Search for neutrinos from TANAMI observed AGN using Fermi lightcurves with ANTARES

Suche nach Neutrinos von TANAMI-AGN unter Verwendung von Fermi-Lichtkurven mit ANTARES

Der Naturwissenschaftlichen Fakultät

der Friedrich-Alexander-Universität Erlangen-Nürnberg

zur

Erlangung des Doktorgrads Dr. rer. nat.

vorgelegt von

Kerstin Fehn

aus Coburg

Als Dissertation genehmigt
von der Naturwissenschaftlichen Fakultät
der Friedrich-Alexander Universität Erlangen-Nürnberg

Tag der mündlichen Prüfung: 24.03.2015

Vorsitzender des Promotionsorgans: Prof. Dr. Jörn Wilms

Gutachter/in:	Prof. Dr. Gisela Anton
	Prof. Dr. Ulrich Katz

ν

Abstract

Active galactic nuclei (AGN) are promising candidates for hadronic acceleration. The combination of radio, gamma ray and neutrino data should give information on their properties, especially concerning the sources of the high-energetic cosmic rays. Assuming a temporal correlation of gamma and neutrino emission in AGN the background of neutrino telescopes can be reduced using gamma ray lightcurves. Thereby the sensitivity for discovering cosmic neutrino sources is enhanced. In the present work a stacked search for a group of AGN with the ANTARES neutrino telescope in the Mediterranean is presented. The selection of AGN is based on the source sample of TANAMI, a multiwavelength observation program (radio to gamma rays) of extragalactic jets southerly of $-30°$ declination. In the analysis lightcurves of the gamma satellite Fermi are used. In an unbinned maximum likelihood approach the test statistic in the background only case and in the signal and background case is determined. For the investigated 10% of data of ANTARES within the measurement time between 01.09.2008 and 30.07.2012 no significant excess is observed. So on the total flux of the AGN of the stacked search an upper limit can be set.

Zusammenfassung

Aktive galaktische Kerne (AGN) sind vielversprechende Kandidaten für hadronische Beschleunigung. Die Kombination von Radio-, Gammastrahlen- und Neutrinodaten soll Aufschluß über ihre Eigenschaften, insbesondere im Hinblick auf die Quellen der hochenergetischen kosmischen Strahlung, geben. Unter der Annahme der zeitlichen Korrelation von Gamma- und Neutrinoemission in AGN kann durch Verwendung von Gamma-Lichtkurven der Untergrund von Neutrinoteleskopen reduziert werden. Dadurch erhöht sich die Sensitivität zur Entdeckung kosmischer Neutrinoquellen. In dieser Arbeit wird eine Stapelsuche nach Neutrinos von einer Gruppe von AGN mit dem ANTARES-Neutrinoteleskop im Mittelmeer vorgestellt. Die Auswahl der AGN beruht dabei auf der Quellengruppe von TANAMI, einem Multiwellenlängen-Beobachtungsprogramm (von Radio- bis Gammastrahlung) von extragalaktischen Jets südlich von $-30°$ Deklination. In der Analyse werden Lichtkurven des Gammastrahlungs-Satelliten Fermi verwendet. Mit einer ungebinnten Maximum-Likelihood-Methode wird die Teststatistik im reinen Untergrundfall und im Signal- und Untergrundfall bestimmt. Für die untersuchten 10% der Daten von ANTARES in der Messzeit zwischen 01.09.2008 und 30.07.2012 ist kein signifikanter Exzess zu beobachten. Damit kann ein oberes Limit für den Gesamtfluss der AGN der Stapelsuche gesetzt werden.

Contents

meinen Eltern

im Andenken an meine Großeltern

Melitta und Wilhelm Früh
und Maria und Johann Fehn

Chapter 1

Introduction

We all want to learn more about our universe. Discovering great secrets with tiny particles is the fascinating idea of neutrino astronomy.
Neutrino astronomy deals with questions reaching from the origin of the universe to its components from dark matter to special objects like supernova SN 1987 detected 23.02.1987. It combines astronomy with particle physics using a great variety of fundamental physical principles from general relativity to magnetohydrodynamics and detector physics. So neutrino astronomy approaches fundamental questions unifying a variety of methods.
From their invention by Pauli, who did not want to give up the principle of energy conservation when he was trying to explain the energy distribution at the beta decay and bravely postulated a new particle, neutrinos have always been bewitching. It was neutrino astronomy that proved via flavour conversion of solar neutrinos that neutrinos have got masses. The virtue that makes them so difficult to detect makes neutrinos unique messengers through space and time: Neutrinos are only liable to the weak interaction and can escape dust, where no photons can and fly straightforward through the universe, where charged particles are deviated.
The detection of protons and ions of energies up to 10^{20} eV leads to the conclusion that there must be an accelerator for hadrons hundred million times stronger than the large hadron collider at CERN somewhere in the universe. To find that collider has been a goal of astroparticle physics for a century. Among other astronomical objects like supernovae remnants and gamma ray bursts, active galactic nuclei are very promising candidates. Diffuse flux analyses as well as point source analyses were performed with the neutrino telescopes. These analyses have to cope, however, with the background over the whole time range that is considered. The

smaller the time bin for an expected signal is, the more the background can be reduced. The present analysis exploits that fact searching for neutrinos from active galactic nuclei from TANAMI sources using Fermi lightcurves with ANTARES.

Chapter 2

Neutrinos from active galactic nuclei

2.1 Black holes in active galactic nuclei

Active galactic nuclei (AGN) are good candidates for the production of neutrinos of high energies. Being a center of a very bright galaxy, an AGN consists according

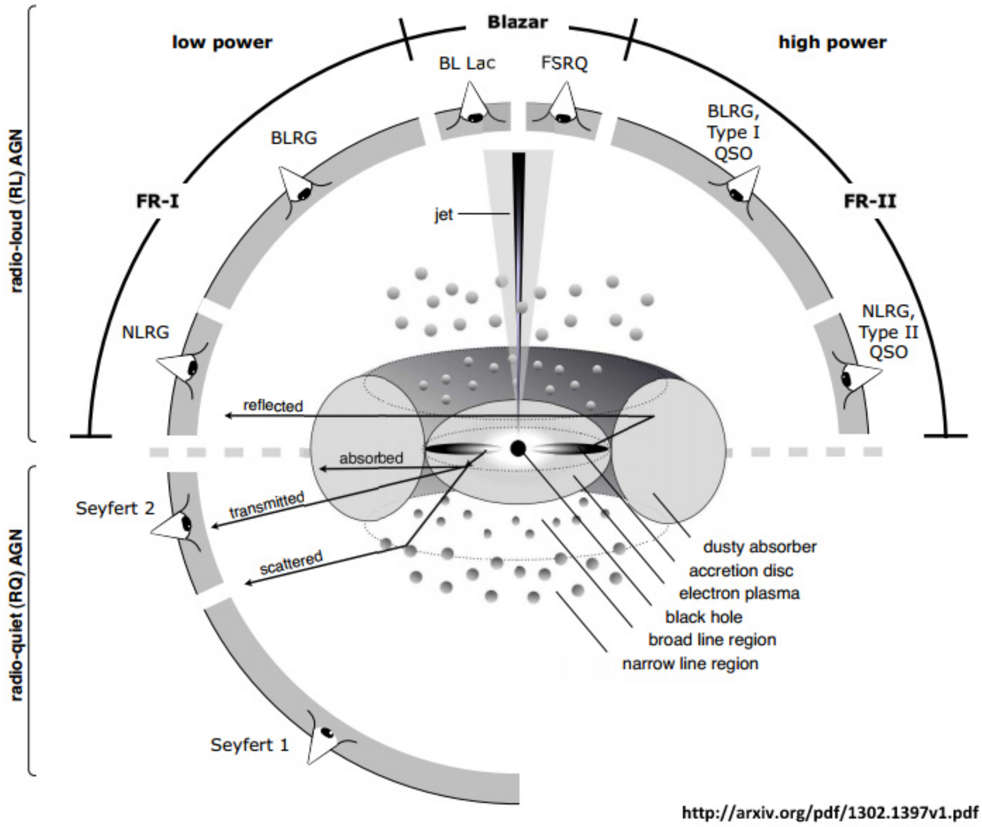

FIGURE 2.1: Overview of types and components of active galactic nuclei [BS12]

to Figure 2.1 of the following components [WM14]:

1. a supermassive ($10^6 - 3 \cdot 10^9$ solar masses) black hole
2. a rotating accretion disk
3. a torus of dust
4. jets

A black hole is formed when the size of a gravitating object of mass M becomes smaller than its gravitational radius $r = \frac{2 \cdot G \cdot M}{c^2}$. In general relativity, a black hole is self-supported empty curved spacetime. While the Schwarzschild solution of the nonlinear field equations only describes static black holes, Kerr [Ke08] found a solution for rotating black holes. Symmetry in time guarantees the conservation of energy, symmetry to the rotation axis of the black hole guarantees the conservation of momentum. The frame dagging effect implies that everything rotates with the same frequency together with the black hole. So does the torus of dust consisting of cold molecules of $10^4 - 10^8$ star masses, which orbits the black hole at a distance of 1 pc. Non axial disturbances can cause matter flow to the black hole. Within the torus a cold Shakura-Sunyaev-disk (SSD) is formed due to the rotation and efficient radiative cooling. A charged particle that is accelerated under the action of electromagnetic radiation becomes a source of dipole electromagnetic radiation itself. Thus the initial electromagnetic radiation is scattered by the charged particle. The spherical accretion of the matter on a massive radiating body has got autoregulation. The Eddington luminosity L_{Edd} is reached, when the outward force of radiation F_{rad} on the matter is equal to the gravitational attraction F_{grav}. The outward force of radiation on the matter at the sphere of radius r is [FZ11]

$$F_{\mathrm{rad}} = \frac{\sigma_{\mathrm{T}} \cdot \rho}{\mu \cdot m_p \cdot c} \cdot \frac{L}{4\pi r^2} \ . \tag{2.1}$$

σ_{T} Thomson scattering cross-section
L total luminosity
ρ density
μ molecular weight per electron
M mass of the black hole
It is equal to the gravitational attraction when the luminosity is

$$L_{\mathrm{Edd}} = \frac{4\pi \cdot G \cdot M \cdot \mu \cdot m_p \cdot c}{\sigma_{\mathrm{T}}} = 1.3 \cdot 10^{38} \frac{\mathrm{erg}}{\mathrm{s}} \cdot \mu \cdot \frac{M}{M_{\odot}} \ . \tag{2.2}$$

[FZ11] The flow of matter in the SSD leads to turbulences, which lead to a redistribution of angular momentum outwardly. This transport of angular momentum causes hydrodynamic and magnetic interactions of the particles. The inner part of the SSD gets hotter, particles are ionized and generate magnetic fields themselves. The charged magnetized fluid moves in curved geodesic lines and can be described by relativistic magnetohydrodynamics. When the magnetic fields get near the event horizon to the ergosphere of the black hole, the Penrose process [Pe69] takes place and the above mentioned frame dagging effect twists the magnetic field lines (see Figure 2.2). When magnetic field lines of different polarity clash, due to reconnection magnetic fields collapse locally and thus transfer energy to the surrounding plasma. So the magnetic energy is transformed into kinetic energy that allows the plasma to escape the black hole and urges poynting fluxes in the Blandford and Znajek process [BZ77]. The dominant toroidal magnetic fields form the so called gravitomagnetic dynamo. When the magnetic field strength is large enough, a leptonic pair plasma of electrons and positrons is generated. The particles can escape from the ergosphere. In this electromagnetic way, rotational energy is extracted from the black hole, but accretion adds angular momentum via infalling matter ([WM14]). The efficiency of the accretion process in the AGN

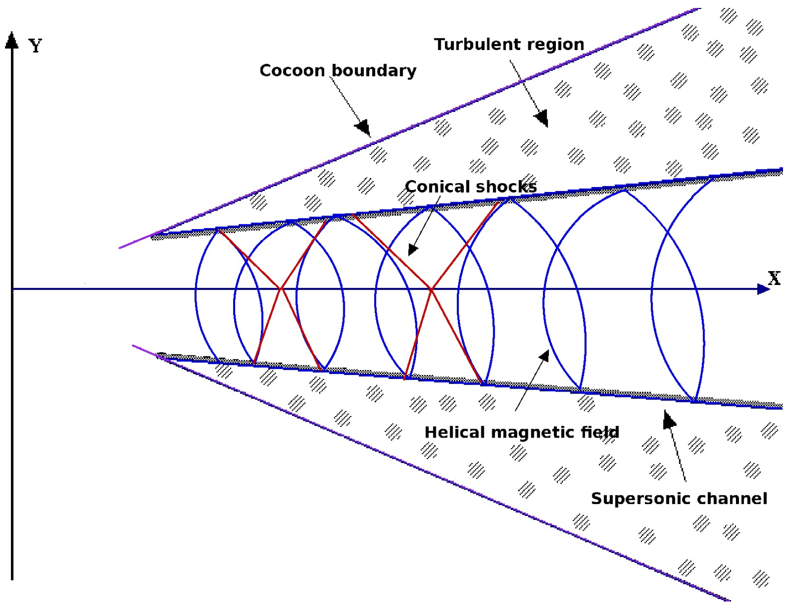

FIGURE 2.2: Helical magnetic field lines [Me12]

can be estimated as follows: When dust of the mass m falls to the black hole of mass M, the infalling matter looses potential energy

$$\Delta E = \int_{R_0}^{\infty} \frac{G \cdot M \cdot m}{r^2} dr = \frac{G \cdot M \cdot m}{R_0} . \tag{2.3}$$

$$\Rightarrow \eta = \frac{\Delta E}{m \cdot c^2} = \frac{G \cdot M}{c^2 \cdot R_0^2} \tag{2.4}$$

The efficiency η is much higher than the efficiency in nuclear fusion for example, it reaches from 10% even to values larger than 100% (see [Tc11]), when energy is extracted from the spin of the black hole.

2.2 Neutrino and photon production

Radiative processes

Important processes concerning particles in an AGN are:

- Synchrotron radiation
- Inverse Compton interaction

Linearly polarized synchrotron radiation reveals that electrically charged particles are accelerated in a magnetic field. While the synchrotron photons of particles at small velocities show a Larmour distribution, the radiation cone of relativistic particles is highly collimated (beaming) with the opening angle of the cone from the synchrotron emission of a single electron being proportional to the inverse Lorentz factor. The synchrotron luminosity for a particle with charge Ze and mass m at a magnetic flux density B and an electric field strength E is

$$L = \frac{4Z^4 e^4 B^2 E^2}{9m^4 c^7} . \tag{2.5}$$

The equation also holds for protons, so a pure proton jet would have to be significantly faster or more massive than an electron or positron jet to reach the same luminosity.

For a relativistic electron or positron, the luminosity is

$$L_{e,\text{rel}} = \frac{4}{3} \sigma_{\text{T}} c \gamma^2 \frac{B^2}{8\pi} \approx 2.7 \cdot 10^{-14} \frac{\text{cm}^3}{\text{s}} \cdot \gamma^2 \cdot \frac{B^2}{8\pi} . \tag{2.6}$$

The spectrum of a single electron emitting synchrotron radiation is sharply peaked, its frequency is

$$f \approx \left(\frac{E}{mc^2}\right) \cdot f_{\text{Larmour}} \,. \tag{2.7}$$

Thus, the energy distribution of the synchrotron emission will depend directly on the energy distribution of the electrons. In case of flat spectrum radio quasars (FSRQ), the electron energy distribution is proportional to E^{-2} [BS12]. At AGN synchrotron radiation has got radio frequencies. The gas of electrons absorbs photons of the self generated synchrotron radiations. This **synchrotron self absorption** increases dramatically at the turnover frequency, which leads to a drop in the spectral energy distribution (SED). At larger frequencies the gas is optically thin. A highly relevant effect in this context is the **synchrotron self Compton** effect. Here low energetic, soft synchrotron radiation is converted into higher energetic, hard radiation through inverse Compton interaction. Soft photons are scattered at the hot plasma and gain energy; this cools the plasma, because internal energy of the plasma, i.e. kinetic energy of the particles in the plasma, is converted into radiation energy. The hot reservoir is the gas of electrons itself. The synchrotron self Compton effect can cause the hump at higher frequencies in the SED. As explained further below in this section, the high frequency hump in the SED can also hark back to pion photoproduction and subsequent cascading.

Acceleration

There are different approaches to describe particle acceleration in jets. An approach being discussed recently is the expansion of an over-pressured, supersonic jet. The classical and most frequently used approach is the Fermi acceleration in shock waves as depicted in Figure 2.3. A basic idea in Fermi's concept (see Figure 2.4) is that a particle can gain energy when it hits a magnetic field that is moving in the opposed direction. Second order Fermi acceleration is not crucial, as in first order Fermi acceleration the statistical gain of energy of a particle at a collision with a magnetic field moving with velocity βc is larger.

$$\left\langle \frac{\Delta E}{E} \right\rangle \approx \frac{4}{3}\beta^i \tag{2.8}$$

$i = 1$ for first order Fermi acceleration

$i = 2$ for second order Fermi acceleration

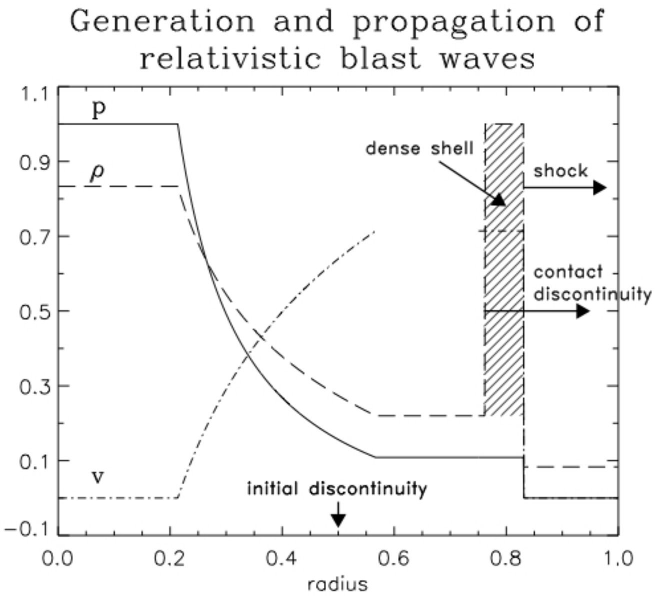

FIGURE 2.3: Relativistic wave [MM03]

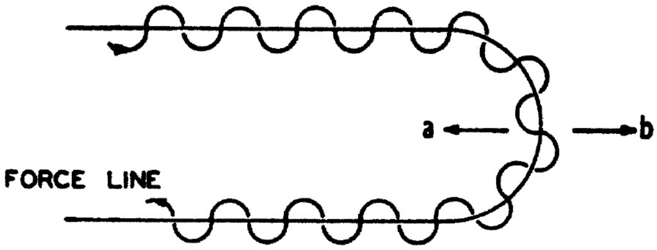

FIGURE 2.4: When the line of force at the bottom of the curve moves in the direction indicated by the arrow a, the particle gains energy (head-on collision). [Fe49]

First order Fermi acceleration describes the acceleration of charged particles at ex-

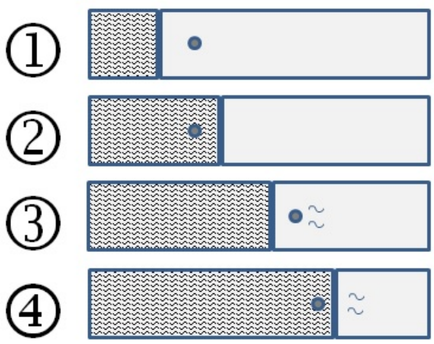

FIGURE 2.5: Scheme of first order Fermi acceleration

tensive shock fronts that move with the velocity v. The interstellar medium (ISM) approximated as ideal, monatomic gas is accelerated to $\frac{3}{4}v$ behind the shock front. Thereby turbulences arise, which generate comoving magnetic fields pictured in

Figure 2.5 ①. A charged particle is reflected by the moving magnetic field and gains energy ②. So the particle comes upon the ISM before the shock front with velocity $\frac{3}{4}v$, it sees the ISM approaching with that velocity. Meanwhile other charged particles crossing the shock front have generated a magnetic field there, too ③. This magnetic fields reflects the particle again. Thus the particle has gained energy a second time and has moved behind the shock front ④ (cf. Figure 2.6).

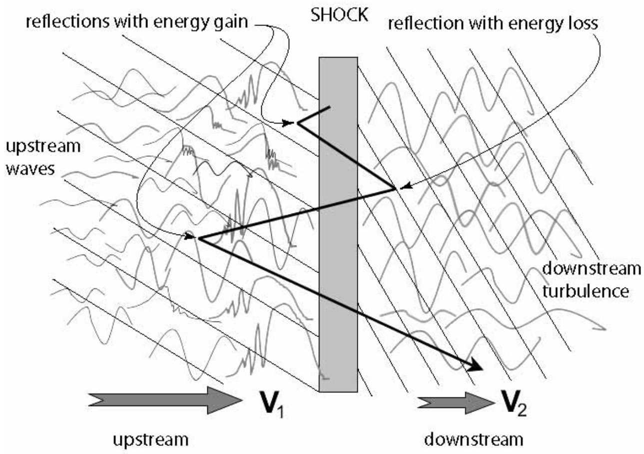

FIGURE 2.6: Shock in Fermi acceleration [Tr08]

Generation of neutrinos

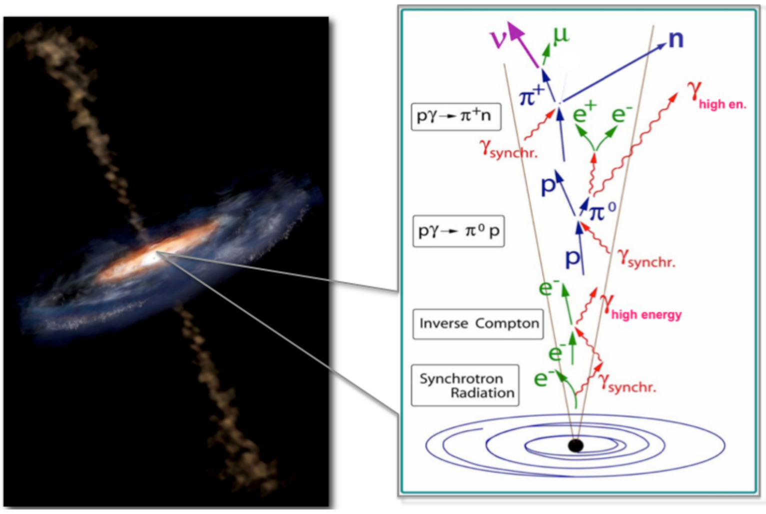

FIGURE 2.7: Artists impression of an AGN (credit Simonnet, A., Sonoma State University) and processes in the jet [KS12]

Neutrinos are generated in hadronic cascades. Their origin in most cases is an interaction of a photon with a proton. This leads to the following processes:

$$
\begin{array}{lll}
 & & \pi^0 \qquad\qquad\qquad +\mathrm{p} \\
 & \nearrow & \hookrightarrow \gamma + \gamma \\
\gamma + p \rightarrow \Delta^+ & & \\
 & \searrow & \pi^{\overset{+}{(-)}} \qquad\qquad\quad +n \\
 & & \hookrightarrow \mu^+ + \nu_\mu \\
 & & \quad \hookrightarrow e^+ + \nu_e + \overline{\nu}_\mu
\end{array}
$$

The ratio of the cross sections $\sigma_{\pi^0 p}$ and $\sigma_{\pi^+ n}$ can be calculated as follows. The Δ^+ baryon consists of two up quarks and one down quark. So while the isospin I of Δ^+ is $\frac{3}{2}$, for the z-component of the isospin of Δ^+ the formula applies: $I_z = \frac{1}{2} + \frac{1}{2} - \frac{1}{2} = \frac{1}{2}$.
For a system $|JM\rangle$ of coupled isospins j_1 and j_2, the square of the Clebsch Gordan coefficents gives the probability for the states $|j_1 m_1\rangle$ and $|j_2 m_2\rangle$.
So the ratio of the branch is [PR99]

$$\frac{B(\Delta^+ \rightarrow p + \pi^0)}{B(\Delta^+ \rightarrow n + \pi^+)} = 2\ . \tag{2.9}$$

There are also higher resonances contributing in the decay chain.

$$\gamma + p \xrightarrow{\Delta,N} \Delta' + \pi, \quad \Delta' \quad \rightarrow p' + \pi' \tag{2.10}$$
$$\gamma + p \xrightarrow{\Delta,N} \rho + p', \quad \rho \quad \rightarrow \pi + \pi' \tag{2.11}$$

Other channels for the neutrino production are the following with the photoproduction to pp interaction cross-section being 0.01.

$$pp \rightarrow \begin{cases} pp\pi^0 & \text{fraction } \frac{2}{3} \\ pn\pi^+ & \text{fraction } \frac{1}{3} \end{cases} \tag{2.12}$$

The interactions 2.9 and 2.10 also take place as direct production in the $t-$channel. Similar processes occur for incident neutrons instead of protons, leading to the production of π^- particles. At higher energies, kaons can also contribute to the spectrum. Positively charged kaons decay with about 64% probability into muons and direct high-energy muon neutrinos. Higher order processes are usually referred to as multipion production processes. The production of two or more pions at high energies can be described by the QCD-fragmentation of color strings.

Lepto-hadronic models

Corresponding to the assumed position of neutrino generation, there are two types of models.[St10]

- Neutrino production close to the black hole
  In these models neutrinos are generated where the infalling matter meets the radiation pressure in a shock $x = 10 - 100$ Schwarzschildradii away from the black hole. From the source luminosity and the mass of the black hole, assuming Eddington luminosity, the radiation energy density at the shock can be derived. The magnetic field at the shock is assumed to be in equipartition with the photon field. From the accretion rate needed to support the source luminosity the proton density can be estimated. The photon density can be derived from the emission spectrum. All photon energy is thermalized.

$$U_{\text{rad}} \approx 10^{-39} \left(\frac{30}{x}\right)^2 \frac{\text{erg}}{\text{s}} \tag{2.13}$$

$$B \approx 2 \cdot 10^{-19} \cdot \frac{30}{x}\ \text{G} \tag{2.14}$$

$$\rho_p \approx 10^8 \cdot \sqrt{x}\ \frac{1}{\text{cm}^3} \tag{2.15}$$

$$\frac{n_p}{n_\gamma} \approx 10^{-13} \cdot x^{1.5} \tag{2.16}$$

  The maximum proton energy at acceleration at the shock is determined by the energy loss on photo production. The further away the shock is from the black hole, the smaller the photon density is and the higher the maximum acceleration can be. For the chosen range of x the acceleration proceeds to sufficiently high energy to generate neutrinos of energy exceeding 10^9 GeV.

- Neutrino production in the AGN jet
  In these models the photoproduction is on internal synchrotron photons or on the thermal UV photon background of the accretion disk. The matter density in the jet is very low and the proton energy loss on *pp* interactions and the neutrino production from this process is small. The high energy neutrino spectra will have the shape of those of the accelerated protons, usually assumed with power law index of 2 before interactions. The containement of 10^{20} eV protons in the jet requires magnetic fields of 1 G at distances of 0.1 pc from the central object.

Purely hadronic models fit the SED well, but face some difficulties explaining the very short time variability. So lepto-hadronic models e.g. [MP14] are favored, where it is assumed that electrons and protons are accelerated at the same site in the jet.

A blob, the emission region, is considered to move along the jet axis with relativistic speed. The relativistic electrons radiate synchrotron photons which serve as the target radiation field for proton-photon interaction in the initial phase of jet expansion and for the subsequent pair-synchrotron cascade which develops as a result of photon-photon pair prodution. While in the high frequency BL Lacertae blazars the high frequency hump of the SED is dominated by proton synchrotron radiation, from the low frequency peaked BL Lacertae blazars (LBL) more neutrinos are being expected. LBLs have got high luminosities and dense photon fields. In order to accelerate protons to energies above the photo-pion production threshold, fields of order 10 G are necessary. With increasing magnetic field strength, the importance of synchrotron radiation increases. Because of the dense photon fields in LBLs, the hump in the SED at low energies can originate from secondary electrons from the muon synchrotron cascade, while the hump at high energies can be explained by muon synchrotron radiation and the radiation of the pion cascade. The contribution of muon synchrotron radiation and pion cascades increases with increasing photon energy density because of the growing efficiency of photo-meson production.

Variability could be caused by an increase in the accretion rate causing a shock to propagate along the jet. Preexisting blobs could thereby be reenergized and may undergo an increase in their bulk Lorentz factor. As the shock moves through the highly magnetized plasma, electrons start to increase their synchrotron photon production, possibly due to an increase in the number of relativistic electrons. This leads to a higher intrinsic photon density. Simultaneously, the number of relativistic protons also increases. The appearance of a fresh relativistic shock in an otherwise weakly turbulent plasma implies an increase of the acceleration efficiency. This leads to a correlated shift of synchrotron peak energy and gamma ray peak energy to higher energies.

The neutrino spectrum depends on the ambient proton spectrum and the spectrum and density of target photons. The ratio of injected electrons and protons is 1 for LBLs assuming most relativistic electrons responsible for the low energy hump in the SED are primaries coaccelerated with the protons. So protons are considered

to be injected in the jet following an E^{-2} spectrum. Due to photohadronic interactions with the photons mainly generated by synchrotron radiation, this spectrum changes to a power law of roughly an E^{-1} spectrum. Therefore also the spectrum of the neutrinos is expected to be E^{-1} (see [MP14], [Ma00]).
Sources are transparent to neutrinos, while protons are near-completely confined and gamma rays are reprocessed in synchrotron-pair cascades until emitted in the energy range of 10 MeV − 30 GeV. The propagation of neutrinos in an universe filled with the cosmic microwave background radiation conserves the particle number. For adiabatic losses due to the expansion of the universe, i.e. particle redshift, the trajectories for neutrino energy have got the following evolution [Ma00].

$$E(z) = E_0 \cdot (1 + z) \tag{2.17}$$

In summary, AGN transform gravitational energy into radiation and kinetic energy of the accelerated particles. If protons are accelerated, high-energy neutrinos can be expected.

Chapter 3

Neutrino telescope ANTARES

3.1 Interactions before detection

As leptonic fermions, neutrinos interact only weakly. So they traverse the universe and the earth. Near the detector, ideally one of the reactions of Figure 3.1

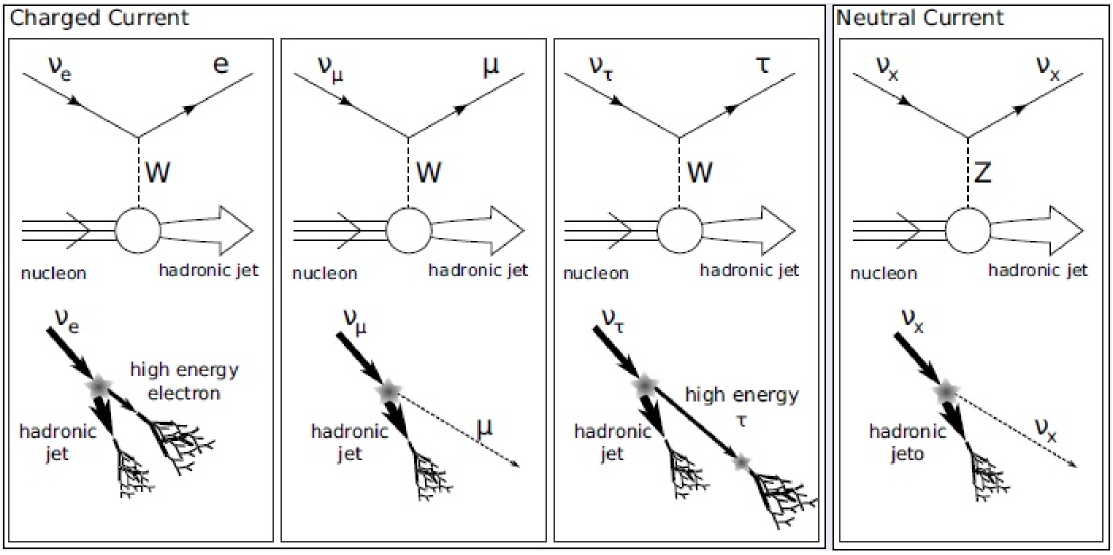

FIGURE 3.1: Interactions [Ti11]

$$\nu_\mu + N \rightarrow \mu^- + X(CC) \tag{3.1}$$

$$\bar{\nu_\mu} + N \rightarrow \mu^+ + X(CC) \tag{3.2}$$

takes place. The neutrino cross section is distributed in Figure 3.2. The leading order double differential cross section of the charged current deep inelastic scattering for an isoscalar nucleus is as follows.

$$\frac{\mathrm{d}^2\sigma}{\mathrm{d}x\mathrm{d}y} = \frac{2G_F^2 ME}{\pi}\left(\frac{M_W^2}{Q^2+M_W^2}\right)^2 [xq(x,Q^2) + (1-y)^2 x\bar{q}(x,Q^2)] \tag{3.3}$$

G_F Fermi coupling constant
M mass of the target nucleon
M_W mass of the W boson
E energy of the incident neutrino
E_μ energy of the outgoing muon
$y = \frac{E-E_\mu}{E}$ inelasticity
Q^2 invariant square of the momentum transferred between neutrino and muon
$x = \frac{Q^2}{2M(E-E_\mu)}$ scaling variable
$q = \frac{1}{2}(d_p + u_p + 2s_p + 2b_p)$ distribution function (i_p density of i quark in proton)
$\bar{q} = \frac{1}{2}(\bar{d}_p + \bar{u}_p + 2c_p)$

The direction of the charged muon deviates maximally by 1.5° from the path of

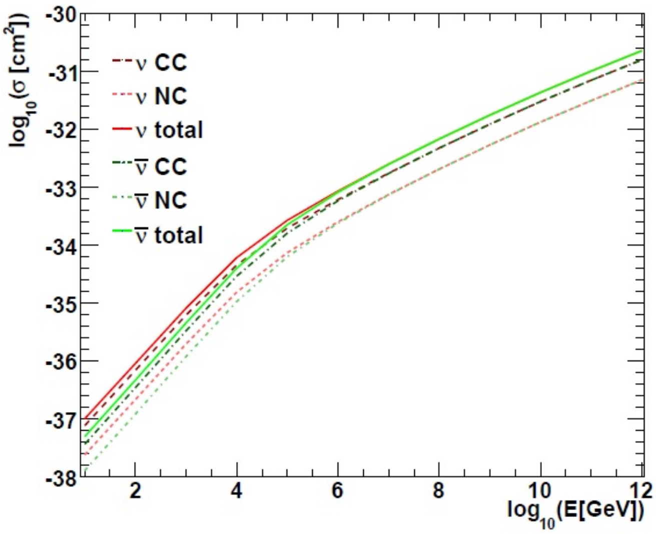

FIGURE 3.2: Neutrino cross section [Scu11]

the neutrino.

$$\vartheta_{\nu\mu} \approx \frac{0.6°}{\sqrt{E_\nu[\mathrm{TeV}]}} \tag{3.4}$$

Before arriving at the detector, the muon is scattered by a small angle by water or rocks. Both deviations are depicted in Figure 3.3. The charged muon moves faster than light in water and therefore emits Cherenkov radiation. The water becomes electrically polarized by the electrical field of the muon. If the muon does not travel slowly, the disturbance cannot relax elastically back to mechanical equilibrium as

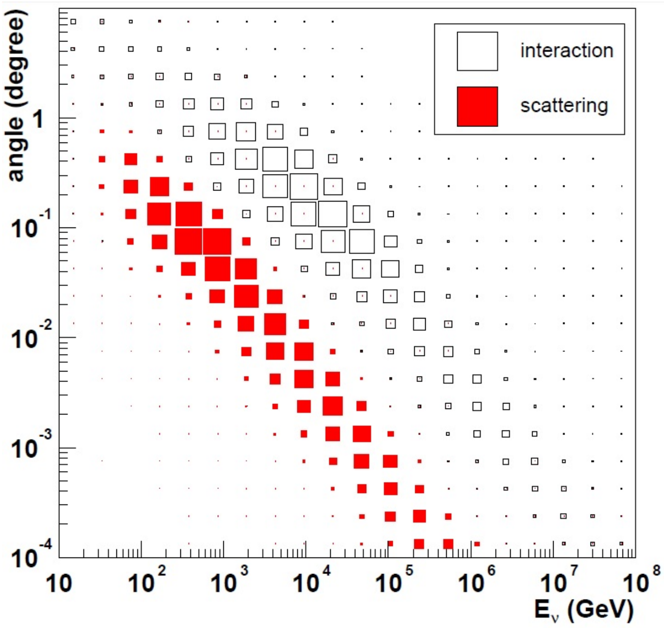

FIGURE 3.3: Deviations [He04]

the particle passes. Instead the limited response speed of the medium means that a disturbance is left in the wake of the muon and the energy contained in this disturbance radiates as coherent shock wave.

$$v_\mu = \beta \cdot c \quad > \quad v_\gamma = \frac{c}{n} \tag{3.5}$$

$$\cos\vartheta \quad = \quad \frac{1}{\beta \cdot n}, \; n \approx 1.35 \tag{3.6}$$

$$\Rightarrow \vartheta \quad \approx \quad 42^\circ \tag{3.7}$$

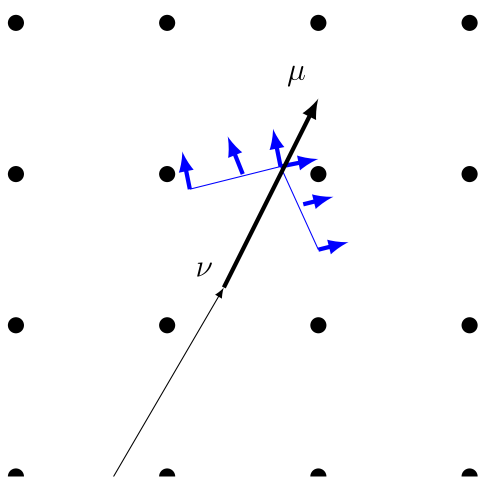

FIGURE 3.4: Cherenkov radiation

Number and energy of the emitted Cherenkov photons depend on the speed of the muon according to the Frank-Tamm formula.

$$\frac{\mathrm{d}^2 N}{\mathrm{d}x\mathrm{d}\lambda} = 2\pi \cdot \alpha \cdot \frac{1}{\lambda^2} \cdot \left(1 - \frac{1}{\beta^2 \cdot n^2}\right) \tag{3.8}$$

λ wavelength of the photon
α fine structure constant
Around the visible spectrum the relative intensity per unit frequency is approximately proportional to the frequency. Within 1 cm flight path of the muon 100 photons are emitted at wavelengths of $400 - 500$ nm.
With the relevant kinetic energies of the muons reaching from about 100 GeV to 10^7 GeV the speeds of the muons vary according to the following relation

$$v = \sqrt{1 - \frac{m_0^2 c^4}{(m_0 c^2 + E_{\mathrm{kin}})^2}} \cdot c \tag{3.9}$$

from $6 \cdot 10^{-5}\%$ smaller than c to $6 \cdot 10^{-15}\%$ smaller than c.
A small proportion of photons is absorbed ($\lambda_{\mathrm{abs}} = 60$ m at $\lambda = 473$ nm), another proportion is scattered ($\lambda_{\mathrm{\ s}} = 260$ m at $\lambda = 473$ nm), the number of photons is the following.

$$N(r) = N_{1\ \mathrm{m}} \cdot \frac{1}{r} \cdot e^{\frac{-r}{\lambda_{\mathrm{abs}}}} \tag{3.10}$$

$r = \frac{k}{\sin\vartheta}$	length of the photon path
$\lambda_{\mathrm{abs}} \sim \frac{1}{\alpha_{abs}} \approx 38$ m	effective absorptionlength
$N_{1\ \mathrm{m}} \approx 100$	number of photons 1 m away from the muontrack

The arrival time at an optical module (OM) depicted as black dot in Figure 3.4 is composed of the driving time of the muon until the Cherenkov photon is emitted and the driving time of the photon.

$$t = t_\mu + t_\gamma = [t_0 + \frac{1}{c}(l - \frac{k}{\tan\vartheta})] + [\frac{1}{v_g}(\frac{k}{\sin\vartheta})] \tag{3.11}$$

k shortest distance from the muon track to the OM
l distance on the muon track from the current location to the point with the shortest distance to the OM
c approximation of the speed of the muon
v_g group velocity of light in water (value taken at 460 nm)
The length of the photon path $\frac{k}{\sin\vartheta}$ has to be shorter than the absorption length in water.

The angle of incidence of the photon on the OM is given by

$$\cos(\alpha_i) = \vec{p_\gamma} \circ \vec{w} = [\overrightarrow{XO} - \vec{p_\mu}(l - \frac{k}{\sin\vartheta})] \circ \vec{w} \tag{3.12}$$

$\vec{p_\gamma}$ unit vector of the momentum of the photon
$\vec{p_\mu}$ unit vector of the momentum of the muon
$\vec{w}$ unit vector of the pointing direction of the OM
$\overrightarrow{XO}$ vector from the location of the muon to the location of the OM

At wavelengths of $400 - 500$ nm the efficiency of the photomultipliers as well as the transparency of the water are maximal.

3.2 ANTARES detector

The Cherenkov photons emitted by the muon reach the detector. The ANTARES

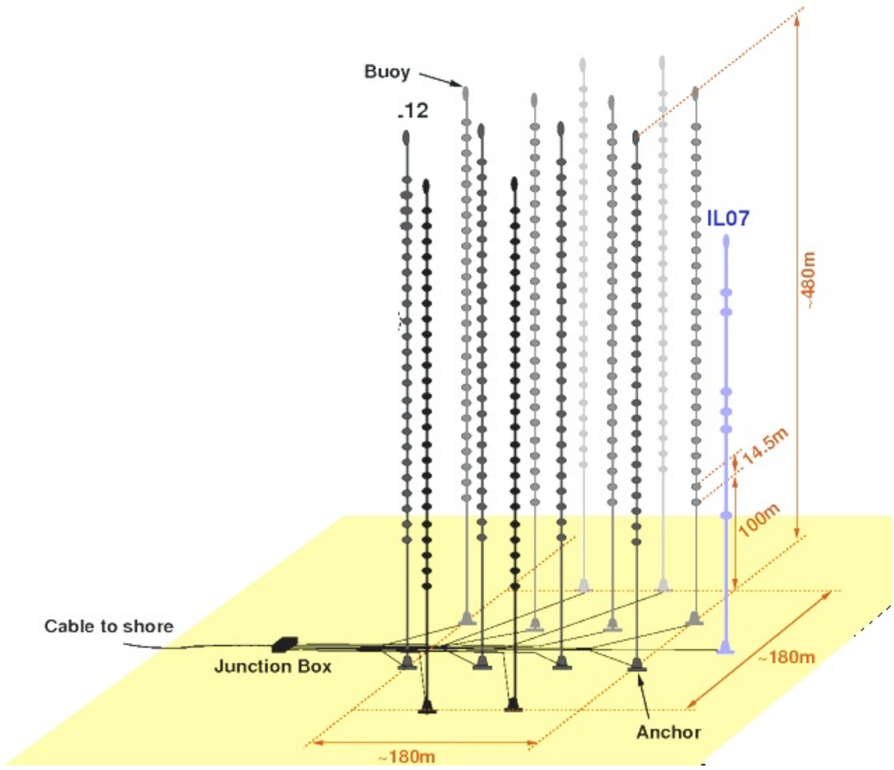

FIGURE 3.5: Neutrino telescope ANTARES [Ag11]

detector is located at a depth of 2475 m in the Mediterranean Sea at 42°47.935′ N, 6°09.942′ E, 42 km from Toulon in the south of France. It consists of a array of 885 optical sensors arranged on 12 vertical lines with 25 detection storeys on each line located $100 - 450$ m above the sea bed (see Figure 3.5). The spacing between storeys is 14.5m while the lines are spaced by $60 - 70$m, so the detection volume is about 0.03 km^3. In May 2008 the full detector with 12 lines was completed. The main detection elements are photomultipliertubes (PMTs) hosted in the above mentioned OMs shown in Figure 3.6. Each OM consists of a pressure resistant

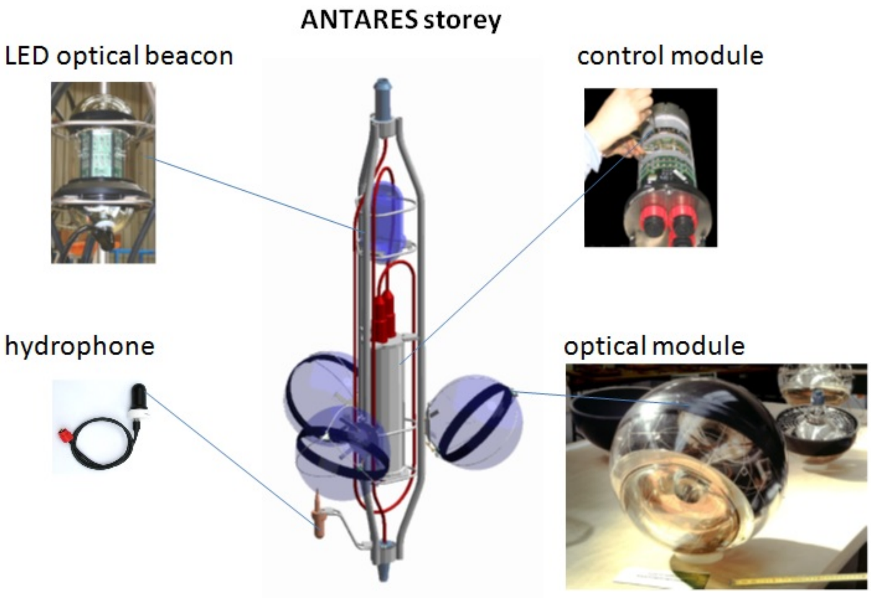

FIGURE 3.6: Basic detector element (photographies (c) CEA/DSM/DAPNIA)

blackened glass sphere with diameter 43 cm, which hosts beside the PMT within optical gel the electonics that provide the high voltage. When optimally oriented, the projected area of the photocathode is 440 cm^2, which corresponds roughly to the diameter of 10". The PMT has got nominal amplification $5 \cdot 10^7$ at a high voltage of 1760 V. When a photon detaches an electron from the photocathode, the electron is accelerated in 14 stages, which leads to a torrent of electrons that is evaluated as electronic signal.

The signals from the PMTs get time stamps by the local electronics. This is done by a system of a 20 MHz master clock onshore, whose signal is distributed via optical fibers to clocks at the local control modules on the lines. The different paths have got different lengths, so the clocks must be synchronized. In order to measure this optical path length, a calibration signal can be sent to a local control module, which returns the signal. Thus the offsets are determined. This measurement does not take into account the transit time of the PMT, which depends on the high voltage put on the PMT. The transit time can be measured by flashing a LED located inside the optical module, which illuminates the back of the photocathode. For the **time calibration** of the whole system, two more devices are deployed. Four floors per line are equipped with an optical beacon, which can emit a set of pulsed LED flashes, which illuminate a number of OMs on adjacent lines. Besides, there is a powerful pulsed laser located at the bottom, which can illuminate a large part of the detector. The **assignment of a time** to a hit is as follows: Using the rising and falling flank of the clock pulse, a time stamp of 25 ns is generated. Within each time stamp, a time to voltage converter (TVC) measures the arrival time of the amplified signal at a precision of 0.2 ns with the overall time resolution of the arrival time dominated by the PMT transit time spread of 3 ns. The two TVCs of each OM work in flip-fop mode with one active at any time while the other is being reset. The calibration of the TVCs is done creating hits at random times, integrating the voltage and comparing with the linear fit. So the digitized hit times consist of the following two components.

- Number of the timestamp, i.e. value of the 20 MHz clock
- TVC value

The **amplitude of the signal**, normalized to be equivalent to the number of electrons emitted from the photocathode and therefore expressed in units of photoelectrons (pe) is determined by an amplitude to voltge converter (AVC). When a certain threshold, 0.3 pe by default, is reached, integration of the signal starts for one timestamp of 25 ns. After recording a hit, it takes 13 ns to switch to the other AVC, which then is available to record the next hit. The dead time of each AVC is 250 ns, in which it is reset. In a special calibration run, in which the high voltage of the PMT is switched off, the permanently present signal from purely electronic noise is measured.

Since the optical modules are mounted on flexible strings, their **positions** and orientations are influenced by currents in the sea water and must therefore be monitored. The orientation of each OM is measured by a compass and a tilt-meter. In addition, one in five floors is equipped with a hydrophone as shown in Figure 3.6. The hydrophone records acoustic signals from transmitters located at the bottom of the line. Via the propagation times of these acoustic signals, the position of the hydrophones is determined.

The data are collected in so called runs.

3.3 Triggers

On shore, a computer farm runs a set of trigger algorithms to identify events containing Cherenkov light from high-energy muons within the data stream, which otherwise consists mostly of signals from radioactive decay and bioluminescence. Hits with an amplitude larger than a certain value (usually 3 pe) and coincident hits, that are measured on different OMs of the same storey within a tunable time window (20 ns by default) are tagged as $L1$ hits. Within the $L1$ hits the triggers are looking for causally connected hits.

- $3N$ trigger
  $L1$ hits that fulfill the follwing condition are chosen.
  $|\Delta t| < \frac{|\Delta x|}{c_\gamma}$ where $|\Delta t/x|$ are absolute temporal/ spatial distances between two hits
  Only if the hits are consistent with a muon fom a certain direction, the cluster that is derived in this way, is kept.

- $2T3$ trigger
  It searches for $L1$ hits in adjacent or next-to-adjacent storeys within a time window of 100 ns or 200 ns respectively.
  Two of these so called $T3$ clusters within a time interval of 2.2 μs are needed to accept the data as physics event.

- GC trigger
  The Galactic center trigger requires one $L1$ hit and four raw hits with an amplitude greater than 0.3 pe in the direction of the galactic center.

- $K40$ trigger
  This trigger is used for in situ calibration. It requires two raw hits with an amplitude grater than 0.3 pe on two OMs of the same storey within a time window of 50 ns.

3.4 Background

The effect the $K40$ trigger is named after is the β decay of radioactive **Kalium** in water.

$$^{40}_{19}K \rightarrow^{40}_{20} Ca + e^- + \bar{\nu}_e \quad (89\%) \tag{3.13}$$

$$^{40}_{19}K + e^- \rightarrow^{40}_{18} Ar + \nu_e \quad (11\%) \tag{3.14}$$

$$^{40}_{19}K \rightarrow^{40}_{18} Ar + e^+ + \nu_e \quad (0.001\%) \tag{3.15}$$

So the main contribution to uncorrelated background from $^{40}_{19}K$ is reaction 3.13. The emitted electron moves faster than light in water and thus emits Cherenkov radiation. This causes a certain rate of coincident hits on adjacent PMTs, which is so well understood that it is even used to check the time calibration as well as to monitor the efficiency of PMTs. Another source of unavoidable background radiation is **bioluminescence**. Bacteria are a steady baseline source of light with rates of about 30 kHz. Macro-organisms cause short flashes up to the order of MHz. In the mediteranean sea there are organisms and megaplankton in the size range of $0.2 - 2000$ mm. Pyrosoma and bacteria glow in movement. Bioluminescence undergoes seasonal fluctuations and is high in spring. There is also a relatively strong correlation to the sea current. These observations could indicate that the bacteria tend to glow more when in movement or that the current transports nourishment, which leads to a breeding of the bacteria. Data quality parameters (see 8) have been introduced to take the varying conditions regarding bioluminescence into account.

With respect to the aim of ANTARES to detect cosmic neutrinos also other particles are background, especially atmospheric muons and neutrinos. The earth shields from atmospheric muons from below, so called upgoing muons. The orientation of the OMs prevents from observing atmospheric muons from the sky. These so called **downgoing muons**, however, cause Cherenkov light in water, too, which might be misreconstructed as upgoing track. Unlike truely upgoing atmospheric muons, **upgoing atmospheric neutrinos** can cross the earth. They can only be distinguished from cosmic neutrinos via the energy.

3.5 Track reconstruction

After recording the hits, the data have to be analyzed. There are two basic principles of reconstruction, track reconstruction and shower reconstruction. The latter searches for light emitted within an electromagnetic cascade, when an electron suffers bremsstrahlung and produces photons, which produce an electron-positron-pair, which again suffer bremsstrahlung and so on, until the energy of the constituents falls below the critical energy; the remaining energy is dissipated by ionisation and excitation. For electromagnetic showers it can be assumed that all Cherenkov light is emitted isotropically from the shower axis, as the lateral extension of an electromagnetic shower is on the order of 10 cm. While the energy resolution of shower reconstruction is higher, the pointing accuracy is smaller than the pointing accuracy of track reconstruction. Therefore for this point source analysis, a track reconstruction algorithm that follows the principles described in Equation 3.11 was used. The reconstruction strategies are tested in toy samples, where the numbers and directions of inserted signal and background events are known. Aim of the track reconstruction is to avoid reconstructing tracks of downgoing atmospheric muons as upgoing while reconstructing as many signal events as possible. Different track reconstruction algorithms are developed within ANTARES. A strategy that has got a good ratio in this respect especially for highly energetic events is the strategy Aafit developed by Aart Heijboer. Besides the following strategies exist: Bbfit, developed by Jürgen Brunner and Salvatore Galatea, provides fast reconstruction and good performance especially for low energies, OSFfit, developed by Katrin Roensch, uses Bbfit as prefit and works with analytical probability density functions unlike the other algorithms that are based on Monte Carlo productions, Gridfit, developed by Erwin Visser for the low energy range, and Krakefit, developed by Stefanie Wagner for the high energy range, both use Filteringfit, developed by Claudio Kopper. Besides a program that combines Aafit, Bbfit and Gridfit based on random decision forests is being developed by Stefan Geißelsöder. Because of its comparatively high efficiency Aafit (see [He04]) is used for the present work and is described here shortly. It consists of six steps:

1. Pre-selection of hits

   In order to make the algorithm insensitive to the amount of background, a rough selection is performed. Since the hit with the largest amplitude is almost always a signal hit, only hits are selected, which fulfill the following criterion.

$$|\Delta t| \leq \frac{d}{v_g} + 100 \text{ ns} \tag{3.16}$$

Δt time difference between a hit and the hit with the largest amplitude

d distance between the OMs of the two hits

2. Linear prefit

   First, all hits are assumed to be on points that are located along the muon track. The prefit is a linear fit through the positions of the hits with the hit time as independent variable.

3. M-estimator fit

   An M-estimator is an estimator that maximizes a function. Preferable are estimations that are robust against large fluctuations in a small number of data points. Ideally, a reasonable track reconstruction can be obtained without the requirement of choosing the perfect starting point. In the present case, the following function is used.

$$G = \sum_i \kappa \left(-2\sqrt{1 + A_i \frac{R_i^2}{2}} \right) - (1-\kappa) f_{\text{ang}}(\alpha_i) \tag{3.17}$$

   R_i residual

   $\kappa = 0.05$ parameter optimized using Monte Carlo events

   $f_{\text{ang}}(\alpha_i)$ angular response function of the OM

4. Maximum likelihood fit with original probability density function (PDF)

   For each possible set of track parameters, the probability to obtain the observed events is calculated. Then standard numerical tools are used to find the maximum of the likelihood function.

$$P(\text{event}|\text{track}) = \prod_i P(t_i | t_i^{th}, a_i, r_i, A_i) \tag{3.18}$$

   t_i time of the hit

   t time see 3.11

   $a_i = \cos(\alpha_i)$ see 3.12

   r_i length of the photon path see 3.10 A_i amplitude of the hit

5. Repetition of steps 3 and 4 with different starting points

   The efficiency of the algorithm is improved by the repetition of the steps.

The result with the best likelihood per degree of freedom as obtained in step 4 is kept.

6. Maximum likelihood fit with improved PDF
   Finally, the preferred result obtained in step 5 is used as a starting point for the last maximum likelihood fit. This fit also takes hits from background into account.

As mentioned previously, a challenge in finding cosmic neutrinos are misreconstructed muons. Among others, this is taken into account in the quality parameters of the fit.

- lambda parameter

$$\Lambda = \frac{log(L)}{n_{\mathrm{dof}} - 0.1(N_{comp} - 1)} \tag{3.19}$$

  L likelihood from the final fit
  n_{dof} number of degrees of freedom
  N_{comp} number of prefits from the second step with a deviation of less than $1°$ from the best one

- beta parameter
  The beta parameter is also called $\hat{\alpha}_\mu$ and is the error estimate on the direction extracted from the error matrix of the fit.

$$\hat{\alpha}_\mu = \sqrt{\sin^2(\hat{\vartheta})\hat{\sigma}_\varphi^2 + \hat{\sigma}_\vartheta^2} \tag{3.20}$$

  $\hat{\vartheta}$ fitted zenith
  $\hat{\sigma}_\vartheta$ zenith error
  $\hat{\sigma}_\varphi$ azimuth error

3.6 Energy reconstruction

The muon looses energy on its path because of the following effects.

- Photonuclear interaction
  The muon exchanges a virtual photon with a nucleus.

- Ionisation
  The charged muon ionizes atoms in the medium. The energy transfer to the electrons is usually modest, but occasionally so called knock-on electrons obtain a non-negligible fraction of the energy of the muon.

- Pair production
  A e^+ e^- pair is produced.

- Bremsstrahlung
  The muon emits a photon in the nuclear electric field.

The energy loss of the muon due to pair production and bremsstrahlung increases strongly with energy. The amount of light emitted by the electromagnetic cascades resulting from these processes can be used as a measure for the muon energy loss and thus for the muon energy.
Nevertheless, due to the small size of the ANTARES detector compared to the muon track length, which is of the order of kilometers at energies above 1 TeV, the energy deposited within the detection volume by muons of the same energy can vary greatly. Therefore it is reasonable to combine various observables through a likelihood approach in order to increase accuracy. One representation of a likelihood approach ca be achieved using an Artificial Neuronal Network (ANN) for the mapping of the likelihood between the chosen observables and the energy. A simple ANN consists of nodes and connections between the nodes. The output w_j of each node j is calculated as follows.

$$z_j = g\left(\sum_i w_{ij} x_i\right) \tag{3.21}$$

x_i input parameters from node i
w_{ij} connection weight
g activation function describing the reaction of node j
$g(x) = \tanh\left(\frac{\alpha x}{2}\right)$ with $\alpha = 1$ chosen
The ANN must be trained. For this purpose the available data sample is divided into subsets. The information content of the training sets should be disjoint, but each training set should contain the maximum amount of information. In the same way validation sets are created. Every training set has got a corresponding validation set that is associated with it. In the training sets the input values are propagated through the ANN and the output of the ANN is compared with

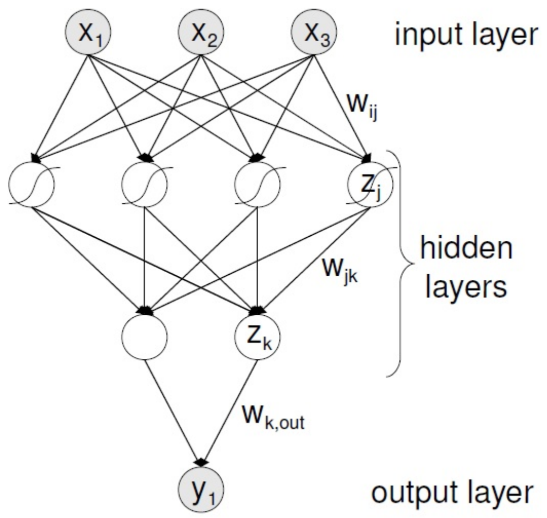

FIGURE 3.7: schematic view of an ANN [Scn10]

the expected output values. While in the beginning the connection weights are chosen randomly, during the training they are adapted recursively, starting from the output layer, with the goal to minimize the mean square error (MSE).

$$MSE = \frac{1}{N_{\text{sample}}} \sum_{k=1}^{N_{\text{sample}}} (y_{\text{out,ANN},k} - y_{\text{out,sample},k})^2 \tag{3.22}$$

The energy estimator ANNergy is created using ANN. In the present work, the ANNergy estimator was applied after the track reconstruction. Therefore also parameters related to the track could be taken into account. Among others, important parameters are the following:

- triggered hits
- working OMs, triggered OMs
- track effective length, track zenith, distance between muon track and the center of gravity of the detector
- mean charge of hits within a time window of $[-20\text{ ns}, +300\text{ ns}]$ around the first and last hit that was found by the trigger algorithm

As ANNergy has got a comparatively good resolution for high energies (cf. [Scn10]), this estimator was adopted. In the following the energies reconstructed with the ANN estimator are called annergies.

In this chapter the collection and the principle of the evaluation of data from the neutrino telescope ANTARES is described, while in the next chapter the simulation is depicted.

Chapter 4

Simulation

4.1 Point source and run by run Monte Carlo

Aim of the simulation is to model all the processes that take place as accurately as possible. A simulation is performed for two reasons. As it is built of physical theories as described in Section 3.1, the comparison of simulated and real data (see Section 4.3) helps understanding physical processes. The major task of the simulation in this work is to provide information that can be used to optimize the search for neutrinos from AGN.

As AGN are so far away (redshifts see Table 6.1), they can be considered as point sources. That is the reason why a point source simulation was implemented. Besides within ANTARES a run by run simulation is available, which was implemented in a second step. The two approaches are discussed at the end of this section.

The simulation described in this chapter comprises the chain parallel to the processes described in Chapter 3. It consists of the four consecutive blocks named after the software packages GENHEN, KM3, Trigger Efficiency and SeaTray that perform the steps from the simulation of neutrinos to the genesis of muons, their interactions, the simulation of Cherenkov light, the response of the detector and the reconstruction of tracks from it.

GENHEN

GENHEN (GENerator of High Energy Neutrinos) is the ANTARES software package to simulate neutrino interactions in the proximity of he detector. It is the first step of the simulation chain for Monte Carlo production of events. GENHEN generates interacting neutrinos inside a generation volume, whose size depends on the energy, the flavor and the interaction type of the neutrino.
The required inputs for the simulation include a detector geometry file. In the present work for the point source Monte Carlo simulation the same geometry file was used as for the latest available run by run simulation v 2.2, the detector geometry file r12_c00_s04.det. It refers to the situation of the detector after the redeployment of lines 6, 9, 12 in 2010 and assumes a sea current of 0 $\frac{\text{cm}}{\text{s}}$. While in previous versions the sea floor was considered to be at a depth of 2475 m, in the present version of the detector geometry the value is 2478 m. The detector geometry file is used to calculate the so called can. The can is the base for the generation

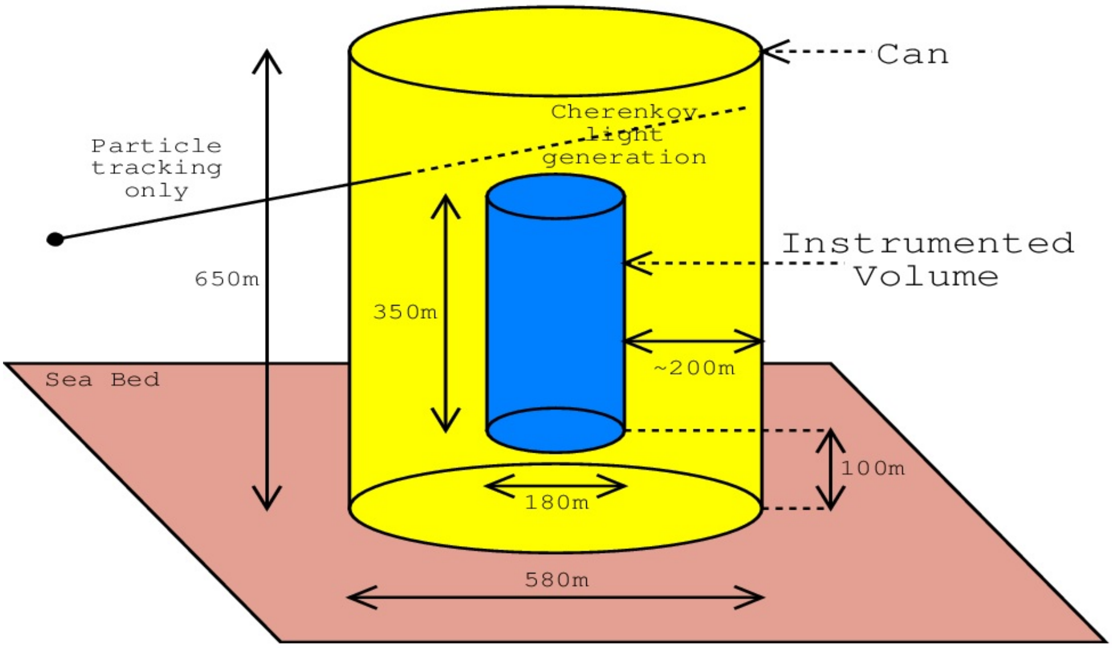

FIGURE 4.1: Detector geometry for the event generation stage of the simulation [Ba02]

volume, which is an energy-dependent extension of the can, within which neutrino interactions are generated. Outside this volume only particle energy losses in propagation are considered. The can size shown in Figure 4.1 exceeds the instrumented volume by about 200 m except from below where it is bounded by the sea bed from within which no Cherenkov light can emerge. Figure 4.2 depicts the scheme of the simulation. In GENHEN, the model LEPTO [In96] is used for the generation of

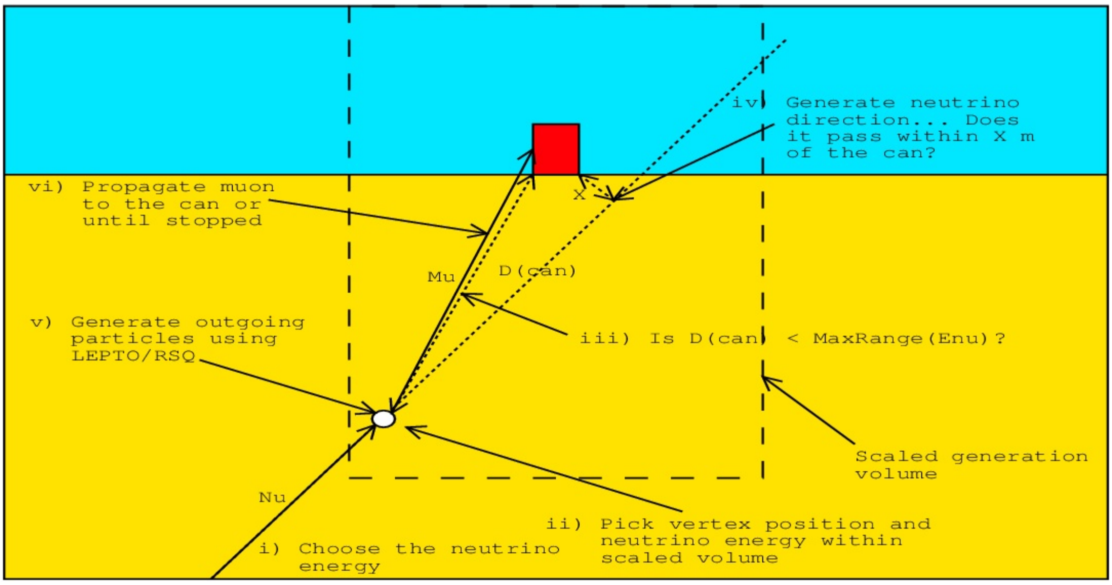

FIGURE 4.2: Scheme of the simulation chain [Ba02]

interaction events and also for the computation of neutrino cross sections at the initialization stage of each energy bin. LEPTO can reproduce the published cross sections and kinematics described in Section 3.1 to better than 5% in the main region of interest [Ba02]. The formula for the deep inelastic cross section presented in Equation 3.3 relates to isoscalar nuclei. Standard rock (A = 22, Z = 11, taken from [Li91]) is an isoscalar nucleus corresponding to the formula above. Water, however, is not, and this has got an effect on the total cross section. Besides the target density of the two media are different ($\rho_{\text{rock}} = 2.65\frac{\text{g}}{\text{cm}^3}$, $\rho_{\text{water}} = 1.04\frac{\text{g}}{\text{cm}^3}$), which is taken care of by the use of water equivalent units, where the density is set to one and all distances rescaled accordingly. The error can be reduced, when water is used for low energies where most vertices are in the can and rock for high energy upgoing events where most events start within the rock [Ba02]. The transmission probability of the earth is also taken into account.

$$P_{\text{trans}} = e^{-N_{\text{A}}\sigma_\nu(E_\nu)\int\rho_\vartheta(l)dl} \tag{4.1}$$

N_{A} Avogadro number

ρ_ϑ earth column depth in the neutrino direction ϑ

σ_ν neutrino CC cross section

The formula 4.1 assumes that a neutrino disappears after a CC interaction, since muons or other secondaries are absorbed through the path to the detector and decay at rest into neutrinos that cannot reach the region close to the detector. For ν_μ effects of NC that produce another neutrino of lower energy than the current one can be neglected, because $\sigma_{NC} \approx 0.4 \cdot \sigma_{CC}$ for ν_μ [AM04]. Dominating is the deep inelastic scattering, but the quasi elastic channel and the resonant channel with Glashow resonance including the W decay channels e, μ, τ, hadrons are also implemented in GENHEN. The hadronization is done with PYTHIA and JETSET [Sj95]. For muon propagation the software package MUSIC [An97] is used. Since the GENHEN release v6r10 applied in the present work, the atmospheric flux is Bartol by default. The flux of neutrinos arriving at the earth that is simulated is the following.

$$\frac{\mathrm{d}\Phi_\nu}{\mathrm{d}E_\nu \mathrm{d}S \mathrm{d}t} = g_1 \cdot g_2 \cdot g_3 \tag{4.2}$$

$$\begin{aligned} g_1 &= \frac{E^{-X}}{I_E} \cdot \frac{N_{\text{total}}}{V_{\text{gen}}} \cdot \frac{1}{t_{\text{gen}}} \text{ distribution of the rate of interacting neutrinos} \\ g_2 &= \frac{1}{\sigma(E_\nu)\rho N_{\text{A}}} \text{ inverse target nucleon density and interaction cross section} \\ g_3 &= \frac{1}{P_{\text{trans}}(E_\nu, \vartheta_\nu)} \text{ inverse transmission probability through the earth} \end{aligned}$$

E_ν neutrino energy [GeV]
S area [m^2]
$-X$ spectral index for the interacting neutrinos
I_E energy phase space factor, integrated generation spectrum from E_{min} to E_{max}
N_{total} number of simulated events
V_{gen} generation volume [m^3] (definitions according to [Bru99])
t_{gen} generation time
For a flux corresponding to a particular model, every event in each interval dE_νdϑ has to be reweighted by the ratio of the two fluxes.

$$w_{\text{event}} = \frac{\mathrm{d}\Phi_\nu^{\text{model}}}{\mathrm{d}E_\nu \mathrm{d}S \mathrm{d}t} : \frac{\mathrm{d}\Phi_\nu}{\mathrm{d}E_\nu \mathrm{d}S \mathrm{d}t} \equiv \Phi(E_\nu, \vartheta_\nu) \cdot w_{\text{generation}} \tag{4.3}$$

So for convenience, the inverse of 4.2 is stored for each event as $w_{\text{generation}} \equiv w_2$ in GENHEN and has to be multiplied by the energy spectrum. GENHEN simulates one ν or $\bar{\nu}$ flavor at a time and one type of interaction (CC or NC) at a time. For the present analysis, neutrino charged current interaction was simulated with the following settings in particular.

- energy range $10^2 - 10^8$ GeV

- number of simulated events 10^{10}
- spectral index -1
- POINTMODE TRUE

When POINTMODE is set to TRUE in GENHEN, which can only be done when generating the Monte Carlo personally, a declination can be chosen. The specified declination is the declination of the emitting point of simulated neutrino events, the hourangle is randomly generated between 0 and 2π, a subroutine included in the SLALIB Positional Astronomy Library [WS14] is used to convert equatorial coordinates into horizon coordinates, given the detector latitude [Bo14].

KM3

The output of GENHEN is processed with KM3 to simulate the production of Cherenkov light and the propagation of photons to the optical modules, where they generate hits. All long-lived particles are tracked through the water in the can volume. The composition and density of the water is adjusted to the values at the experimental site. KM3 performs a high energy muon simulation with light diffusion. As a full simulation where every Cherenkov photon is generated and propagated individually is not possible, KM3 works with photon tables. The photon tables store the distributions of the nmbers and arrival times of PMT hits at different distances, positions and orientations with respect to a given muon track. The KM3 software package consists of three programs (see [NT99]).

- GEN
  GEN generates the photon fields at various radii from a muon track segment.
- HIT
  HIT transforms the photon fields from GEN into hit probability distributions in a photomultiplier tube.
- KM3MC
  KM3MC is a detector simulation program which uses the hit probability distributions generated in HIT along with a geometrical field description of the detector to simulate events in the ANTARES detector.

GEN and HIT are run only once to generate the relevant tables of the hit probabilities in the OMs. KM3MC reads the user inputs from the cards file, the description files and the tables containing the information with the hit distributions for muons and eletrons. The MUSIC [An97] package is then initialized and the event input file with the list of events and the output file with the list of hits are opened. The detector geometry file with the location and orientation of the OM clusters is read in and stored in memory. A muon is processed if its distance of closest approach to the detector is smaller than about 200 m. The muons are propagated through the medium using MUSIC by iterating through track segments (typically 1 m long until the muon is stopped or leaves the detector. For each step, the energy loss by the muon, the start and end positions, the direction and the time of the muon are stored in arrays. If the energy lost by a muon in a segment is well above the average energy loss by ionization, an independent electromagnetic shower is assumed to occur at random location along the length of the segment. This new particle is added to the event particle stack and is treated sparately as an electron. Once the array with the parameters of each segment for muons and electrons is filled, the program computes the direct hists and the scattered hits produced by the muons and electrons. In the present work, the water model of the run by run production v2.2, tab_dic08_extend_reproc, was used.

Trigger Efficiency

The output of KM3 is forwarded to the Trigger Efficiency program [Jo10]. With this program different triggers can be processed simultaneously. It is also possible to specify the settings of the PMT read out system and the photomultiplier characteristics. For the point source Monte Carlo simulation, the raw data of run 58104 were read, as this run has got average conditions. Taken at our shift 16.06.2011, the run has got the typical trigger setting 3N+2T3+K40+TS0 June2011 and calibration label 2011:V3.0. The detector file corresponds to the run with 756 as the mean number of active OMs. The quality basic parameter (see 8) for the run is 4 with the baseline being 88 kHz and the burst fraction being 0.07, the median of the triggered hits is 13.5. Trigger Efficiency changes the data format from .evt to .root, a format that can be read by the SeaTray framework that is described next.

SeaTray

The SeaTray software framework breaks down the software into small functionality units with well-defined interfaces [EK09]. SeaTray is a stream based environment that enables the combination of modules with physical content. Each stream is divided into frames, which correspond to detector status files, to geometry files, to calibration files or to events. Every module reads out frame objects, modifies them and passes them to the next module. The output of the first SeaTray chain used in the present work has got the data format .i3. For the following steps of the point source Monte Carlo production the same script is used as for the run by run Monte Carlo production v2.2.

- Get run information
- Get geometry information
- Get calibration information
- Read root files
- Set missing OM condition to off
- Calibrate hits
- Get run statistics
- Reconstruct tracks (see 3.5) AafitFinalFit reco_v1r0.so latest official version
- Reconstruct energies (see 3.6) ANNergyreco ANN_LatestReco

For the evaluation of directions, i.e. angles to the source (see Section 5.1), a module called MCplots is written for this analysis. In its original version it calculates the angle between the reconstructed muon and the position of the source in declination and right ascension, but as Trigger Efficiency does not process the hourangle, the program is rewritten and now compares the direction of the reconstructed muon to the direction of the most energetic original particle. Before, this direction has been proved to agree with the direction to the source.

Comparison of point source Monte Carlo simulation and run by run Monte Carlo simulation

For the present analysis the self generated point source Monte Carlo simulation described above is used. As mentioned, the main settings are the same as in the run by run Monte Carlo simulation provided by the ANTARES collaboration. The point source Monte Carlo simulation is done, because there and only there it is possible to imitate the natural process of neutrinos arriving from exactly one direction. Besides it is possible to generate as many neutrinos from each specific direction as might be desired. In contrast, the statistics of the run by run Monte Carlo simulation for specific declination regions is limited. On the other hand, the advantage of the run by run Monte Carlo simulation is obvious, it is the reason why it is generated: The run by run Monte Carlo simulation takes the changing detector and environmental conditions into account. Although in the present analysis the background is derived from data as explained in Chapter 5, the usage of the run by run Monte Carlo simulation still could enhance specificity disregarding the weaker statistics. In order to exploit the advantages of the run by run Monte Carlo production completely, a program is developed that reads the run by run Monte Carlo data for every declination range separately for each fortnight. Of course, the declinations can not be fixed as strictly as for the point source mode, so as a compromise between accuracy and the amount of statistics, intervals of 5 degrees are chosen. The declination of each selected source lies within such an interval. So in the program written for the run by run case, for every source (16) and every fortnight (102) a histogram (detailed explanation in Chapter 5) for angle and energy is created. As some sources have got similar declinations, the number of histograms is slightly smaller than $16 \cdot 102 \cdot 2$. In Figure 4.3 and 4.4 comparisons of the histograms generated with the point source Monte Carlo and the run by run Monte Carlo production are shown. In the depiction for the run by run Monte Carlo production fortnight number 3 is chosen, as it is relevant for this source (see 8). The declination of PKS 2204-540 lies in the interval chosen for the run by run Monte Carlo histogram shown. It is apparent that the histograms hardly differ in the relevant ranges. As these histograms are the only input parameters concerning angle and energy and the third input parameter, the lightcurve, is the same both in the point source and in the run by run Monte Carlo simulation, also the final results from the point source simulation and the run by run Monte Carlo simulation do not differ significantly.

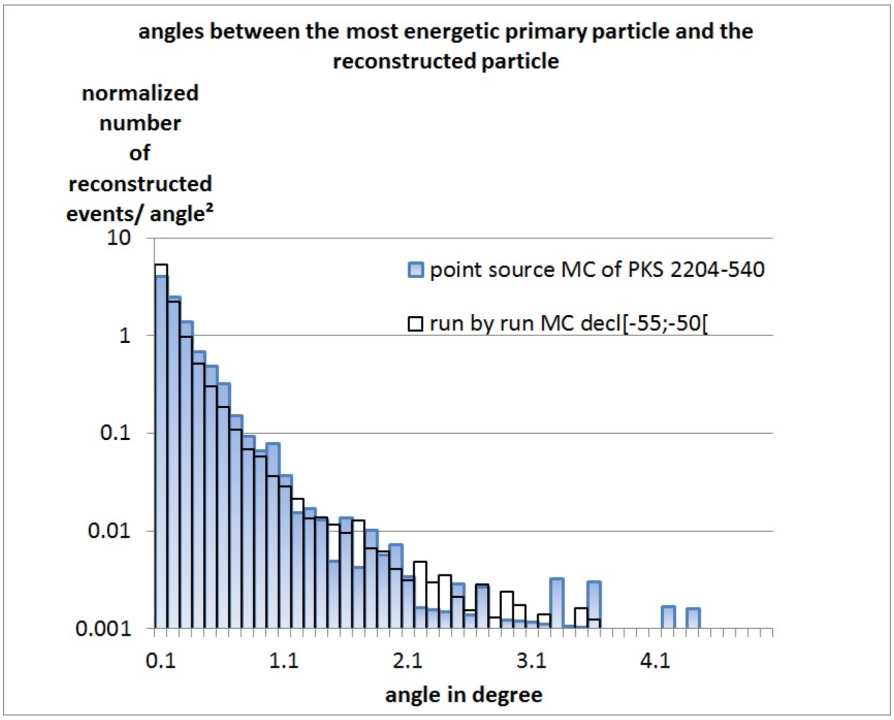

FIGURE 4.3: Comparison of the angle histograms of point source and run by run Monte Carlo

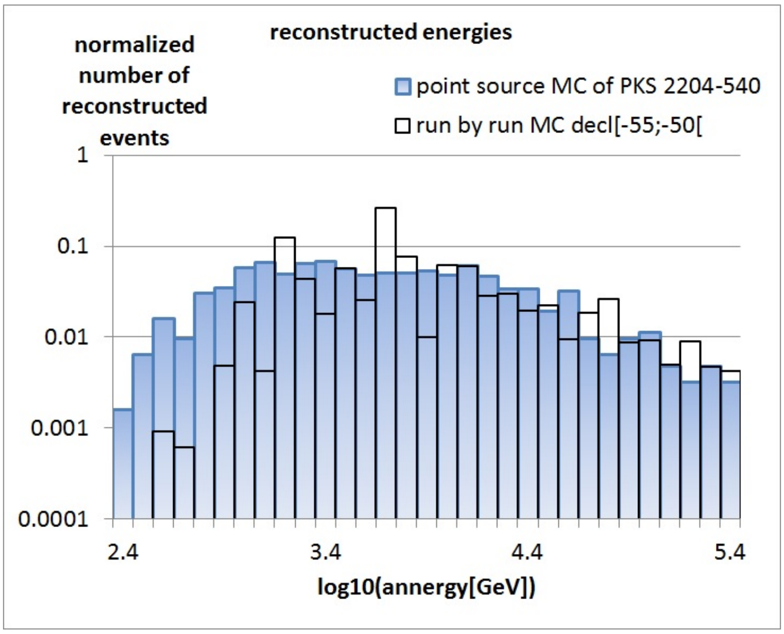

FIGURE 4.4: Comparison of the energy histograms of point source and run by run Monte Carlo

4.2 Acceptance and Flux

The acceptance depicted in Figure 4.5 is a variable that describes the ratio between the number of incoming neutrinos and reconstructed events. Depicted is the number of reconstructed events at different declinations for a flux of $10^{-7} \frac{\text{GeV}}{\text{cm}^2 \cdot \text{s}}$ for an E^{-1} and an E^{-2} spectrum. The number of reconstructed events needed for

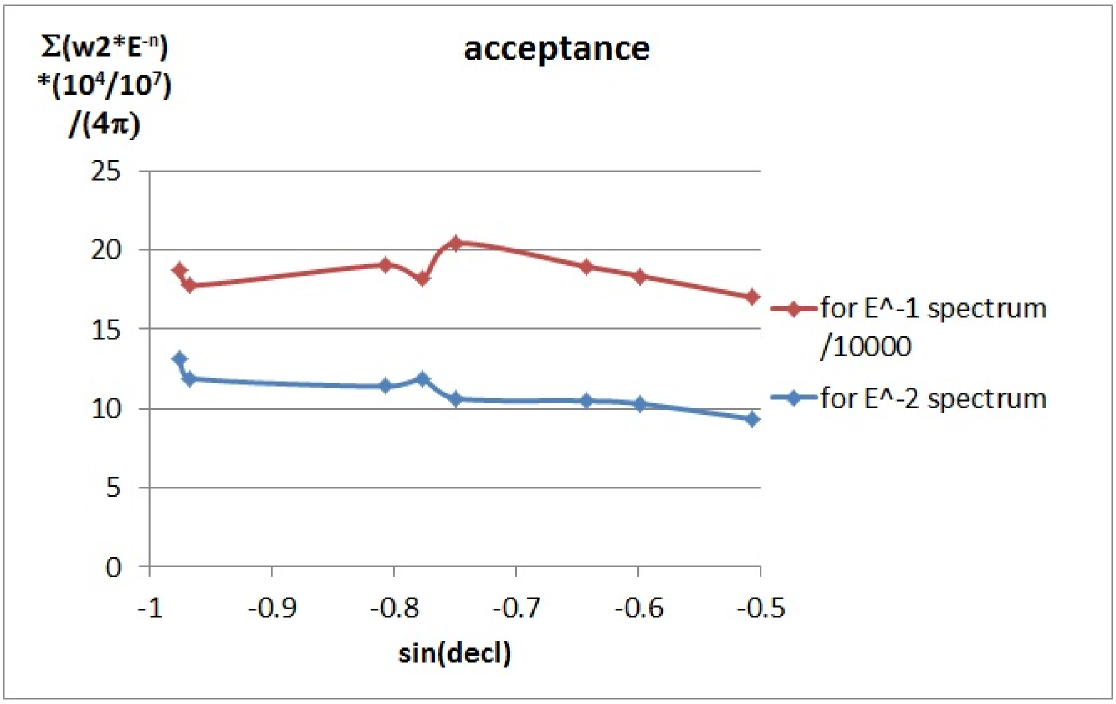

FIGURE 4.5: Acceptance

a probability of 50% for 5σ can be translated by means of the acceptance into the required flux. The flux Φ is the number of neutrinos per GeV, per second, per steradian and per cm^2. For the time one has to consider the running time of the detector, because the signals must have arrived during that time. The effective area is dependent on the energy and the angle in local coordinates. The latter can be neglected, as it changes during one day and we calculate a new time bin only every fortnight. The energy dependency can be drawn from Figure 4.6. In total 10^{10} neutrinos are generated between 10^2 and 10^8 GeV according to an E^{-1} spectrum.

$$a \cdot \int_{10^2}^{10^8} E^{-1} dE = 10^{10}$$

$$\Rightarrow a = \frac{10^{10}}{ln(10^8) - ln(10^2)} = 724 \cdot 10^6$$

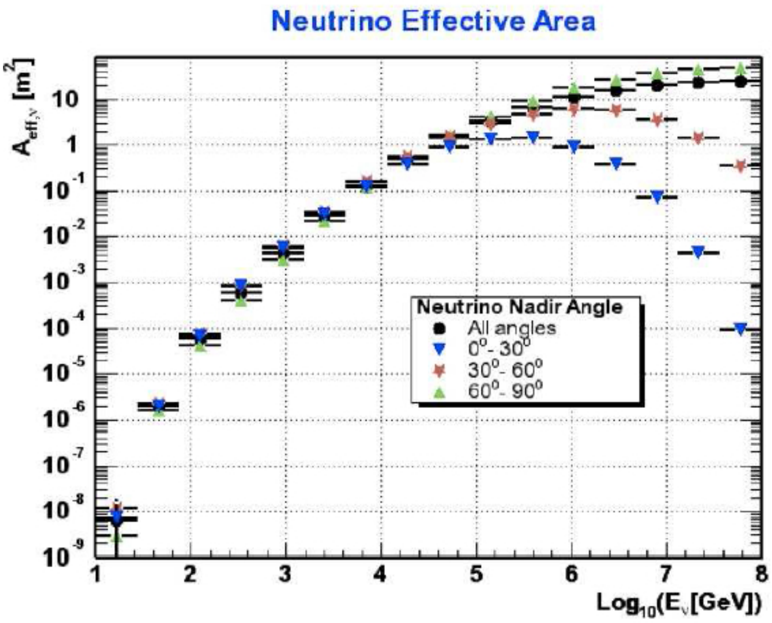

FIGURE 4.6: Effective area [Co13]

So the number of neutrinos generated per energybin is

$$724 \cdot 10^6 \cdot (ln(E_{max}) - ln(E_{min}))$$

where $log_{10}(E_{max}) = log_{10}(E_{min}) + 0.1$
$\Leftrightarrow E_{max} = E_{min} \cdot 10^{0.1}$

$$\Rightarrow 724 \cdot 10^6 \cdot (ln(E_{max}) - ln(E_{min})) = 724 \cdot 10^6 \cdot (ln \left(\frac{E_{min} \cdot 10^{0.1}}{E_{min}} \right)$$

So the content of each bin is equal: $1.\bar{6} \cdot 10^8 = 10^{10} : 60$.
For the calculation of the flux the original content of each bin has to be divided by the number of reconstructed events in this bin. The second factor is the effective area for the particular energy bin. Thirdly the running time in seconds has to be taken into account. In the present analysis, acceptance and flux are derived by the weights described in Equation 4.2. The acceptance is calculated as follows.

$$\left[\sum (w_2 \cdot E^{-n}) \cdot 10^4 \cdot 10^{-7}\right] : (4\pi) \tag{4.4}$$

The factor 10^4 comes from the conversion of m^2 into cm^2, the factor from the flux it is normalized to and the division by 4π is necessary due to the solid angle GENHEN operates on assigning weights.

4.3 Comparison of data and Monte Carlo simulation

As it is explained in Chapter 5, the number of background events is taken from data. The true astrophysical signals from data are not known a priori and therefore neither the angle nor the energy distribution from the Monte Carlo simulation can be compared with a counterpart from data. The only parameter for which a comparison of data and Monte Carlo simulation can be performed for the time dependent point source search is the energy of the background events. As the estimation of the energy is done with the ANN module (see 3.6), first the general agreement between data and Monte Carlo simulation for this energy estimator is tested (see Figure 4.7). Due to the fact that for a fixed declination and right ascension of a source, the local zenith and azimuth of the directions of the arriving neutrinos change with time, this influence is also investigated (see Figure 4.8). Then specifically for the present analysis a comparison of energies of the data and the energies of the point source Monte Carlo weighted with the Bartol flux is performed. Plotted in Figure 4.9 is the result for a declination range within which among others the source PKS 2204-540 is. While Figures 4.7 and 4.8 use as input parameters the run by run Monte Carlo production v2.2 and data from 0 ending runs from 2008 to 2011, figure 4.9 shows the point source Monte Carlo simulation and energies from runs from the time period relevant for the present analysis (see 5). The plots are produced with the cuts beta < 1 and lambda > -5.2. The purity for these cuts is 87% (see [Ad12]). This number reflects that after applying these cuts, according to the evaluation of the Monte Carlo simulation, 13% of the number of reconstructed events are atmospheric muon events erroneously reconstructed as upgoing neutrino events.

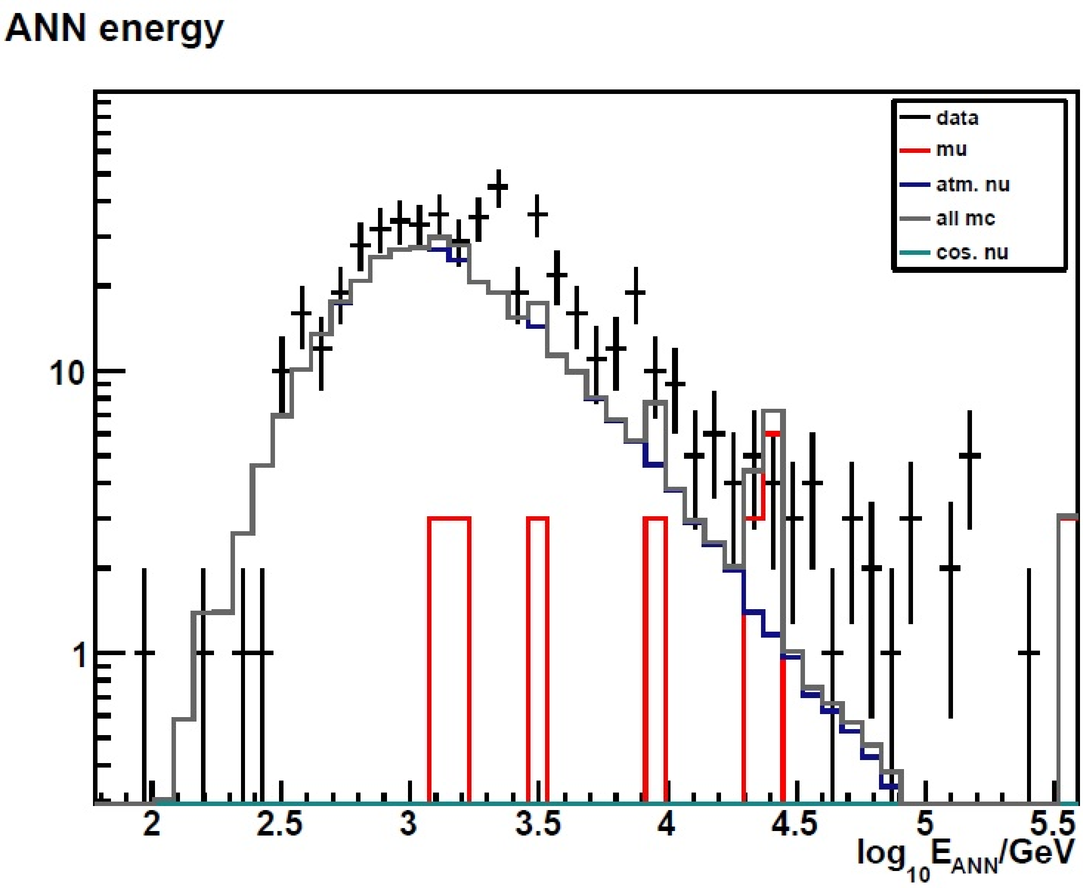

FIGURE 4.7: Comparison of data and monte carlo for background energies, courtesy of Jutta Schnabel

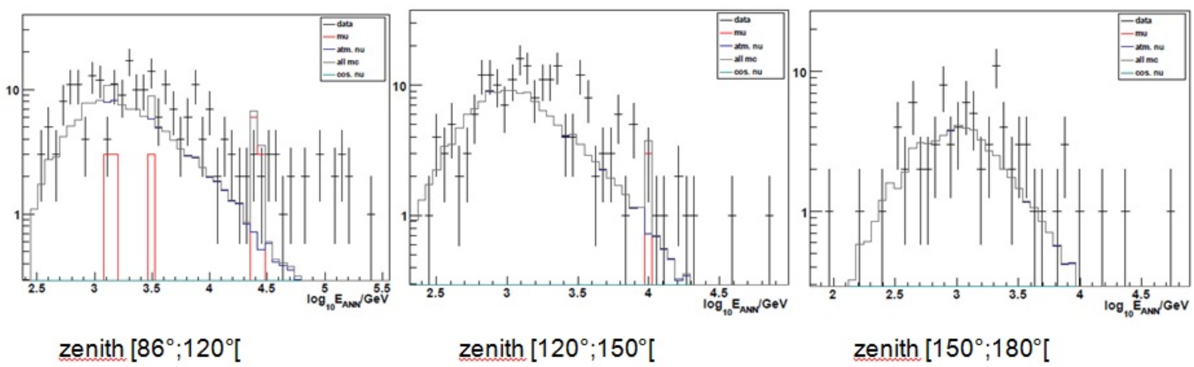

FIGURE 4.8: Comparison of data and monte carlo for different zenith bands, courtesy of Jutta Schnabel

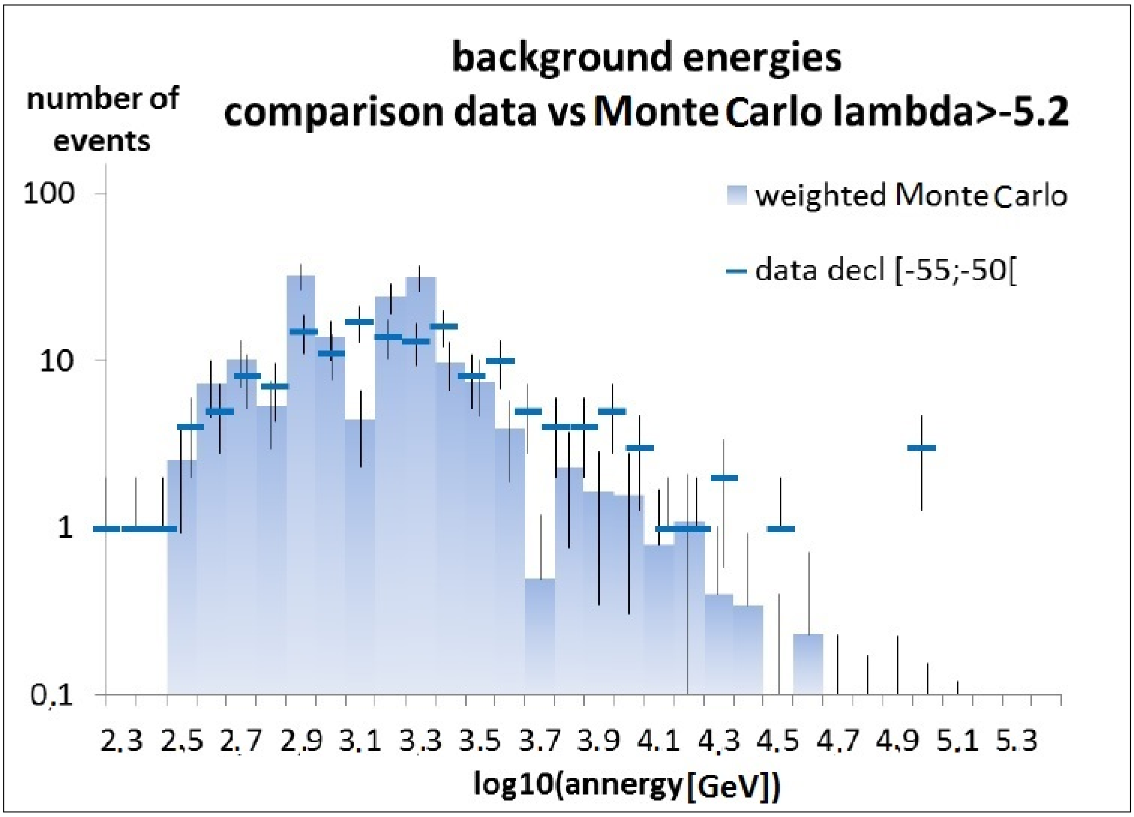

FIGURE 4.9: Energy spectra

Chapter 5

Analysis

For a measured event it is not known whether it is a signal or it is part of the background. For each event the three observables reconstructed angle, reconstructed energy and time are available. To distinguish signal events from background events, assumptions on the special properties of signal events have to be made. The obvious assumption for a point source analysis is that the signal comes from the source. Regarding energy we expect that the spectrum of the signal events differs significantly from the atmospheric spectrum. To account for the acceleration process in AGN, this analysis starts from the premise that neutrinos are emitted simultaneously with the detected gamma photons.These three issues go into the simulation of the signal described in detail below: For N events detected the contribution n_s of signal events is not known $\grave{a}$ priori. To determine the contribution, an unbinned maximum likelihood method is applied. $\frac{n_s}{N}$ is the fraction of signal events, $\left(1 - \frac{n_s}{N}\right)$ is the fraction of background events. In order to obtain the best fit value $\hat{n_s}$ the likelihood L of the data is maximized with respect to n_s.

$$L(n_s) = \prod_{i=1}^{N} \left[\frac{n_s}{N} S_i + \left(1 - \frac{n_s}{N}\right) B_i\right] \tag{5.1}$$

where

n_s	unknown contribution of the signal events
N	number of events
$S_i = \mathcal{N}_s(\alpha_i) \times \mathcal{T}(T_i) \times \mathcal{E}_s(E_i)$	signal probability density
$B_i = \frac{1}{5^2 \cdot \pi \cdot 0.1 \cdot 102} \cdot \frac{n}{\bar{n}} \times \mathcal{E}_b(E_i)$	background probability density

the first factor in B_i is for normalization with 5^2 because of the search cone of 5 deg with 0.1 deg binwidth and 102 for the number of time bins. $\frac{n}{\bar{n}}$ accounts for the time dependency of the background with n number of events in the specific time period and $\bar{n}$ mean number of events cf. [Ad13].

$\mathcal{N}$	probability function for the angle to the source
	normalized height of the histogram of (number of angles)/angle
$\mathcal{N}_s$	from source Monte Carlo with E^{-1} spectrum
	generated with genhen and km3, reconstructed with Aafit
$\mathcal{T}$	probability function for the time of the event
	normalized height of the lightcurve of the source
$\mathcal{E}$	probability function for the energy
	normalized height of the histogramm of reconstructed energies
$\mathcal{E}_s$ respectively $\mathcal{E}_b$	from source Monte Carlo with E^{-1}
	generated with genhen and km3
	reconstructed with ANNergy
	respectively from weighted energy spectrum

Dissident from the standard way of calculating the test statistic (e.g [Br10]) above, a slightly different method was used in previous ANTARES papers. In the following the two methods are compared. While the method used in this analysis does not make an explicit assumption about the background, the other method takes the background as known:

$$logL_{s+b} = \sum_i \left[\mu_s \times \mathcal{F}(\psi_i(\alpha_s, \delta_s)) \times N^s(N^i_{hits}) + B(\delta_i) \times N^{bg}(N^i_{hits})\right] - \mu_s - \mu_{bg} \tag{5.2}$$

$\mathcal{F}$	probability density function	$\equiv \mathcal{N}(r_i)$
	of reconstructing event i	
	at an angular distance ψ_i	
	from the source location (α_s, δ_s)	
N_{hits}	indicator of energy	$\equiv \mathcal{E}(E_i)$
μ_s	mean number of signal events	$\equiv n_s$
μ_{bg}	number of background events	$\equiv N - n_s$
$B(\delta)$	parametrisation	$\equiv B_i$
	the background rate	

(first and second column cited from [Ad12])

$$\begin{aligned}
logL_{s+b} &= loga + logb - (\mu_s + \mu_{bg}) \\
logL_{s+b} &= log(a \cdot b) - (\mu_s + \mu_{bg}) \\
logL_{s+b} + \mu_s + \mu_{bg} &= log(a \cdot b) \\
L_{s+b} \cdot 10^{\mu_s + \mu_{bg}} &= a \cdot b \\
L_{s+b} &= \frac{a \cdot b}{10^{\mu_s + \mu_b}}
\end{aligned}$$

$$L_{s+b} = \frac{\prod_i (n_s \cdot S_i + B_i)}{10^N} \qquad Q = -log_{10} \frac{\prod_i B_i}{\prod_i (\hat{n}_s \cdot S_i + B_i)}$$

$$L(n_s) = \frac{\prod_i (n_s \cdot S_i + (N - n_s) \cdot B_i)}{N} \qquad D = -2log_{10} \frac{\prod_i (N \cdot B_i)}{\prod_i (\hat{n}_s \cdot S_i + (N - \hat{n}_s) \cdot B_i)}$$

As the expected background is drawn from data, the methods do not differ much in the present analysis.This is a conclusion not only from analytical considerations, but also from the simulation depicted in Figure 5.1.

Although for a reconstructed event from data it is not known whether it is signal or background, considering a Monte Carlo event we can distinguish between signal and background and hence calculate the sensitivity. Four cases have to be minded: It is a signal event and we think it is a signal event, it is a signal event and we think it is background, it is background and we think it is a signal event and it is background and we think it is background. When it is a signal event, angle and energy are chosen from the signal Monte Carlo simulation, time is chosen randomly in the treated time interval.

An overview of the analysis gives Figure 5.2. In the following, the individual terms for the likelihood are described in more detail.

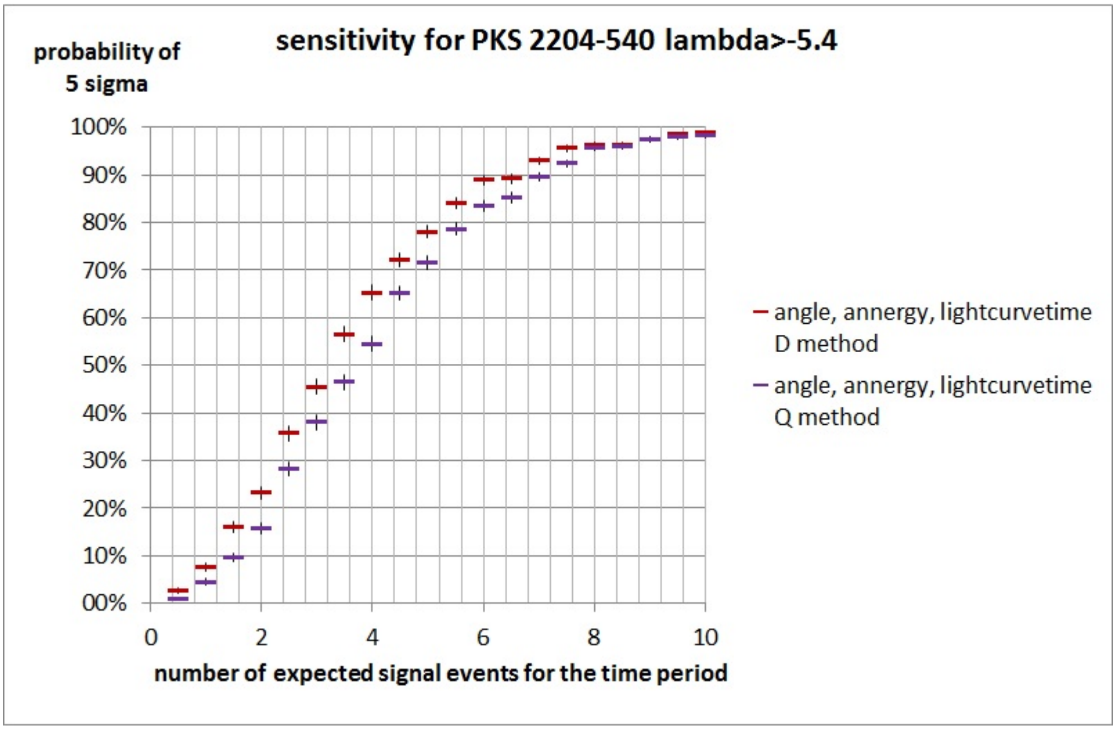

FIGURE 5.1: Comparison of two methods of calculating the test statistic

		signal event	background event
expectation μ		0.5, 1.0, 1.5, ..., 10.0	#
S-term	angle	from E^{-1} MC (angle1, angle2, ...) height from E^{-1} MC	~ sin α
	energy	(energy1, energy2,...)	from $E^{-3.6}$ MC energy height from E^{-1} MC
	time	from cumulated lightcurve	random
B-term		$\frac{1}{5^{\circ 2}\pi} \cdot \underbrace{\text{energy}}_{\text{from } E^{-1} \text{ MC}}$ height from $E^{-3.6}$ MC	$\frac{1}{5^{\circ 2}\pi} \cdot \underbrace{\text{energy}}_{\text{from } E^{-3.6} \text{ MC}}$ height from $E^{-3.6}$ MC

FIGURE 5.2: Scheme of the analysis

5.1 Angle term

As the signals are expected to originate from an AGN, for each source a Monte Carlo simulation is done with GENEHEN v6r10 in point source mode, simulating 10^{10} neutrinos in each case. After propagation with KM3, the events are reconstructed with Aafit using varying cuts of the quality parameter lambda. The second quality parameter beta has only got a small impact (see Figure 5.16) on the results, therefore it is firstly fixed to 1. The coordinates of the events are transformed from local coordinates to equatorial coordinates via the astropackage, which is comparable to the transformation implemented in the program written for the analysis. Afterwards, the angle of each event to the particular source is calculated with the well known formula.

$$\alpha = \arccos\left(\frac{\cos(d)\cdot\cos(a)\cdot\cos(d_S)\cdot\cos(a_S)+\cos(d)\cdot\sin(a)\cdot\cos(d_S)\cdot\sin(a_S)+\sin(d)\cdot\sin(d_S)}{\sqrt{(\cos(d)\cdot\cos(a))^2+(\cos(d)\cdot\sin(a))^2+(\sin(d))^2}\cdot\sqrt{(\cos(d_S)\cdot\cos(a_S))^2+(\cos(d_S)\cdot\sin(a_S))^2+(\sin(d_S))^2}}\right)$$

α angle to the source

d declination of the reconstructed origin of the event

d_s declination of the source

a right ascension of the reconstructed origin of the event

a_s right ascension of the source

The angles of the reconstructed events which passed the cuts are filled into a histogram with bins of 0.1 degree from 0 to 5 degrees. This histogram is normalized by division by its area. The normalized histogram of angles to the source serves for each source of the sample as part of the likelihood of the signal. The likelihood of the background is assumed to be constant with respect to the angles to the source (see 5 above).

In case of a signal the angle is chosen from the vector of angles of the reconstructed events from the Monte Carlo point source simulation (see Figure 5.3). In case of background the angle is chosen from a uniform distribution of angles to the source, which is approximately proportional to $\sin(\alpha)$ because of the outwardly increasing area on the sphere cup.

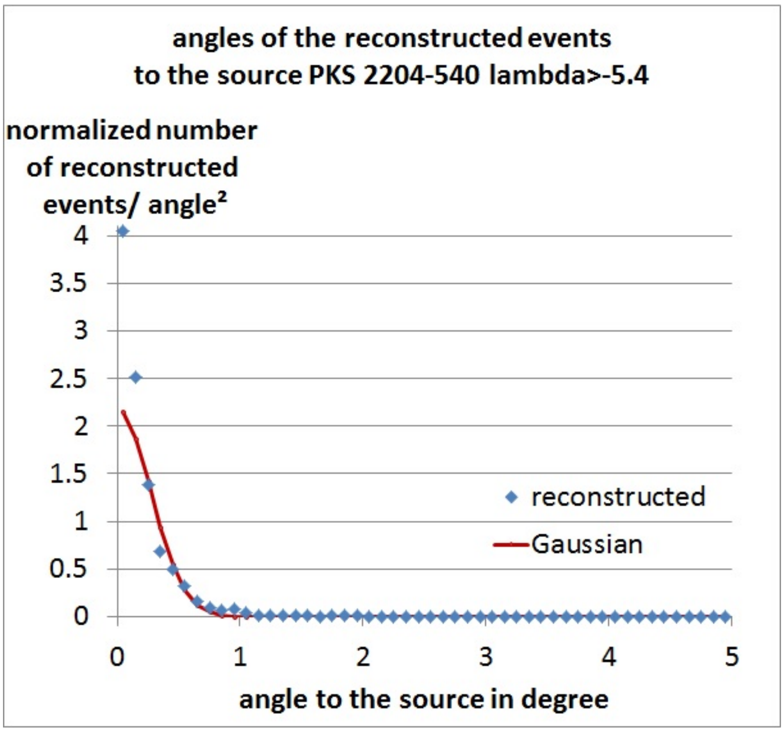

FIGURE 5.3: Angles to the source compared to Gaussian with $\sigma = 0.3$
For the analysis not the Gaussian, but the distribution of angles for each source is used.

5.2 Time term

The time variable approach is the gist of the present analysis. Thus normalized lightcurves from Fermi observations produced with Fermi tools by Cornelia Müller are applied as likelihood in time. It was decided upon a fortnight binning as smallest available binning with tolerable number of upper limits in the lightcurve. The likelihood for background is approximately uniform in time with a correction factor for the rate (see 5.6).

As neutrinos are expected to arrive coincident with gamma rays, in the signal case the times are chosen from the cumulative distribution function of the relevant lightcurve. In the background case, times are chosen randomly between the 102 time intervals from 01.09.2008 to 30.07.2012. First Fermi data are available from 06.08.2012, when in ANTARES line 1 cable was being repaired. So the time intervals of the ANTARES 12 line detector and Fermi observation period fit well starting with ANTARES run 35147, ending with run 65821 with a total running time of 86940135 s. For the calculation of the correction factor data of the official data productions prod_2012-04 for 2008-2011 and prod_2013-06 for 2012 were used. 107 of the 50703 + 5569 files were broken. As the results of each run are

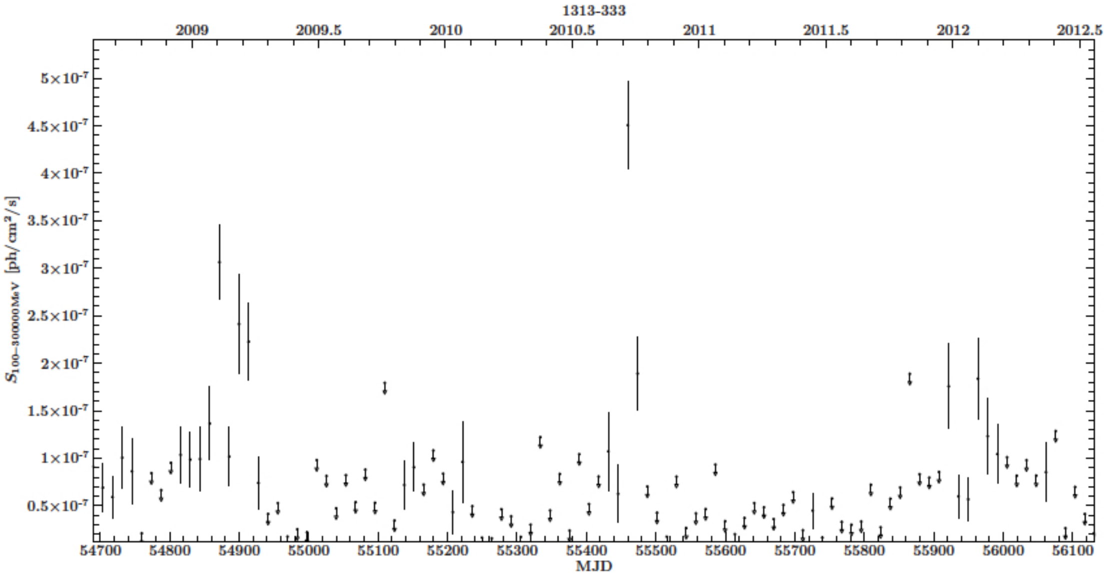

FIGURE 5.4: Lightcurve of PKS 1313-333, courtesey of Cornelia Müller

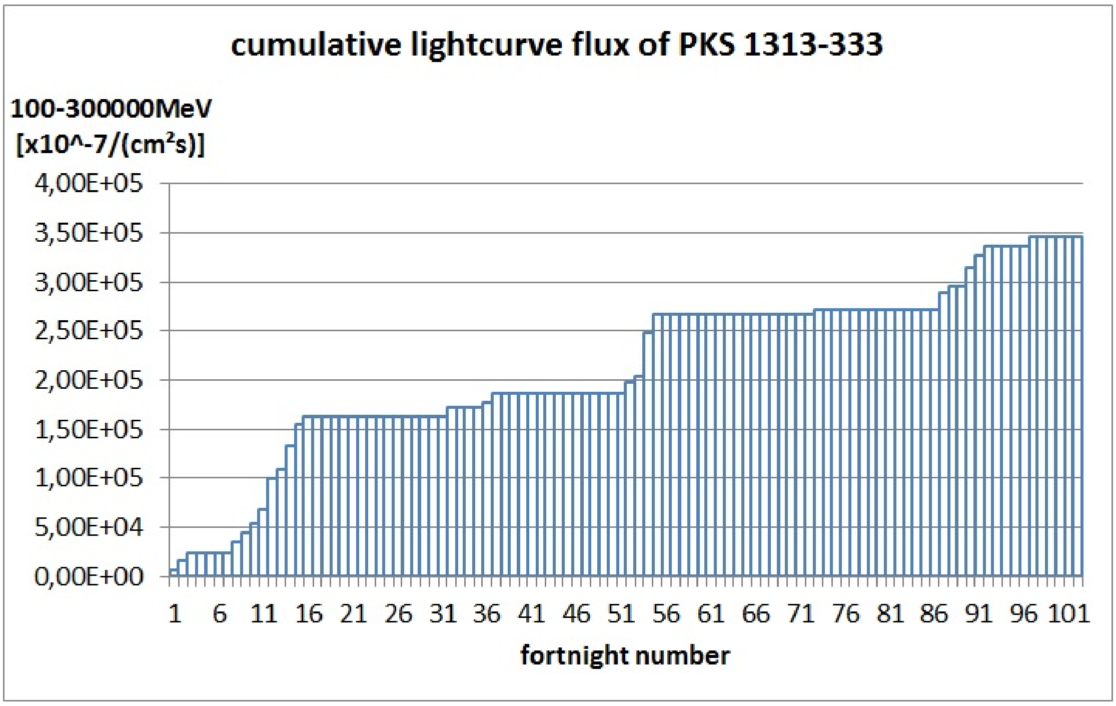

FIGURE 5.5: Cumulative lightcurve, from which the times for signal simulation are drawn

divided into many files, all runs of the production with existing data were taken into account for the calculation of the correction factor.

5.3 Energy term

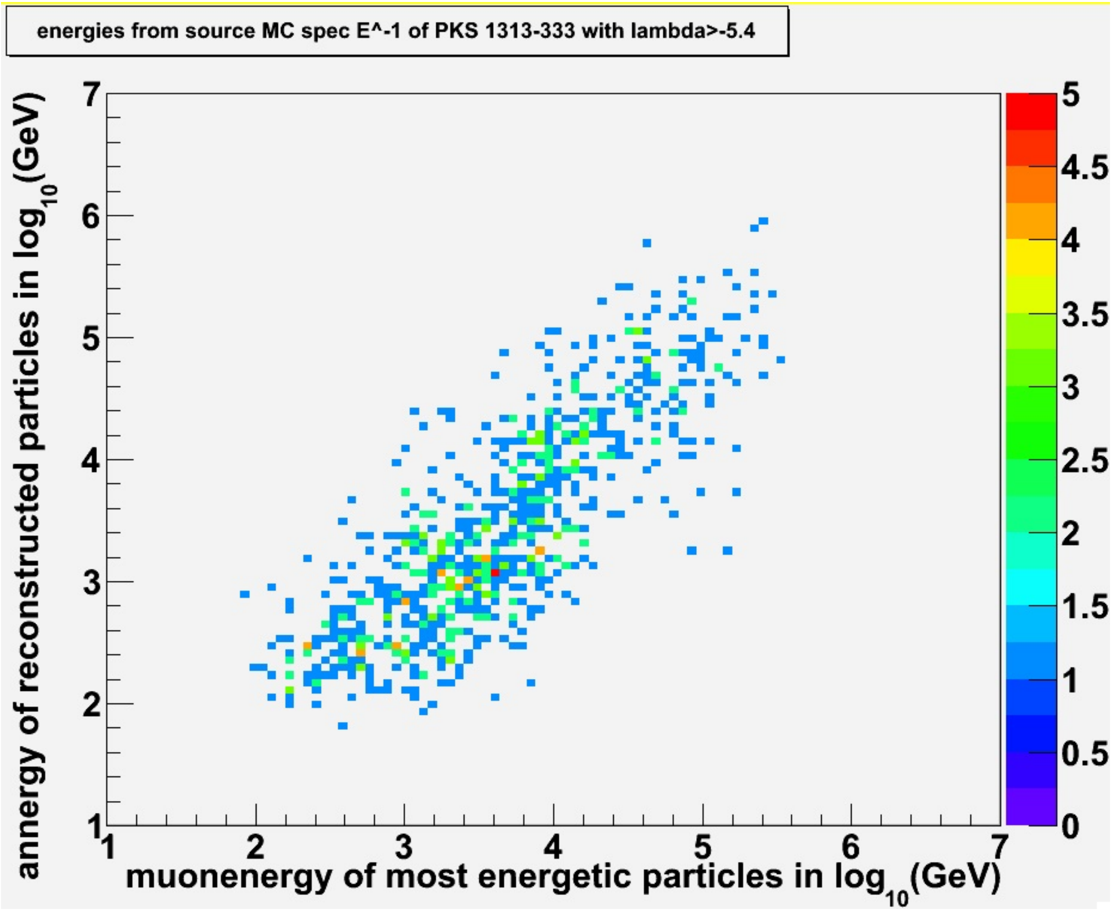

FIGURE 5.6: Energy of muon vs reconstructed energy with ANNergy

Recent theories, e.g. [Re12], [Ma00], [MP14] predict a flat neutrino energy spectrum for AGN (see 2.2). Therefore an E^{-1} spectrum is chosen in the genhen point source simulation. The energy range is as mentioned in 4.1 from 10^2 to 10^8 GeV.

The reconstructed energies of the generated events are weighted according to Equation 4.3 by $w_{\text{generation}} \equiv w_2$ and filled into a histogram with logarithmic bins of 0.1 $\log_{10}$ GeV. The normalized histogram serves as likelihood for signal energy. In the signal case, the energies are sampled from this histogram Figure 5.7 considering the corresponding angles as follows: First the energy bin is adopted according to the distribution of the histogram. Then a specific energy value from the vector of reconstructed energies lying in that bin is chosen according to its weight (see Figure 5.8). As third step the corresponding angle from the vector of reconstructed angles is selected. For background the reconstructed energies from particular

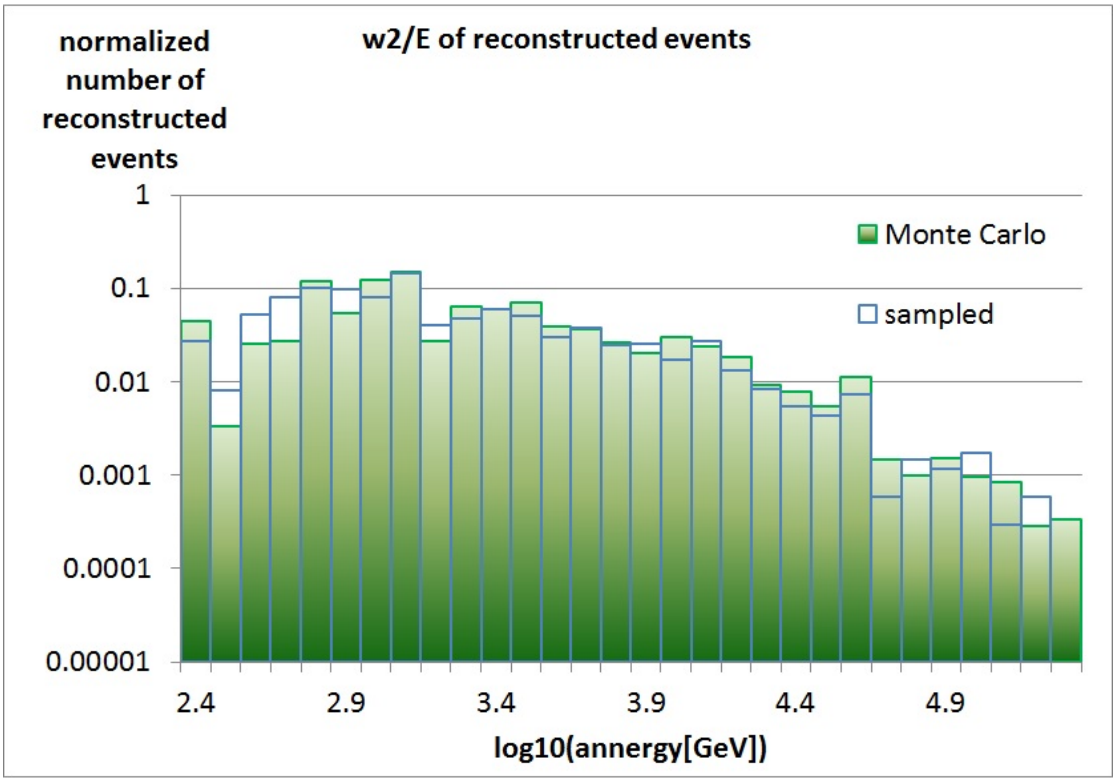

FIGURE 5.7: Comparison of the histogram from which the energybins are sampled (Monte Carlo) and the histogram of the actually chosen bins (sampled)

declination bands over the whole time period are considered and compared to the energies derived weighting the events by the so called global weight w3 that includes the Bartol flux. The normalized histograms of these energy distributions serve as likelihood for background energy.

As events with higher energies tend to get reconstructed better, the conditional probability $P_\alpha(E)$ has to be considered: $P(\alpha \cap E) = P(\alpha) \cdot P_\alpha(E) \stackrel{?}{=} P(\alpha) \cdot P(E)$. To investigate the effect, reconstructed energies for different angle intervals have been tested. The reconstructed energy seems to be appoximately independent of the angle of the reconstructed event (see Figure 5.9).

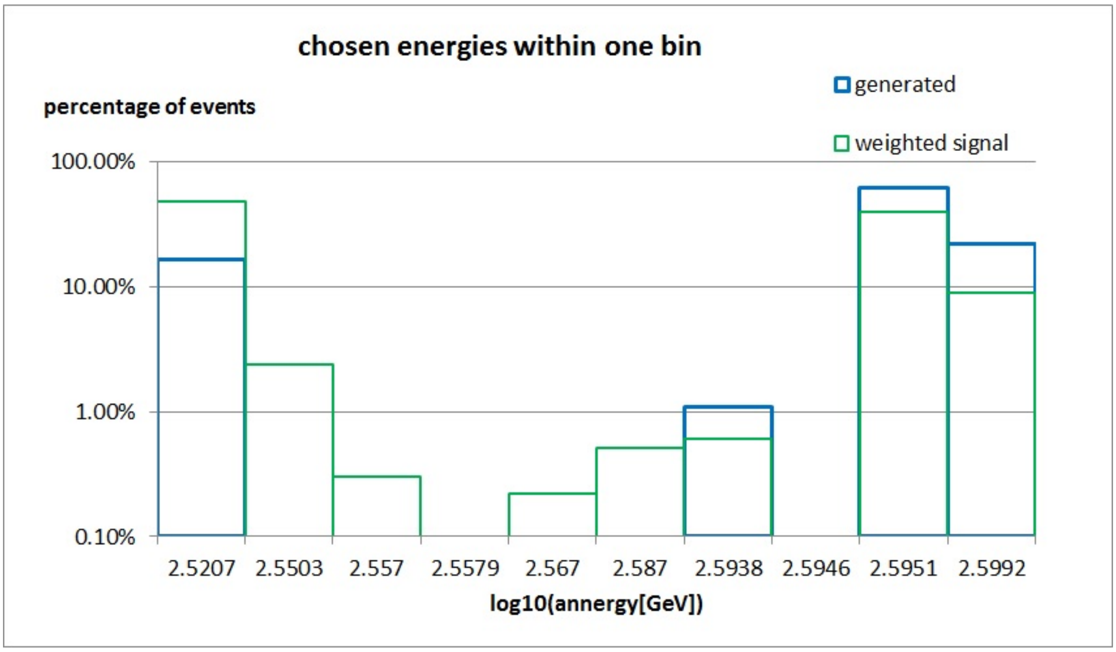

FIGURE 5.8: Distribution of energies within one bin
In the pseudo experiments this bin was hit 183 times. The distibution of the chosen energies (generated) corresponds to the distribution of weighted signals.

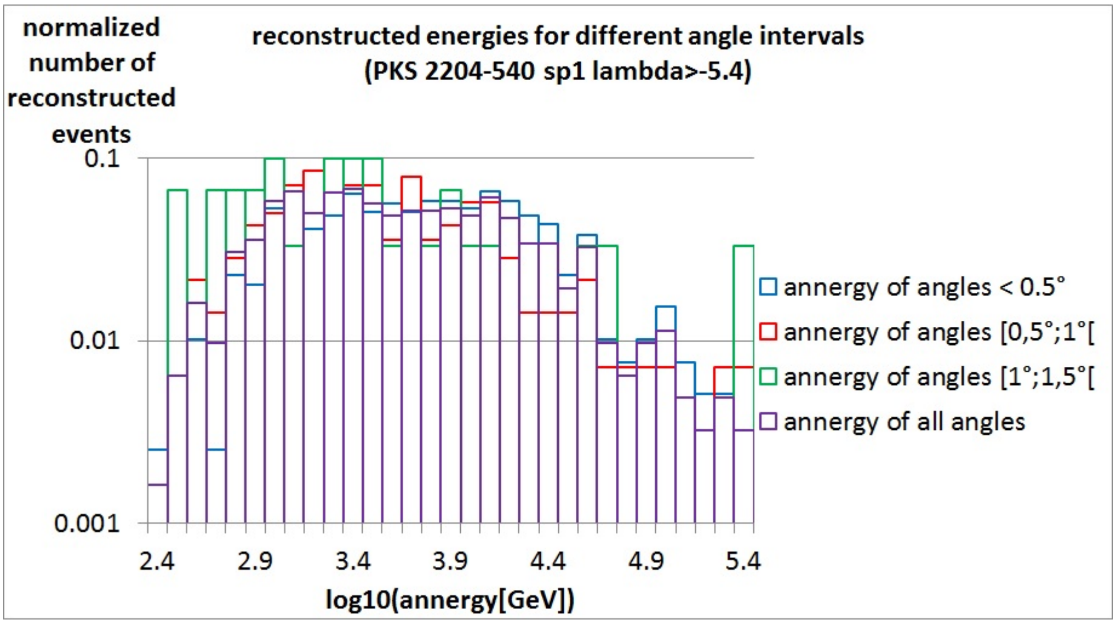

FIGURE 5.9: Energy and angle are almost independent.

5.4 Background rate

The background rate in Figure 5.10 is derived from data as follows. The number of events over the whole time period in declination bands of 5 degrees is counted with varying lambda cuts from -6.0 to -4.9. The number of steradians in a sphere cup of 5 degrees divided by the number of steradians of a declination band of 5 degrees times the measured number gives an approximation of the background in a 5 degree cone around the particular source (see Figure 5.11).

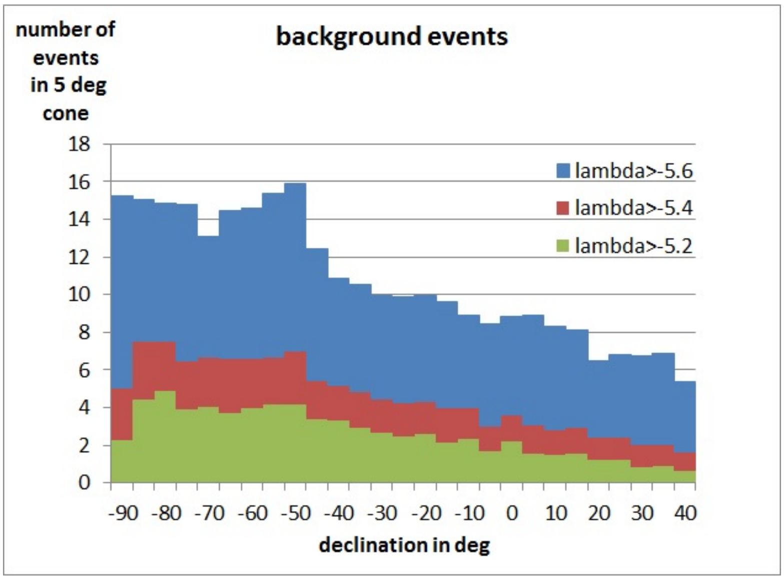

FIGURE 5.10: Background

TABLE 5.1: Number of background events

declination (start)	-75	-70	-65	-60	-55	-50	-45	-40
rad	-1.31	-1.22	-1.13	-1.05	-0.96	-0.87	-0.79	-0.70
number of sr in decl band	0.16	0.21	0.25	0.29	0.33	0.37	0.40	0.43
number of upgoing events	1214	1466	1862	2329	2767	3220	2691	2377
	684	781	1024	1236	1527	1755	1458	1343
	407	460	611	720	859	984	840	789
	257	322	380	469	519	626	533	532
	178	234	279	324	370	434	364	376
	135	190	204	250	290	335	285	306
	108	142	158	196	232	259	227	243
	87	121	138	155	192	209	184	193
	69	92	111	124	162	174	150	159
	51	65	88	95	125	140	121	130
number of sr in 5°	$5.98 \cdot 10^{-3}$	$5.98 \cdot 10^{-3}$	$5.98 \cdot 10^{-3}$	$5.98 \cdot 10^{-3}$	$5.98 \cdot 10^{-3}$	$5.98 \cdot 10^{-3}$	$5.98 \cdot 10^{-3}$	$5.98 \cdot 10^{-3}$
events in 5° lambda 5.8	$4.40 \cdot 10$	$4.18 \cdot 10$	$4.40 \cdot 10$	$4.73 \cdot 10$	$4.96 \cdot 10$	$5.20 \cdot 10$	$3.98 \cdot 10$	$3.27 \cdot 10$
events in 5° lambda 5.7	$2.48 \cdot 10$	$2.23 \cdot 10$	$2.42 \cdot 10$	$2.51 \cdot 10$	$2.74 \cdot 10$	$2.83 \cdot 10$	$2.16 \cdot 10$	$1.85 \cdot 10$
events in 5° lambda 5.6	$1.48 \cdot 10$	$1.31 \cdot 10$	$1.44 \cdot 10$	$1.46 \cdot 10$	$1.54 \cdot 10$	$1.59 \cdot 10$	$1.24 \cdot 10$	$1.09 \cdot 10$
events in 5° lambda 5.5	9.32	9.18	8.98	9.52	9.30	$1.01 \cdot 10$	7.89	7.32
events in 5° lambda 5.4	6.46	6.67	6.59	6.58	6.63	7.01	5.39	5.17
events in 5° lambda 5.3	4.90	5.42	4.82	5.08	5.20	5.41	4.22	4.21
events in 5° lambda 5.2	3.92	4.05	3.73	3.98	4.16	4.18	3.36	3.34
events in 5° lambda 5.1	3.16	3.45	3.26	3.15	3.44	3.38	2.72	2.65
events in 5° lambda 5.0	2.50	2.62	2.62	2.52	2.90	2.81	2.22	2.19

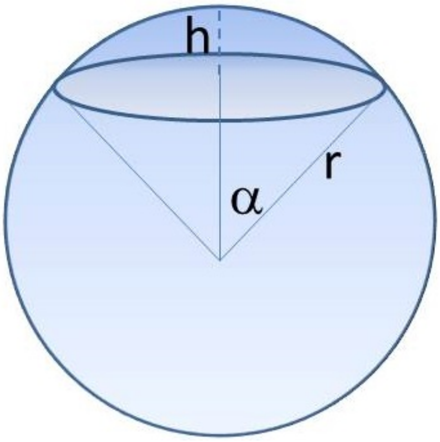

FIGURE 5.11: Surface area of the sphere cup

$$\begin{aligned}
A_{\text{sphere cup}} &= 2\pi r h && (5.3)\\
\cos(\alpha) &= \frac{r-h}{r} && (5.4)\\
\Rightarrow A_{\text{sphere cup}} &= 2\pi r^2(1-\cos(\alpha)) && (5.5)\\
\text{solid angle}_{\text{sphere cup}} &= \frac{A_{\text{sphere cup}}}{A_{\text{sphere}}} = \frac{2\pi r^2(1-\cos(\alpha))}{4\pi r^2} && (5.6)\\
\text{solid angle}_{\text{declination band}} &= \int\limits_{\delta_{\min}}^{\delta_{\max}} 2\pi\cos(\delta)\mathrm{d}\delta = 2\pi(\sin(\delta_{\max}) - \sin(\delta_{\min})) && (5.7)
\end{aligned}$$

In order to consider time dependent effects for the background, too, a correction factor depicted in Figure 5.12 is introduced (cf. [Ad13]). The number of events from all directions over all times including up- and downgoing events is calculated and hence the mean number for the runs in the fortnight considering the running time in each fortnight. In the next step the number of events for the runs in the fortnight is calculated. So the correction factor for one specific fortnight is the ratio of the number of the events and the mean number of events.

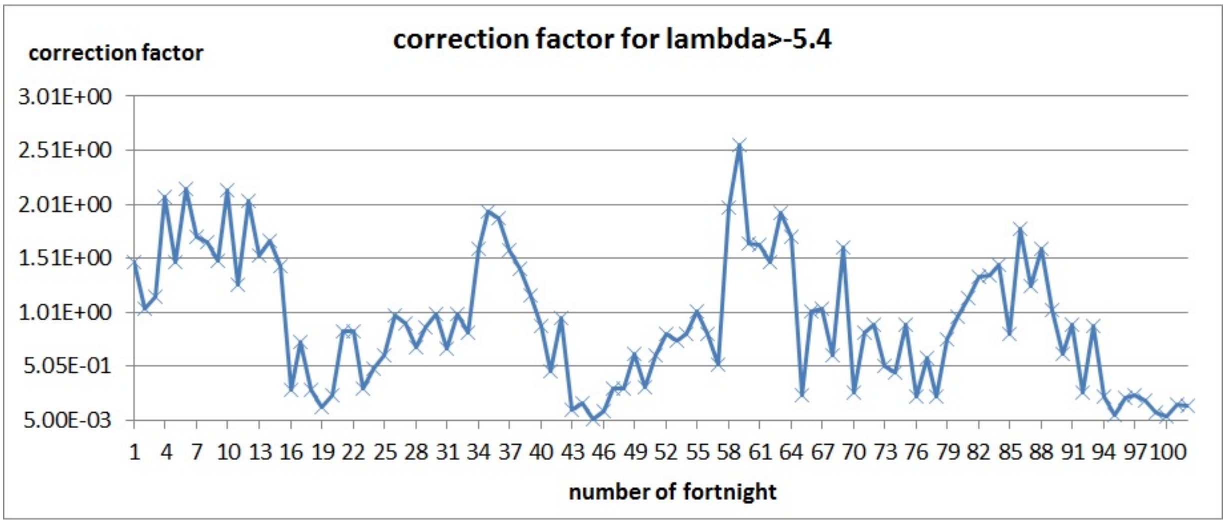

FIGURE 5.12: Correction factor

5.5 Pseudo experiments

The background rate functions as Poissonian mean for the background events that are to be generated per run of the program. For the background only case, 10^7 pseudo experiments are performed, for the signal and background case for each expected flux 1000 pseudo experiments are conducted. The performance of the method is shown in Figure 5.13.

Table 5.2 summarizes the steps of the analysis.

TABLE 5.2: Steps of the analysis

I. background from data	II. angular resolution from source MC	III. simulation of background and signal
number of events in latest data production 12-04-prod	genhen v6r10	number of events from poisson distribution:
in declination bands of 5 degrees	point source mode	(zenith, azimuth, time)
	km3 Aafit	angle to the source, height of lightcurve
running time of the detector in the data production 12-04-prod	calculation of the angles of the reconstructed events to the source	comparison of the distribution of D-values of simulated background and signal

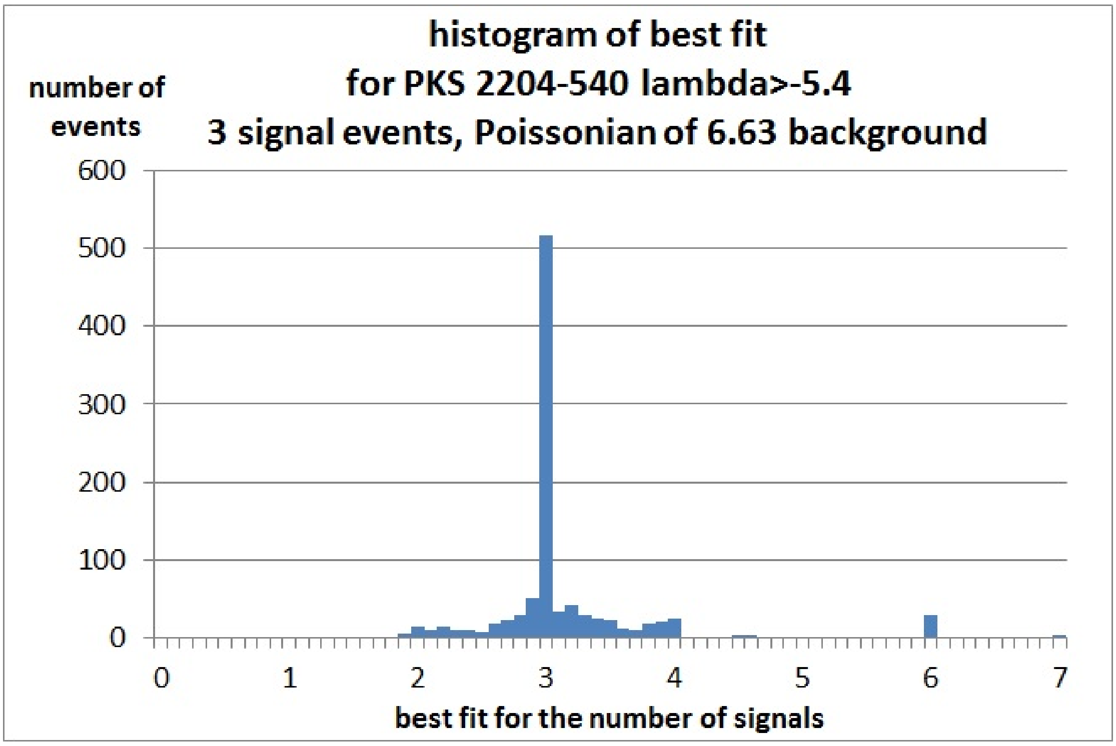

FIGURE 5.13: Histogram of best fit for number of signals $\hat{n}_s$ for $n_s = 3$

5.6 Calculation of the test statistic

For the signal and background case and for the background only case the values of the test statistic D are calculated (see Figure 5.14).

$$D = -2log\left[\frac{L(n_s = 0)}{L(\hat{n}_s)}\right] \tag{5.8}$$

The fraction of D values in the signal and background case greater than the second greatest D value out of 10^7 D values in the background only case gives the probability of 5 sigma. This can also be fitted by $f(D) = a \cdot 10^{-bD}$.

$$\begin{aligned}
\int_x^c a \cdot 10^{-b \cdot D}\, dD &= 0.1 \cdot \frac{1}{2} \cdot 99.9999426697\% \cdot 10^7 \\
\left[\frac{a}{-b \cdot ln10} \cdot 10^{-b \cdot D}\right]_x^c &= 0.2866515 \\
x &= -\frac{1}{b} \cdot log_{10}\left(0.286551 \cdot \frac{b \cdot ln(10)}{a} + 10^{-b \cdot c}\right)
\end{aligned}$$

In the example shown in Figure 5.15 the value calculated from the fit is 10.63 and the second greatest value is 10.74.

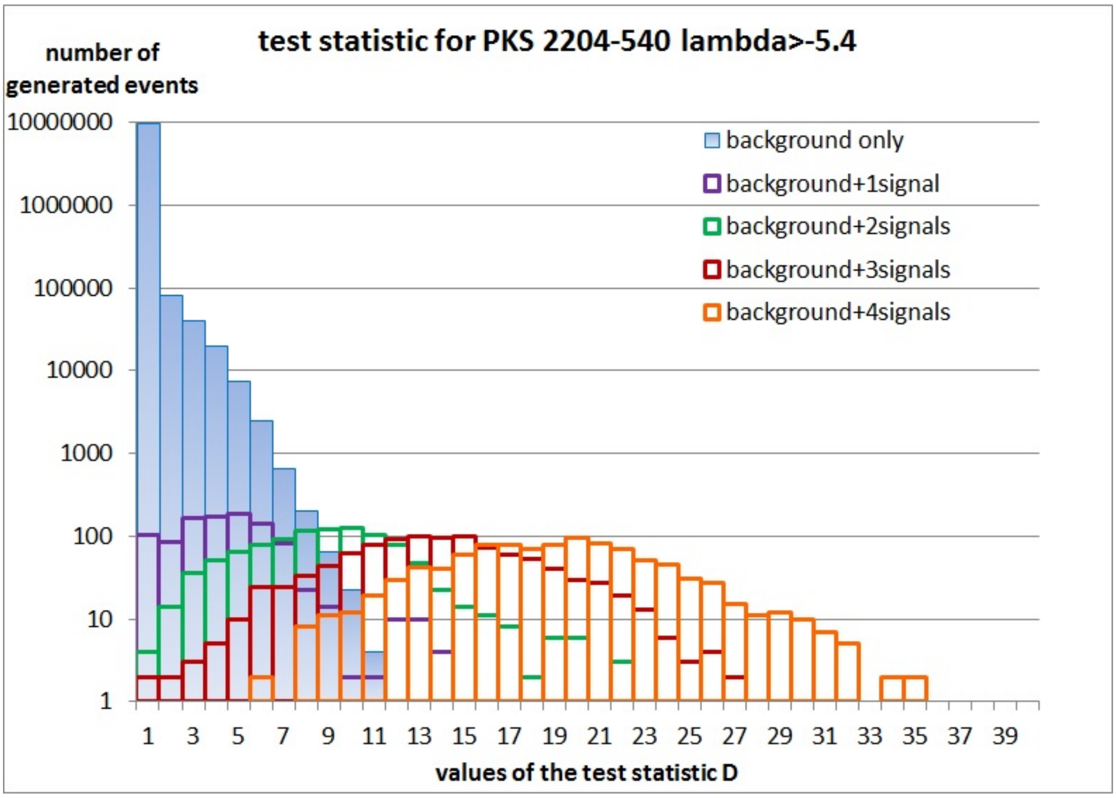

FIGURE 5.14: Distribution of test statistics for background only case and for background and signal cases

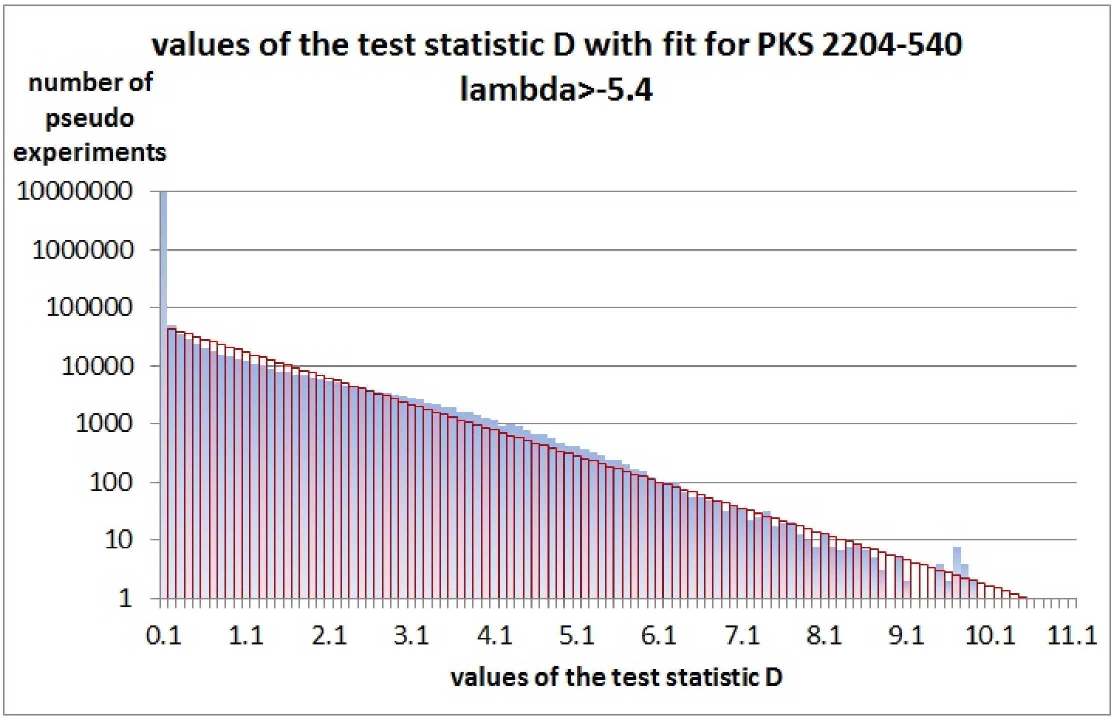

FIGURE 5.15: Fit: $50423 \cdot 10^{-0.45 \cdot D}$, minimized sum of squared differences: 2.34

5.7 Sensitivity and optimization

Before combining the factors, the cuts are optimized source by source. Figure 5.16 shows that the chosen beta cut, which equals 1, is fine. The optimal lambda cut is gained when the quotient of the number of reconstructed events in the source monte carlo and the number of events needed for a 50% change of a 5σ discovery is maximal (see Table 5.3). Thus first the sensitivities for the single

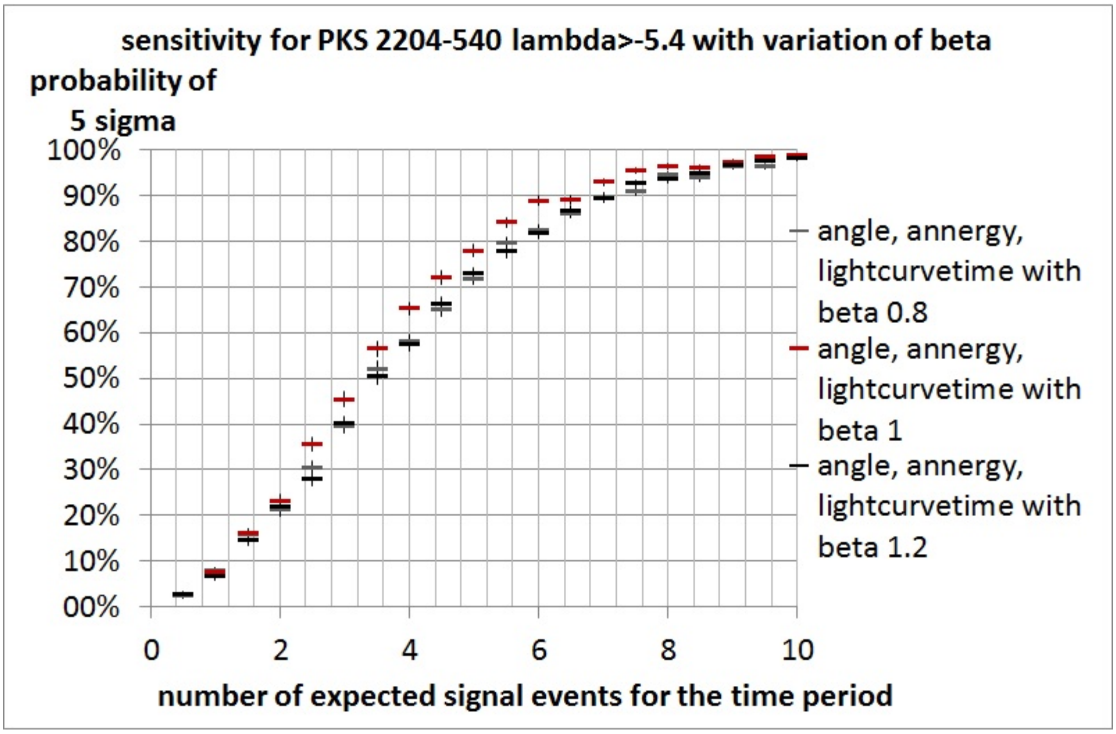

FIGURE 5.16: Influence of different beta cuts

sources are calculated by comparing the values of the test statistic in the signal and background case with the values of the test statistic in the background only case. Afterwards the sensitivity for the stacked search is calculated in the same way. In Appendix A are the sensitivity plots in the order of the source ranking together with the optimization for an E^{-1} spectrum.
In this section, one example is shown. Figure 5.17 makes clear that there is indeed a remarkable gain in sensitivity when the lightcurve is included in the likelihood. The blue curve shows the result of a purely angle based reconstruction as used in the previous point source searches. The green curve reveals the benefit of the additional use of the ANN estimator for energy reconstruction. The largest gain, however is obtained via the lightcurve.

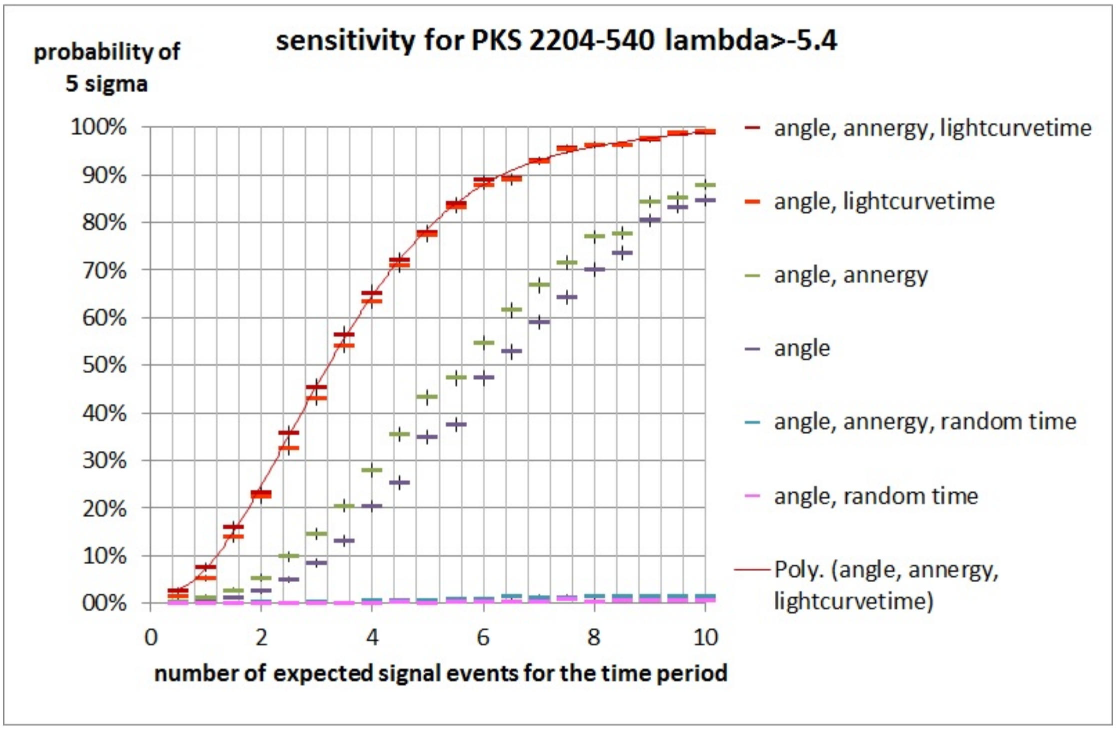

FIGURE 5.17: Optimized sensitivity for PKS 2204-540
In the lowest graph random times are chosen instead of times from the cumulative lightcurve and the likelihood function of the lightcurve is applied. In the graph at the very top likelihood functions of angle, reconstructed energy and time from the lightcurve are combined.

TABLE 5.3: Optimization for PKS 2204-540

lambda cut	number of events from source Monte Carlo	50% probability for 5 sigma at	quotient
-5.5	$9.80 \cdot 10^{13}$	3.45	$2.8 \cdot 10^{13}$
-5.4	$9.52 \cdot 10^{13}$	3.25	$2.9 \cdot 10^{13}$
-5.3	$8.89 \cdot 10^{13}$	3.20	$2.8 \cdot 10^{13}$

Chapter 6

Selection of sources

The physical goal is to find out more about the possible hadronic accelerators AGN. This can be achieved best by a multimessenger approach. Tracking Active Galactic Nuclei with Austral Milliarcsecond Interferometry (TANAMI) is a program to image and monitor the parsec-scale structures of relativistic jets in AGN of the Southern Hemisphere with the Australian/ South African Long Baseline Array (LBA) of -30 degrees declination with milliarcsecond resolution at 8.4GHz and 22GHz. Currently, TANAMI is monitoring about 80 jets (most of them blazars) including many sources found by Fermi to be flaring at gamma rays [Kr12]. The TANAMI sample is highly visible to ANTARES. The selection of sources from the

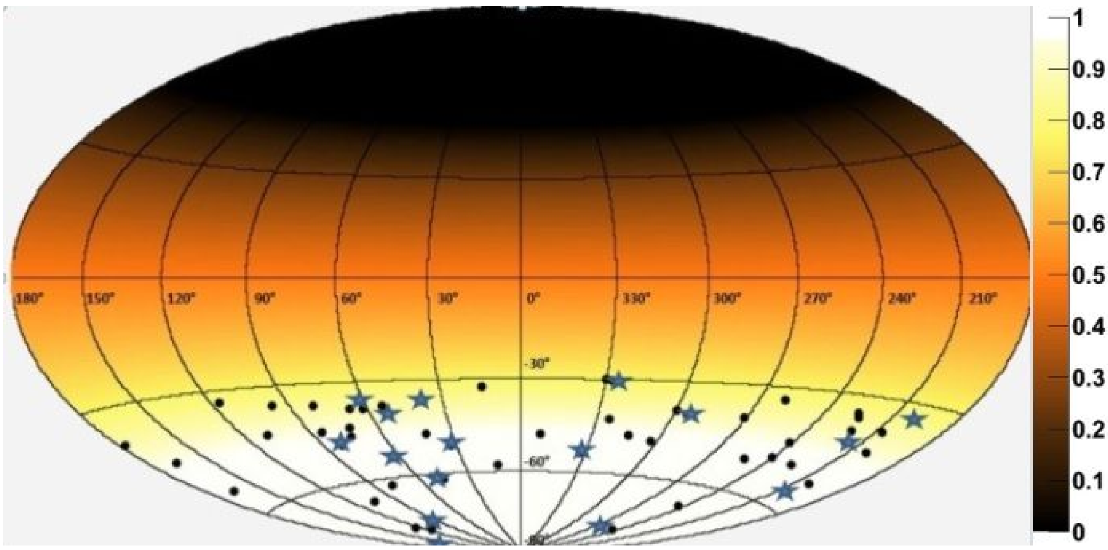

FIGURE 6.1: TANAMI sources and visibility of ANTARES
black dots: sources observed by TANAMI
blue stars: selected sources
color scale: visibility of ANTARES

sample is done according to the sensitivity criterion. Roughly estimated leads a doubling of the number of photons to four times as many interactions and hence four times as many neutrinos. The conclusion is to choose brighter sources as first point. As it is shown in Chapter 5, the strength of the method consists in reducing background. The normalized height of the lightcurve is used as part of the probability density term. Therefore the larger the height at one time interval in comparison to the remaining time intervals, the larger the gain in sensitivity. This results in the weighting factor.

- Calculate the ratio $\frac{F_{\max}}{\text{FGLmeanflux}}$ and select only sources $\frac{F_{\max}}{\text{FGLmeanflux}} > 5$
- Count the number n of bins flux $>$ FGLmeanflux $+ 3\sigma$
  $\rightarrow w = \frac{1}{n}$

$\Rightarrow$ ranking factor $w \cdot \frac{F_{\max}}{\text{FGLmeanflux}}$

Figure 6.2 depicts the behavior of the ranking factor. The first item yields 16

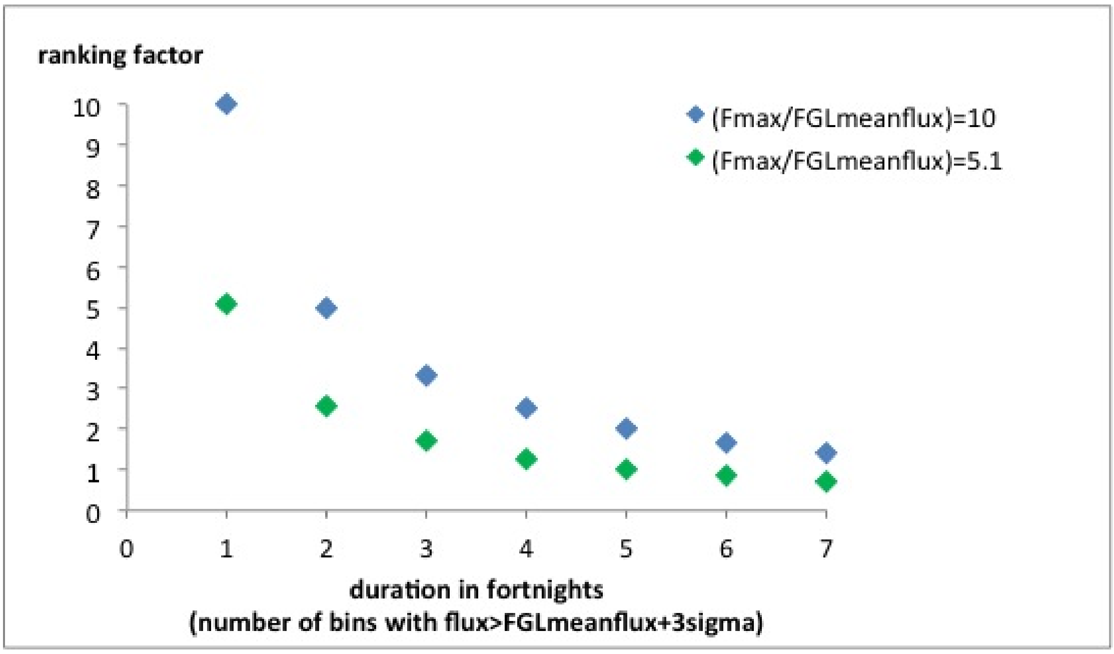

FIGURE 6.2: Ranking

sources (see Table 6.1), whose ranking is shown in Figure 6.3. Sources with higher ranking factors provide better detection chances, because the number of events that have to be detected for a 50% chance of a 5 sigma discovery is smaller for them. The lightcurve of PKS 2204-540 in Figure 6.4 has got only one high peak and is with this method better detectable than PKS 1424-418 as shown in Figure 6.5.

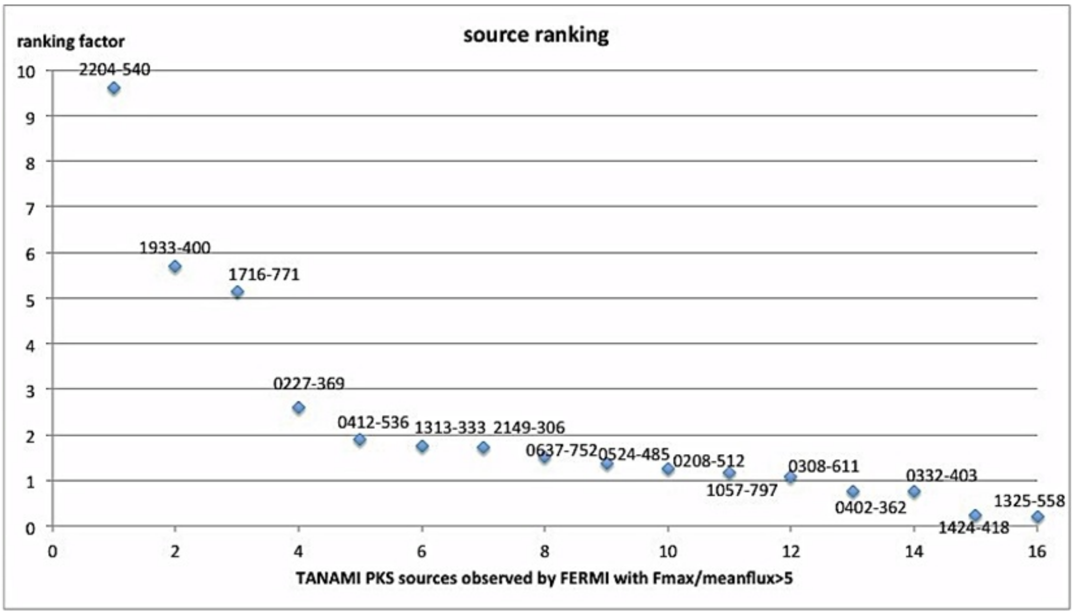

FIGURE 6.3: Ranking of the sources

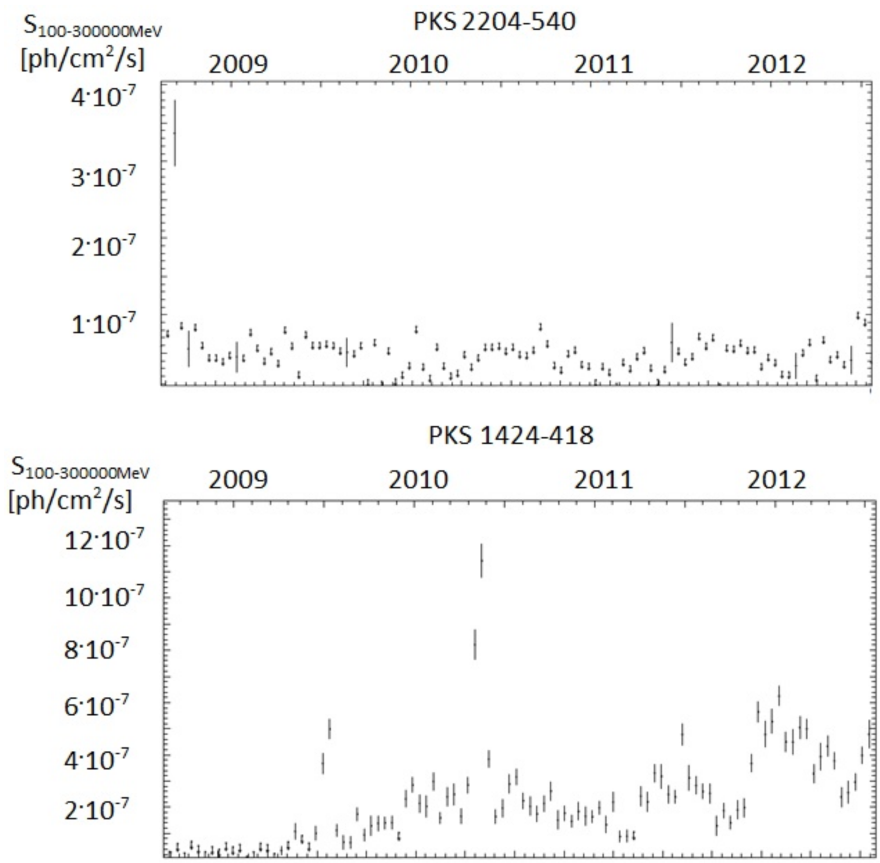

FIGURE 6.4: Comparison of lightcurves (lightcurves provided by Cornelia Müller): PKS 2204-540 is the source ranked best, PKS 1424-418 is the source ranked worst. Indeed the sensitivity for PKS 2204-540 is higher as shown in Figure 6.5 A vivid reason is that the peaks of the lightcurve of PKS 1424-418 are spread comparatively homogeneously, while the lightcurve of PKS 2204-540 has got only one high peak in 2008 that has got a great effect.

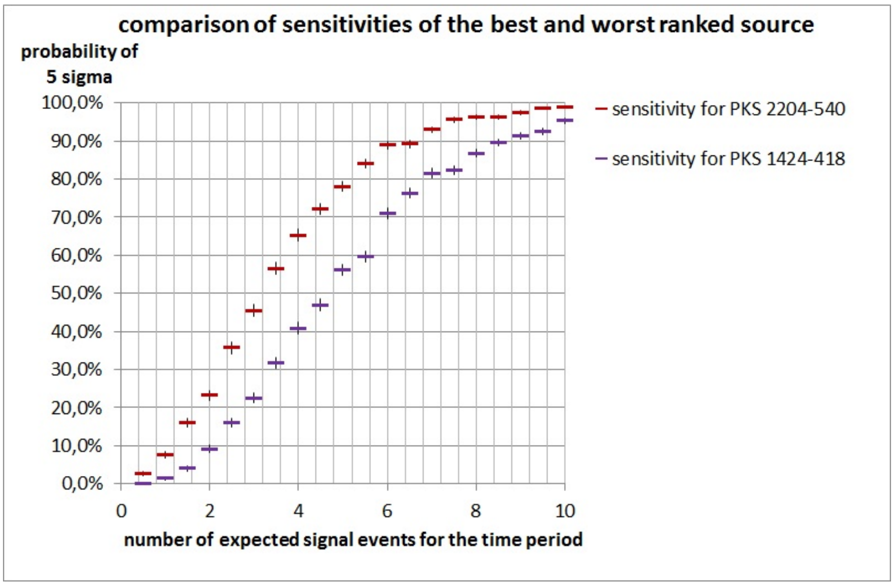

FIGURE 6.5: Comparison of sensitivities
Both sensitivities are displayed for the optimal lambda cut for the respective source, which is in both cases -5.4. The depicted effect shows that the influence of the shape of the lightcurve for the calculated sensitivity is well understood and implemented in the ranking factor.

lambda	source	type	RA (J2000)	Dec (J2000)	redshift
5.4	PKS 2204-540	Q	331.93208	-53.77611	1.206
5.6	PKS 1933-400	Q	294.3175	-39.96722	0.965
5.5	PKS 1716-771	U	260.96042	-77.23056	
5.6	PKS 0227-369	Q	37.3685375	-36.7324503	
5.4	PKS 0412-536	U	63.32167	-53.53389	
5.6	PKS 1313-333	Q	199.03333	-33.64972	1.21
5.5	PKS 2149-306	Q	327.98125	-30.465	2.345
5.1	PKS 0637-752	Q	98.94375	-75.27139	0.653
5.4	PKS 0524-458	U	81.5694633	-48.5102197	
5.4	PKS 0208-512	B	63.6925	-51.01722	0.999
5.3	PKS 1057-797	B	164.6804571	-80.0650442	
5.4	PKS 0308-611	Q	47.4837467	-60.0775153	1.48
5.4	PKS 0402-362	Q	60.9739579	-36.0838644	1.417
5.4	PKS 0332-403	Q	53.55667	-40.14028	1.447
5.4	PKS 1325-558	U	202.2547704	-56.11340739	
5.5	PKS 1424-418	Q	216.98458	-42.10528	1.522

TABLE 6.1: Table of selected sources (Q=quasar, B=blazar, U=unidentified)

Chapter 7

Source stacking

7.1 Sensitivity of the stacked search

To enhance sensitivity in case of similarly behaving sources, it was decided to perform a stacked search. The maximization of the likelihood

$$L(n_s) = \prod_{i=1}^{N} \left[\frac{n_s}{N} S_i + \left(1 - \frac{n_s}{N}\right) B_i \right] \tag{7.1}$$

contains factors S_i and B_i in the appropriate number of all sources. So in each run of the program for all sources one common value of the test statistic is calculated.

The number of signals is expected to increase linearly with the number of sources and the fluctuation of background events with the square root of the number of sources. As in multiple tests not the standard deviations are added, but the variances, it is

$$\mathrm{Var}_{total} = \mathrm{Var}_1 + \mathrm{Var}_2 + ... + \mathrm{Var}_{16} = \sigma_1^2 + \sigma_2^2 + ... + \sigma_{16}^2$$

$$\Rightarrow \sigma_{total} = \sqrt{\sigma_1^2 + \sigma_2^2 + ... + \sigma_{16}^2}$$

So if background is considered as standard deviation from the signal, the following approximation leads to the introductory sentence:

$$b_{total} \approx \sqrt{16 \cdot b_1^2} = \sqrt{16} \cdot b_1$$

Thus, when N is the number of sources in the stacked search and n is the number of events needed for a 50% chance of a 5σ discovery for a single source, the number of events needed for a 50% chance of a 5σ discovery in a stacked search per source is

$$n_{stacked} = \frac{n \cdot \frac{N}{\sqrt{N}}}{N} = \frac{n}{\sqrt{N}}$$

In our case, the mean number of events needed for a 50% chance of a 5σ discovery is for the sources, which are optimized to the different lambda cuts $n = 4.30625$. The number of sources considered in the stacked search is $N = 16$. This would lead to an expectation of $n_{stacked} = 1.0766$ for events needed for the 50% chance of a 5σ discovery in the stacked search.
In the edge case of no background events, if n signal events are needed for a 50% chance of a 5σ discovery, per source the number of needed events in a stacking of N sources is

$$n_{stacked} = \frac{n}{N}$$

So in the actual case, where the number of background events is small, the number $n_{stacked}$ should lie between the mentioned quantities. The result shown in 7.4 agrees in fact with this assumption: The number of events needed for a 50% chance of a 5σ discovery in the stacked search of 16 sources is $n_{stacked} = 0.66$. In the stacked search in [Ab11] for 16 sources the ratio of the actual number to the number calculated by $\frac{n}{\sqrt{N}}$ is $\frac{0.3}{0.5}$, which is in perfect conformity with the ratio $\frac{0.66}{1.08}$ found here. Apposite to the distribution of the test statistic for one source displayed in Figure 7.2 is the distribution of the test statistic of the stacked search displayed in Figure 7.3. The factor mentioned above has to be considered.

For the plot 7.3 of the test statistic of the stacked search one event from each source was assumed.
In the analysis shown in the plots 7.3 and 7.4 the number of signal events follows a poissonian distribution.

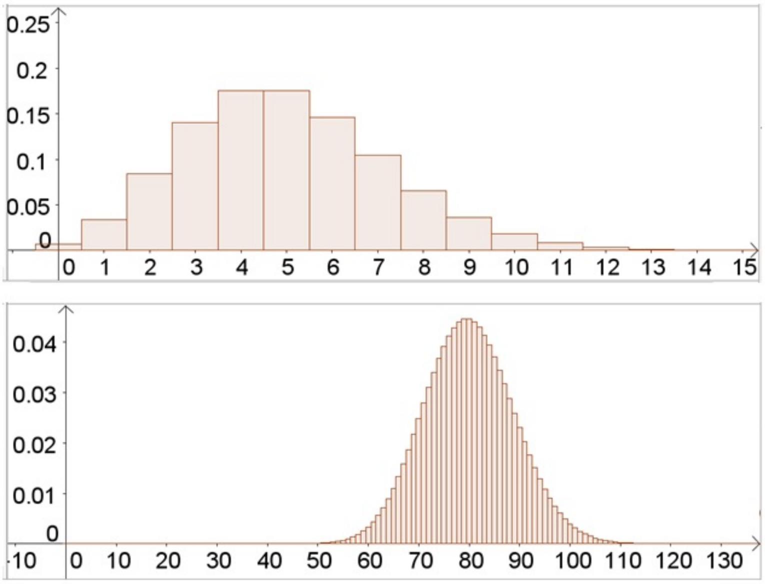

FIGURE 7.1: Trend for the shape of the poissonian distribution

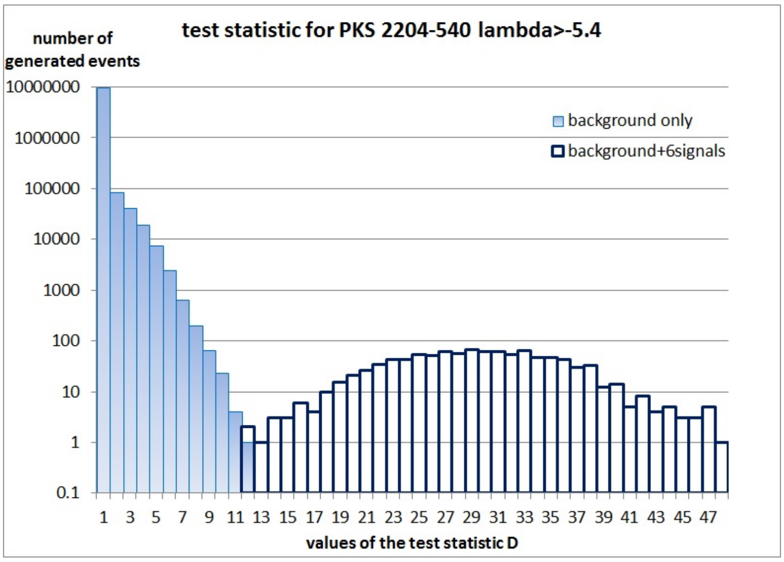

FIGURE 7.2: Test statistic distributions for one source

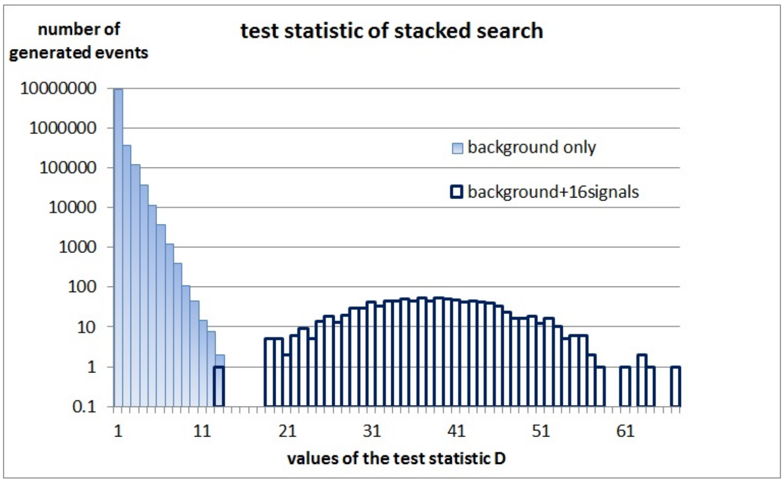

FIGURE 7.3: Distribution of the values of the test statistic for the stacked search

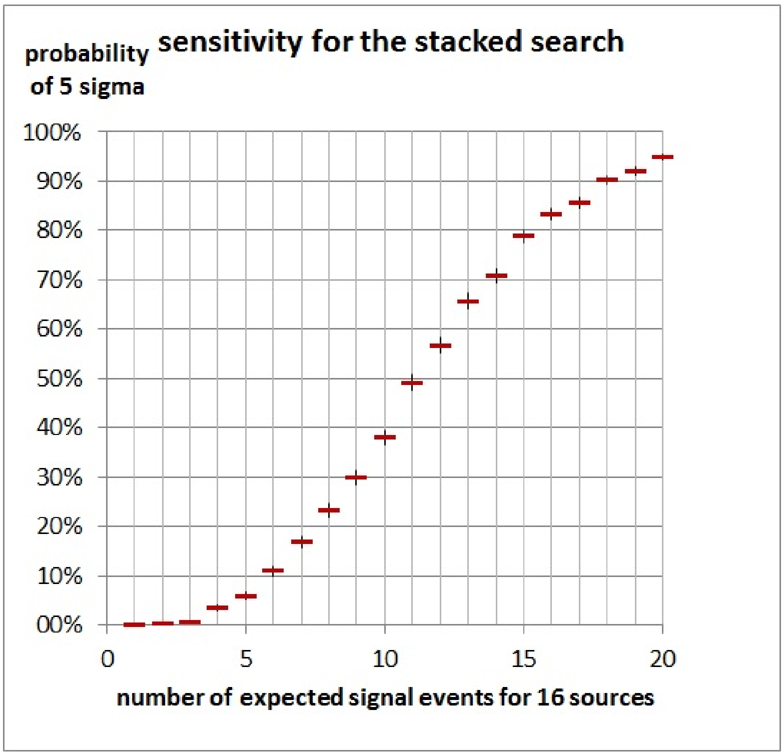

FIGURE 7.4: Probability of discovery for the stacked search

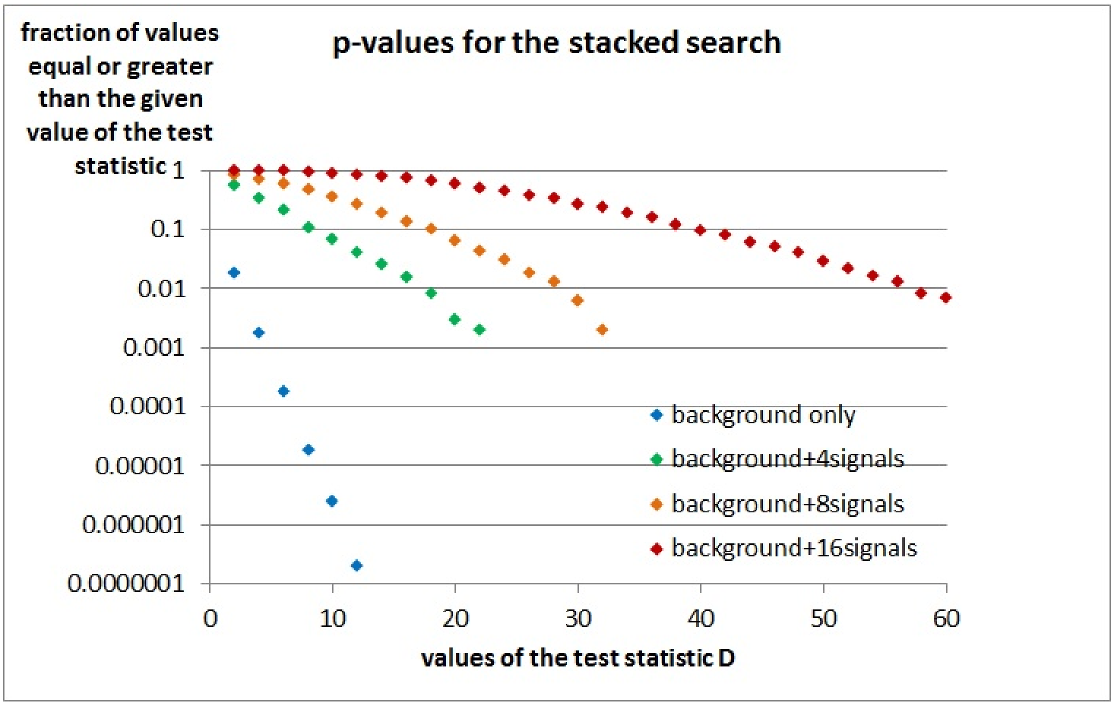

FIGURE 7.5: P-values

7.2 Uncertainty analysis

The three parameters angle, energy and time used in the analysis 5 contain uncertainties. As the time resolution of the ANTARES detector is in the order of $1ns$ and the considered time intervals are fortnights, in this analysis the error in time does not play a role.
The uncertainty in energy is taken into account via the described shift in energy by up to 15% (see 5.3).
Overview of systematics (table!).
While the median of the cumulative distribution of the angle between the direction of the reconstructed muon and that of the true neutrino is 0.38 deg (see [Ad14]), this uncertainty is already taken into account in the analysis 5.1, as reconstructed angles are used. The absolute orientation of the detector is known with an accuracy of 0.1 deg ([Ad12]). The influence of the latter effect is investigated.

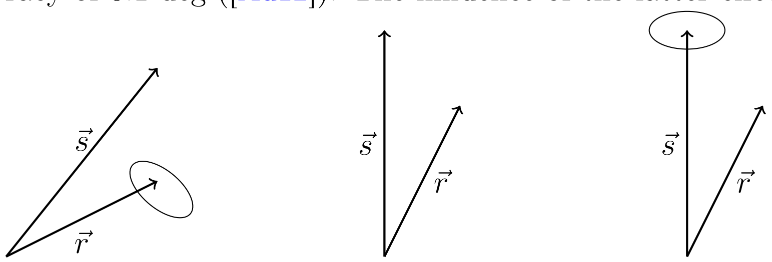

In the pictures $\vec{s}$ is the vector to the source and $\vec{r}$ is the reconstructed direction. The picture on the left shows the fact that the reconstructed direction has to be smeared by up to 0.1 deg due to the uncertain orientation of the detector. The following pictures show how this problem is solved. The vectors are rotated around an axis perpendicular to both until the vector to the source is parallel to the z-axis of the coordinate system. Thereby the angle between the vectors is preserved. Instead of smearing the reconstructed direction, now the vector to the source is smeared, which has got the same effect. This procedure offers two advantages: The rotation matrix has to be calculated only once per source and the smearing can be performed easily. First, the angle is chosen from a sin-distribution between 0 deg and 0.1 deg, as there is only one point in the middle of the circle and the number of points increases according to sine when approaching the edge. Secondly, the zenith of the rotated source vector is increased by the chosen angle. Thirdly, for the azimuth of the rotated source vector, a random value is chosen. This ensures a random smearing of up to 0.1 deg. Afterwards, the new angle between the reconstructed direction and the source direction is calculated (calculation see

Appendix C).

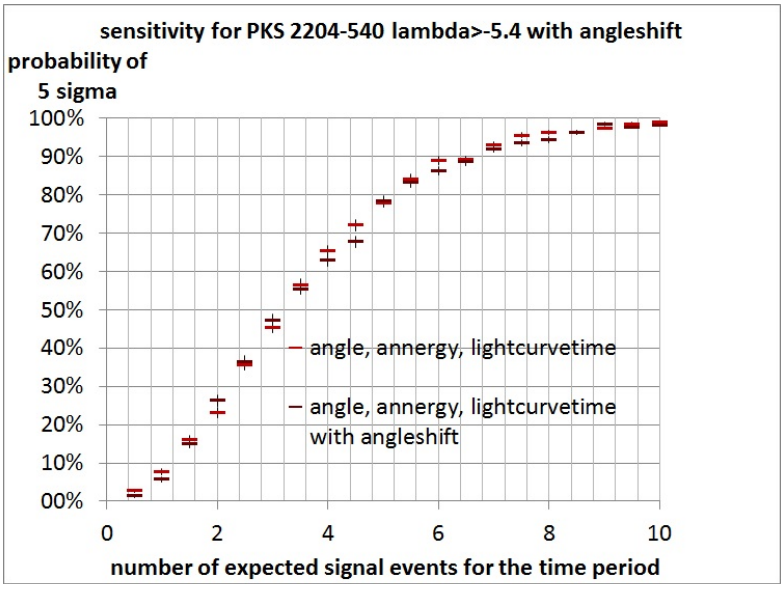

FIGURE 7.6: Sensitivity for shifted angles

7.3 Calculation of limits

There are two main approaches regarding confidence level. The Bayesian approach claims the confidence level to be the the rate of reliance that the true value is within the calculated confidence interval. The Frequentist approach asserts that when many confidence intervals with confidence level α are calculated, α is the fraction of confidence intervals containing the true value. This work follows the frequentist approach that was developed by Neyman and specified by Feldman and Cousins.

The aim is to be able to set limits on the flux based on a value of the test statistic from measured data. This is achieved as follows. For each Poissonian expectation for the number of signals an interval is built which contains the corresponding value of the test statistic from measured data with 90% probability. Hence the value is in 90% of intervals. The choice of arbitrary intervals with 90% confidence level might lead to two problems, though: Nonphysical values i. e. values of the test statistic smaller than 0 and the so called problem of flip-flopping and underestimation at the transition from two sided limits to an upper limit. Both problems are overcome choosing special 90% confidence intervals following the method of Feldman and Cousins [FC98]. Existing tables are only for discrete values, while in the analysis there are no restrictions for the values of the test statistic or the Poissonian expectation for the number of signals other than that they are positive real numbers. Therefore the calculation of the limits is done using 10000 simulations for each Poissonian expectation for the number of signals. The relative frequency of the values of the test statistic for each Poissonian expectation for the number of signals is taken as approximation for the probability. In the next step the probabilities are ranked: For a fixed value of the test statistic the Poissonian expectation with the highest probability is found. The probabilities for all Poissonian expectations for the same value of the test statistic are divided by the highest probability. This gives the ranking, according to which values of the test statistic for each Poissonian expectation for the number of signals are chosen, until the 90% level is reached.

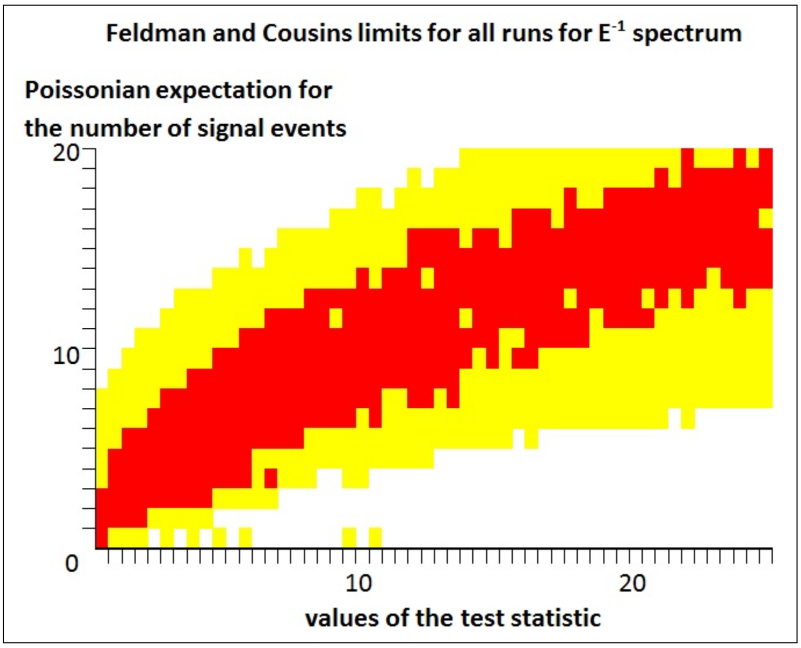

FIGURE 7.7: Upper limits according to the method of Feldman and Cousins for all runs of the data production between 01.09.2008 and 30.07.2012 assuming an E^{-1} spectrum (red: 50% CL, orange: 90% CL)

To convert the number of signals into a flux, the acceptance in Table 7.1 is calculated as described in Section 4.2.

Table 7.1: Acceptance for the stacked search

source	lambda cut	acceptance for E^{-1}	acceptance for E^{-2}
PKS 2204-540	-5.4	$191 \cdot 10^3$	11.4
PKS 1933-400	-5.6	$209 \cdot 10^3$	12.0
PKS 1716-771	-5.5	$198 \cdot 10^3$	14.1
PKS 0227-369	-5.6	$201 \cdot 10^3$	11.5
PKS 0412-536	-5.4	$191 \cdot 10^3$	11.4
PKS 1313-333	-5.6	$193 \cdot 10^3$	10.9
PKS 2149-306	-5.5	$183 \cdot 10^3$	10.0
PKS 0637-752	-5.1	$148 \cdot 10^3$	9.08
PKS 0524-485	-5.4	$205 \cdot 10^3$	10.7
PKS 0208-512	-5.4	$183 \cdot 10^3$	11.9
PKS 1057-797	-5.3	$179 \cdot 10^3$	12.1
PKS 0308-611	-5.4	$191 \cdot 10^3$	11.4
PKS 0402-362	-5.4	$184 \cdot 10^3$	10.3
PKS 0332-403	-5.4	$190 \cdot 10^3$	10.5
PKS 1325-558	-5.4	$191 \cdot 10^3$	11.4
PKS 1424-418	-5.4	$190 \cdot 10^3$	10.5
total		$303 \cdot 10^4$	179

Chapter 8

Results and discussion

For every event from data the angular distance to every selected source is calculated. Thus the event is assigned to a source. Furthermore, the reconstructed energy from ANN estimator is stored. Via the timing information every event is placed in one of the 102 fortnights of the considered time interval starting with 01.09.2008.

For all 16 sources the angle information and the energy information from the Monte Carlo production are loaded as well as the lightcurves. From this the histograms of signal and background for angle, energy and time are built as described in Chapter 5.

So S and B are vectors of 16 vectors that consist for each source of the heights of the normalized histograms for the measured data for signal and background. As described in Chapter 7 on the stacked search, all values S_i and B_i from all the sources give one product, which is optimized in n_s. Therefrom one test statistic value D is calculated.

For the 0 ending runs all processes described in Chapter 5 to Chapter 7 are redone. As expected the number of background events from the 0 ending runs is about 10% from the number of background events from all runs (see Figure 8.1). The second largest of 10 million values in the background only distribution of the 0 ending runs in Figure 8.2 of the test statistic values in the stacked search is 11.8. The value of the test statistic from the 0 ending runs without allowing energy shift is 0.49. According to Figure 8.3 the upper limit for the Poissonian expectation for the number of signals is 6 for 90% confidence level. This number can be translated into a flux via the acceptance 7.1. From a flux normalization of $16 \cdot 10^{-7}$ for an E^{-2} spectrum for 10% of the runs 17.9 events (see Table 7.1) are

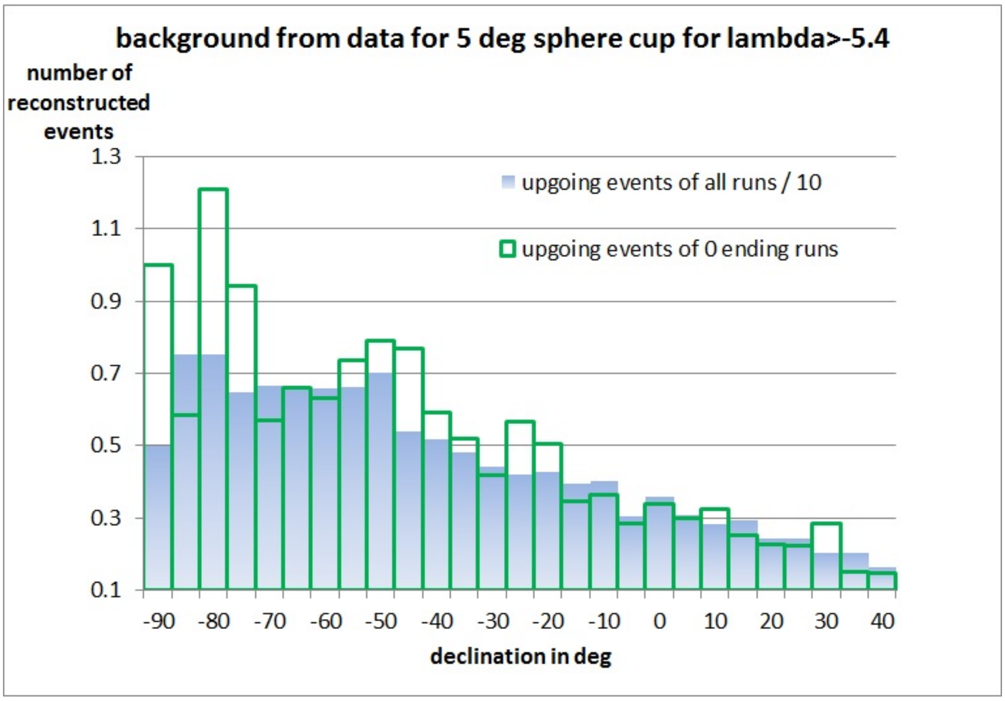

FIGURE 8.1: Comparison of the background of the 0 ending runs and of all runs

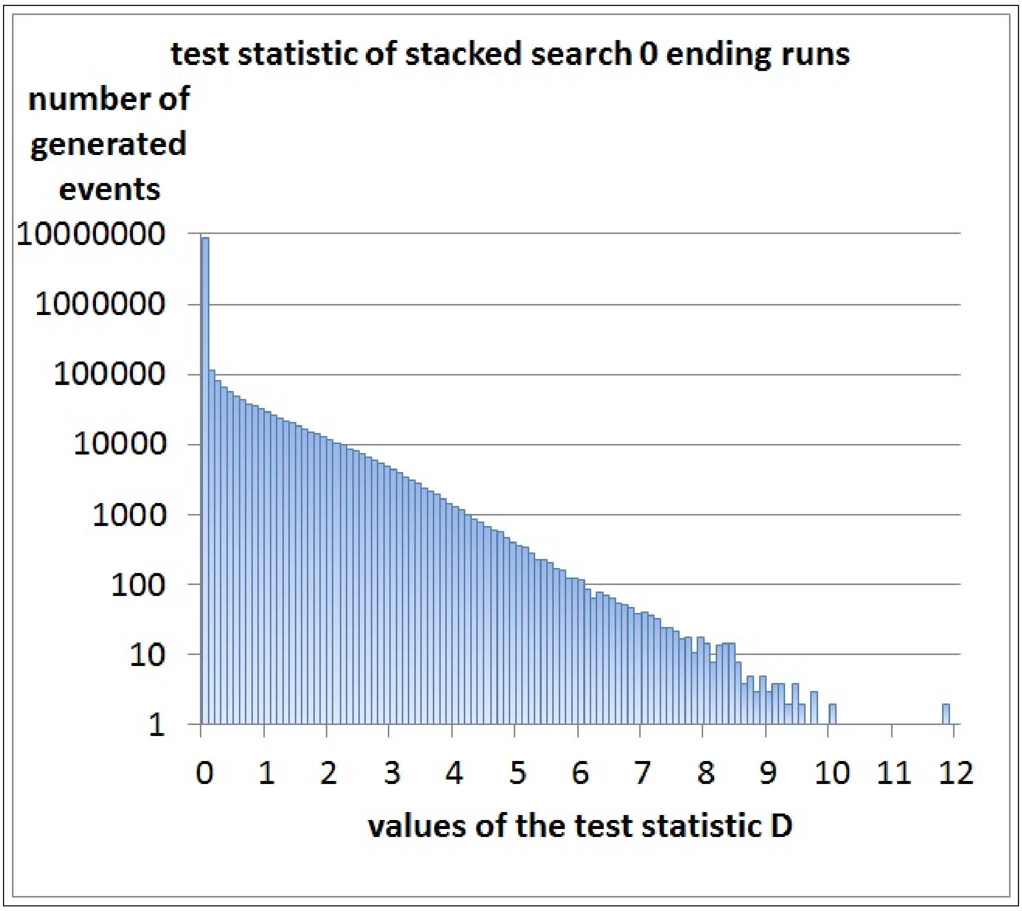

FIGURE 8.2: Test statistic for the background only case of the 0 ending runs

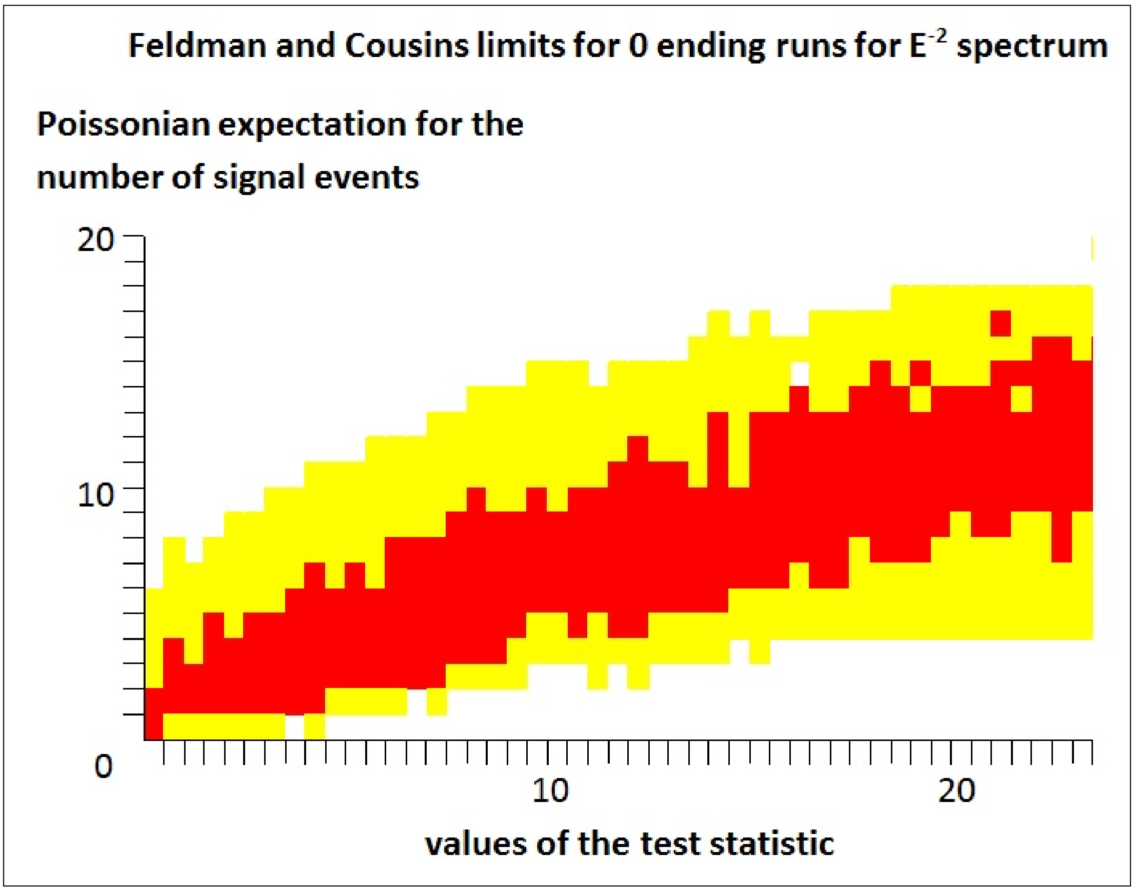

FIGURE 8.3: Upper limits according to the method of Feldman and Cousins for the 0 ending runs of the data production between 01.09.2008 and 30.07.2012 assuming and E^{-2} spectrum (red: 50%, orange: 90% CL)

being reconstructed. So the upper limit for the flux for an E^{-2} spectrum from the 16 sources is $54 \cdot 10^{-8}\ \frac{\text{GeV}}{\text{cm}^2 \cdot \text{s}}$, which gives a mean flux of $3.4 \cdot 10^{-8}\ \frac{\text{GeV}}{\text{cm}^2\text{s}}$.

In total 51 events from the 0 ending runs from the whole time period fulfilled the criterion to have a reconstructed angle to one of the 16 sources smaller than 5 degree. In the following the distributions of angles to the sources of the events (see Figure 8.4) are shown as well as the distributions of energies (see Figure 8.5) and the distribution of the events in comparison to the lightcurves (see Figure 8.6). 16 events (see Tabular 8.1) showed up coincident with a flare of the corresponding source.

QB is a flag that contains basic quality criteria for a run. QB = 3 means that the run fulfills the following criteria ([WA14]):

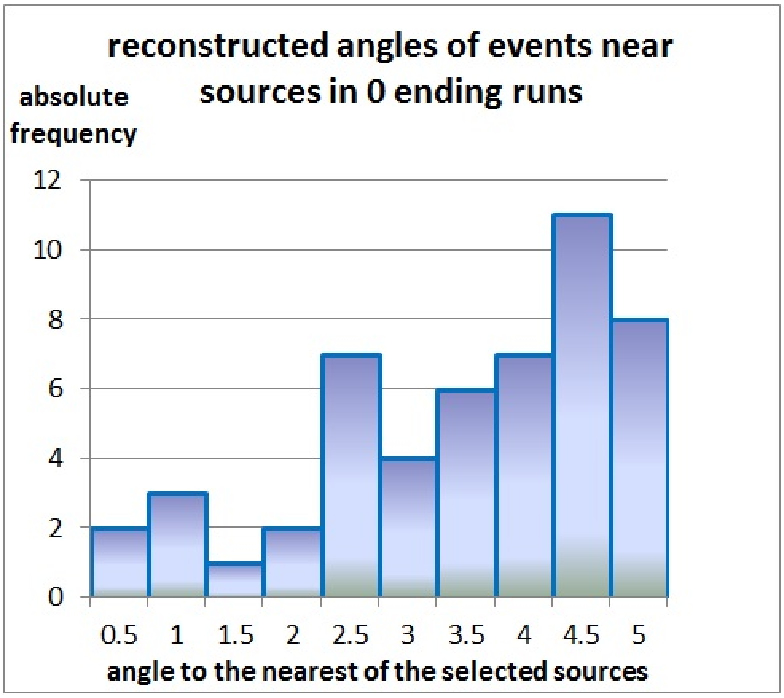

Figure 8.4: Angles of the events from the 0 ending runs each to the nearest of the 16 selected sources

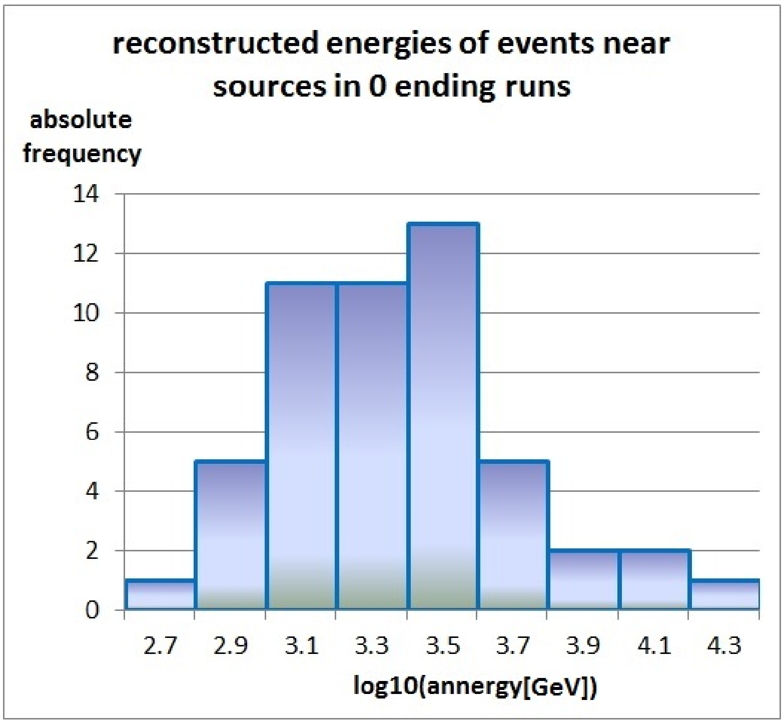

Figure 8.5: Reconstructed energies of the events from the 0 ending runs with angles smaller than 5 deg to one of the 16 selected sources

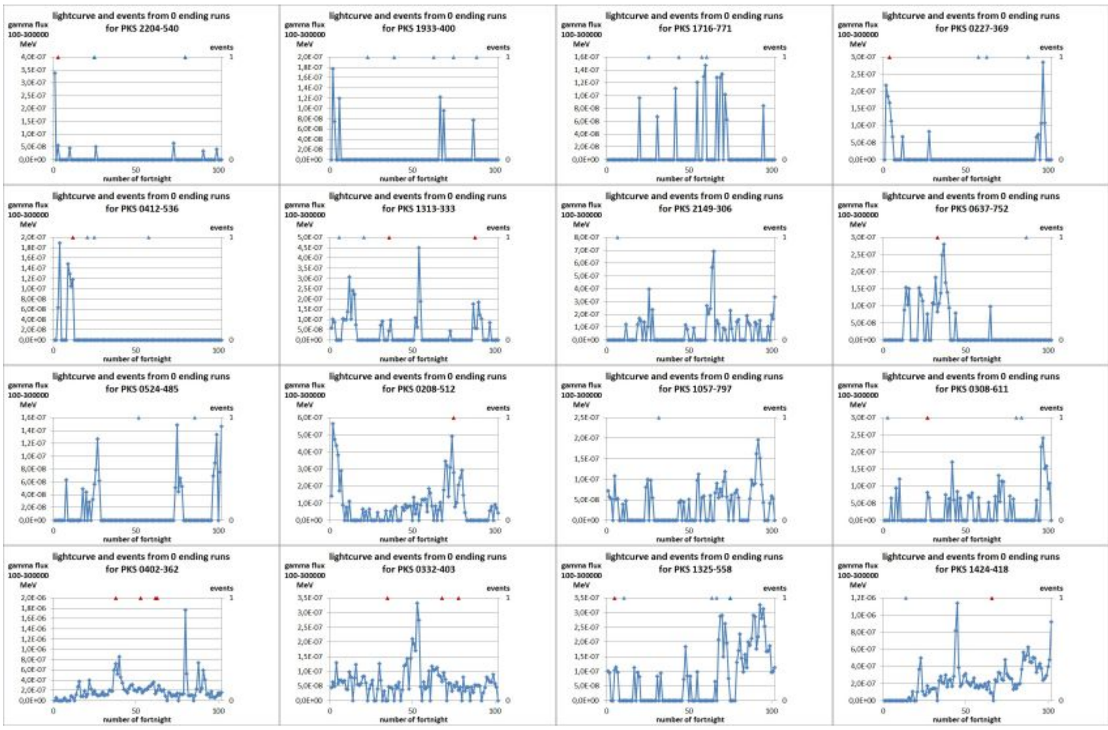

FIGURE 8.6: Lightcurves of the 16 selected sources and events from the 0 ending runs (larger images see Appendix D)

TABLE 8.1: Events from 0 ending runs with γflux>0
The sources are numbered as in the ranking,
the fortnights are numbered from 01.09.2008

source	angle [deg]	annergy [TeV]	fortnight	MJD	date	run	QB
1	3.90	2.06	3	54751.939	13.10.2008	36300	4
4	4.34	14.5	4	54761.851	22.10.2008	36570	3
15	4.28	2.93	5	54774.9753	04.11.2008	36860	3
5	4.82	1.19	12	54870.5847	08.02.2009	38990	4
12	3.65	0.36	27	55074.917	31.08.2009	42860	4
8	3.31	3.57	33	55166.7096	01.12.2009	44860	3
6	3.84	1.20	36	55213.0395	17.01.2010	45860	4
13	4.55	5.91	38	55232.1058	05.02.2010	46360	3
13	0.75	6.32	53	55447.4709	08.09.2010	51840	4
13	0.50	8.49	62	55565.1283	04.01.2011	54320	4
13	2.07	2.05	63	55580.5407	19.01.2011	54710	4
16	1.59	1.62	66	55627.7495	07.03.2011	55810	4
14	4.95	2.40	68	55662.3949	11.04.2011	56760	4
10	4.49	2.12	75	55756.0616	14.07.2011	58640	4
14	4.66	0.81	78	55792.1002	19.08.2011	59170	3
6	4.52	1.28	88	55941.6503	15.01.2012	62180	4

- at least one active analog ring sampler, i. e. chip of the photomultiplier read out system
- no synchronisation problems
- frametime in database matches the frametime in data
- no double frames
- sampling of timeslices < 3
- limited time lost during the run $0 \leq (T_{\mathrm{stop}} - T_{\mathrm{start}}) - (N_{\mathrm{slices}} \cdot \mathrm{frametime} \cdot \mathrm{sampling}) \leq 450$ s
- $10\ \mathrm{mHz} \leq 3N\mathrm{Triggerrate} \leq 10^5\ \mathrm{mHz}$
- $\frac{N_{\mathrm{activeOM}}}{N_{\mathrm{theoOM}}} \geq 80\%$
- baselinerate ≤ 120 kHz
- burst fraction $\leq 40\%$

For QB $= 4$ the burst fraction has to be less or equal than 20%.

Although the runs with the interesting events fulfill high levels of quality as shown in Table 8.1 and although many events are within 5 degrees from one of the selected TANAMI sources coincident with a peak in the Fermi lightcurve as shown in Figure 8.6, for the 0 ending runs only the detection is not significant. The present analysis is optimized for detection and assumes an E^{-1} spectrum. Nevertheless an upper limit for the stacked search for an E^{-2} spectrum can be set. This limit of $54 \cdot 10^{-8}\ \frac{\mathrm{Gev}}{\mathrm{cm}^2\mathrm{s}}$ holds for the flux from the whole sample of 16 TANAMI sources and represents a 90% confidence level. The upper limit for the mean flux per source of the 0 ending runs is classed with results of previous point source searches in Figure 8.7.

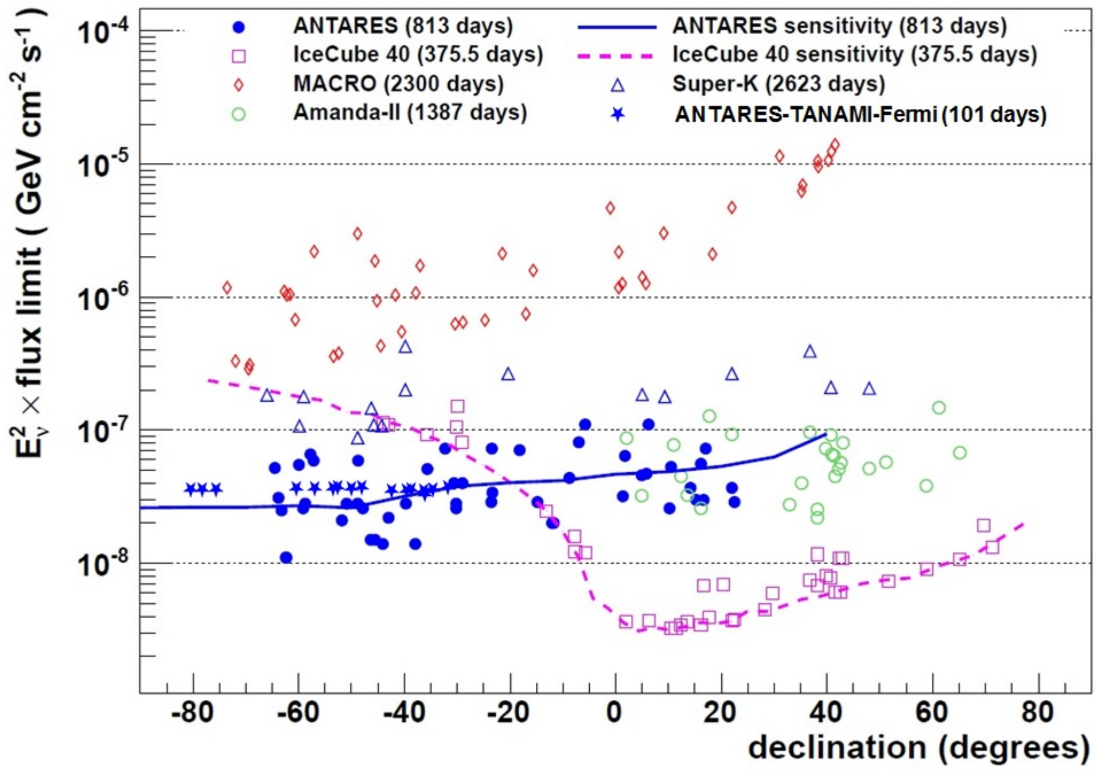

FIGURE 8.7: Mean upper limit per source set on an E^{-2} flux for the 16 stacked ANTARES-TANAMI-Fermi sources from 10% of the runs between 01.09.2008 and 30.07.2012. Upper limits, previously reported in [Ad12] by ANTARES and other neutrino experiments are also included.

Chapter 9

Summary and outlook

This work offers an overview of AGN, particle acceleration and neutrino production at AGN, the detection of neutrinos, the evaluation of the data, the simulation and the analysis. An appopriate sample of radio AGN observed by TANAMI is chosen. The search for neutrinos in correlation with gamma rays measured by Fermi enhances sensitivity remarkably.

Using upper limits, from the analyzed data conclusions concerning the AGN can be drawn. With 90% confidence level the neutrino flux from the examined 16 AGN for 10% of the data of ANTARES between 01.09.2008 and 30.07.2012 is below $3.4 \cdot 10^{-8} \frac{\text{GeV}}{\text{cm}^2\text{s}}$.

In the frame of the ANTARES telescope the analysis can be extended in three ways.

- Run by run conditions
  While the present analysis uses a self generated Monte Carlo, it is shown that the run by run Monte Carlo gives similar results. As a next step, the run by run Monte Carlo production can be investigated more comprehensively, the detector and environmental conditions within single runs can be surveyed.
- Reconstruction
  This analysis is based on the best track reconstruction algorithm available in terms of efficiency for the considered energy range and on a competitive

energy reconstruction method. Both, for track as well as for energy reconstruction, additional methods exist. So as a next step different reconstruction methods can be tested and combined. This could improve the angular resolution as well as the efficiency.

- Sources

  The search can be extended to a greater sample. Withal the stacked search works best for a homogeneous sample of sources.

  Within the stacked search, sources can be weighted.

  Sources brighter in gamma could be given a higher weight. As Fermi measures the flux of incoming gamma rays, also the distance to the source has to be considered in this case. There is the aspect of spread and the aspect of absorption. If the neutrino beam is highly collimated, almost no difference is to be expected in the neutrino flux between similar sources nearby and further away. If gamma rays are less collimated, the number of detected gamma rays decreases with the distance to the source. Besides the probability of absorption of gamma rays by the interstellar medium increases with distance. For these reasons alone the measured brightness in gamma rays of a source cannot serve as unique criterion for weighting. Nevertheless clearly of two identical sources at the same distance to the earth the source brighter in gamma will be expected to emit more neutrinos according to the majority of models. At the same time, not only the mean rate in the detected gamma flux has to be considered, but especially the relative height of the flares which might indicate coincident neutrino emission. The latter is used in this analysis as criterion for the selection of sources, but could for a larger sample also be used as weight for the single sources in the stacked search.

  Furthermore source models can be tested.

As the measured highly energetic protons in the cosmic ray spectrum must come from somewhere and as the sensitivity of this method is comparably high, there is justified hope that the unblinding of the full data set of ANTARES may finally reveal cosmic neutrinos.

Appendix A

Sensitivities for the 16 sources

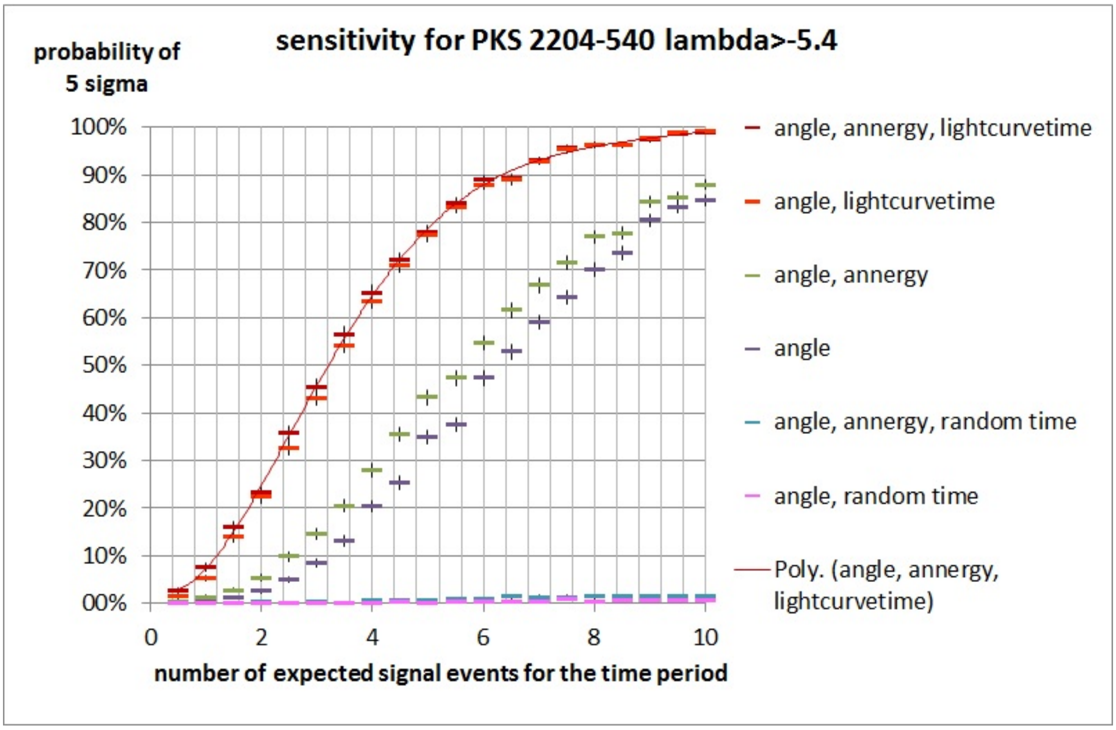

FIGURE A.1: Optimized sensitivity for PKS 2204-540

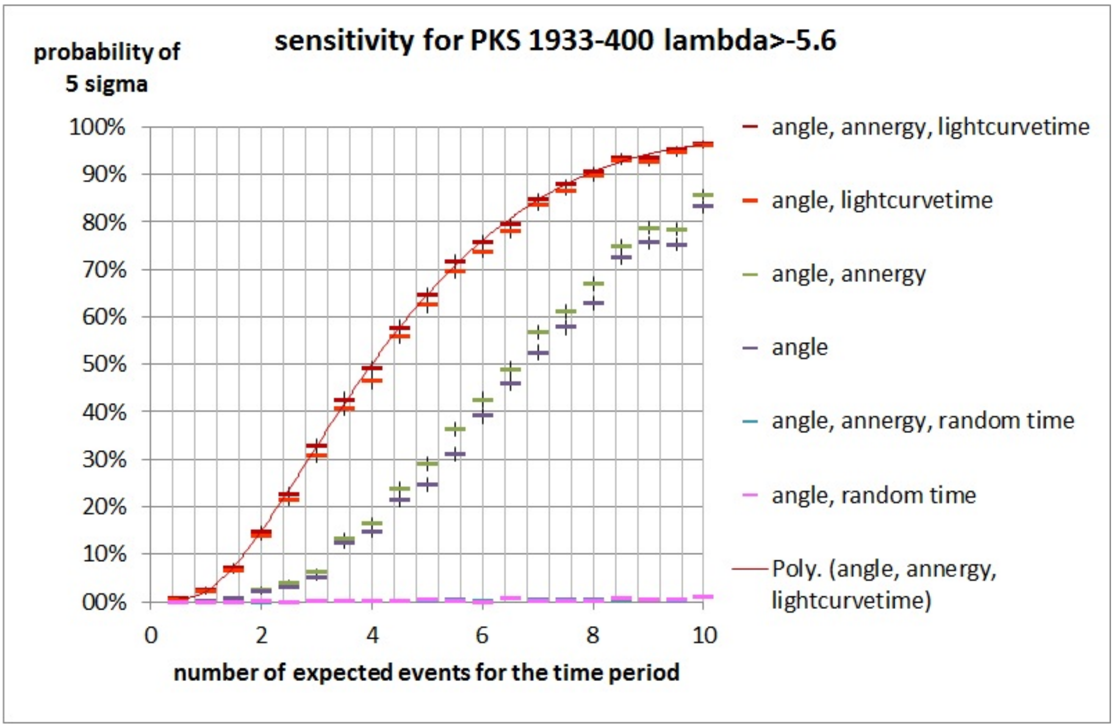

FIGURE A.2: Optimized sensitivity for PKS 1933-400

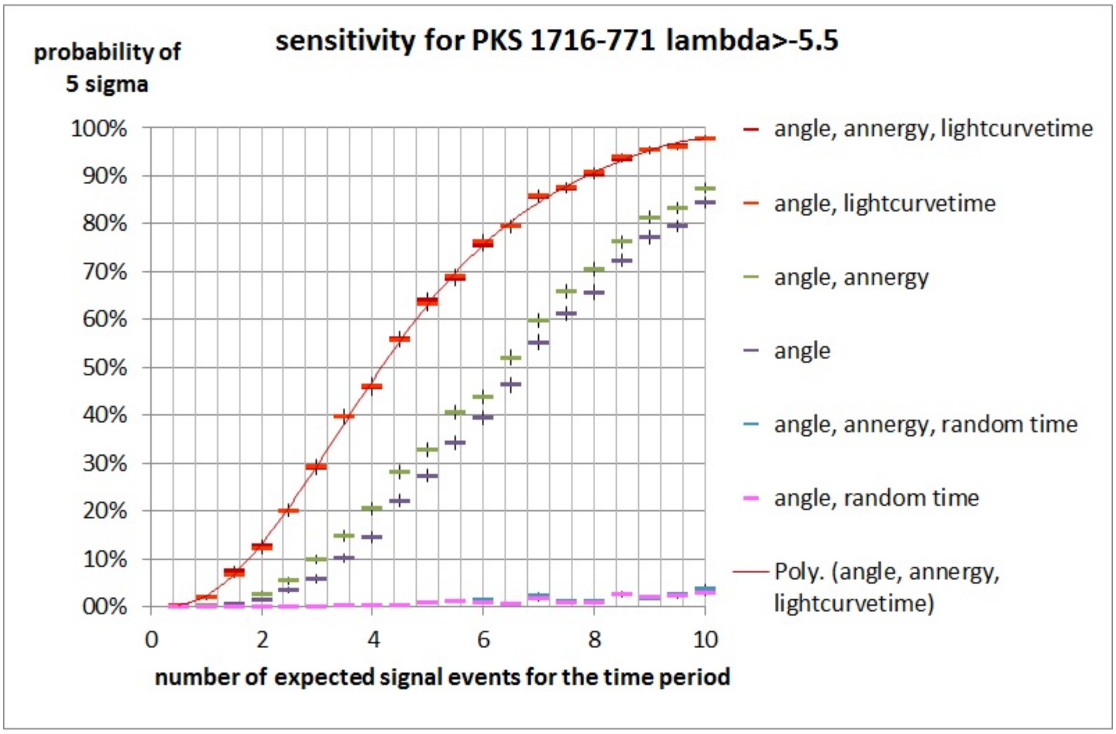

FIGURE A.3: Optimized sensitivity for PKS 1716-771

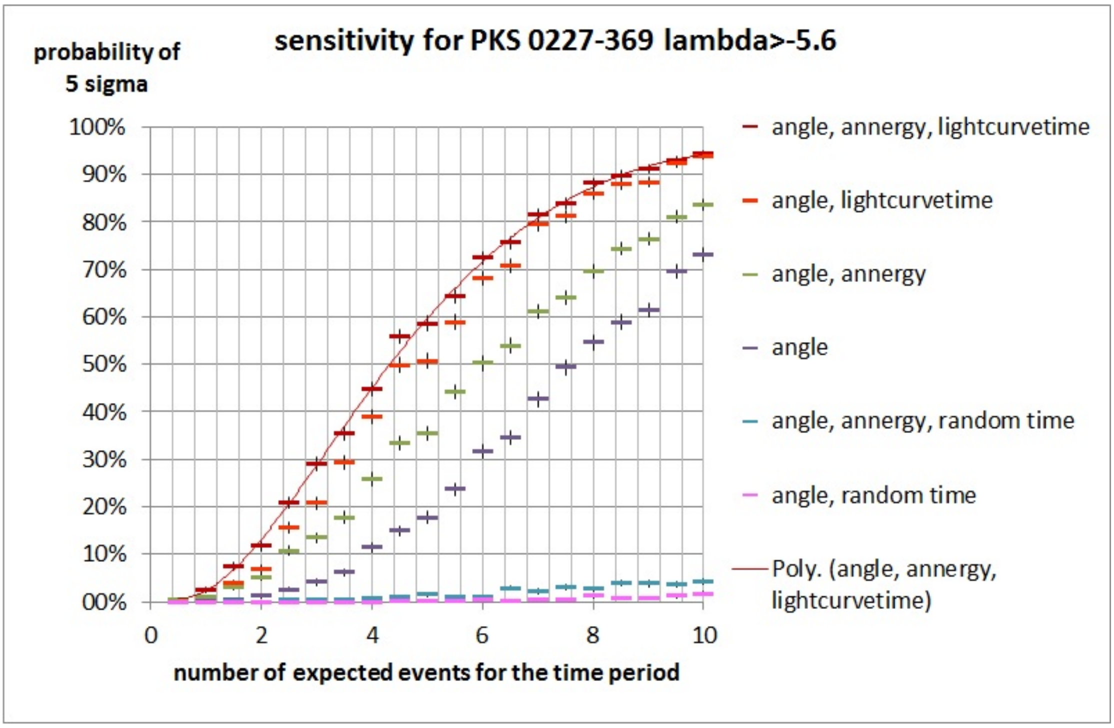

FIGURE A.4: optimized sensitivity for PKS 0227-369

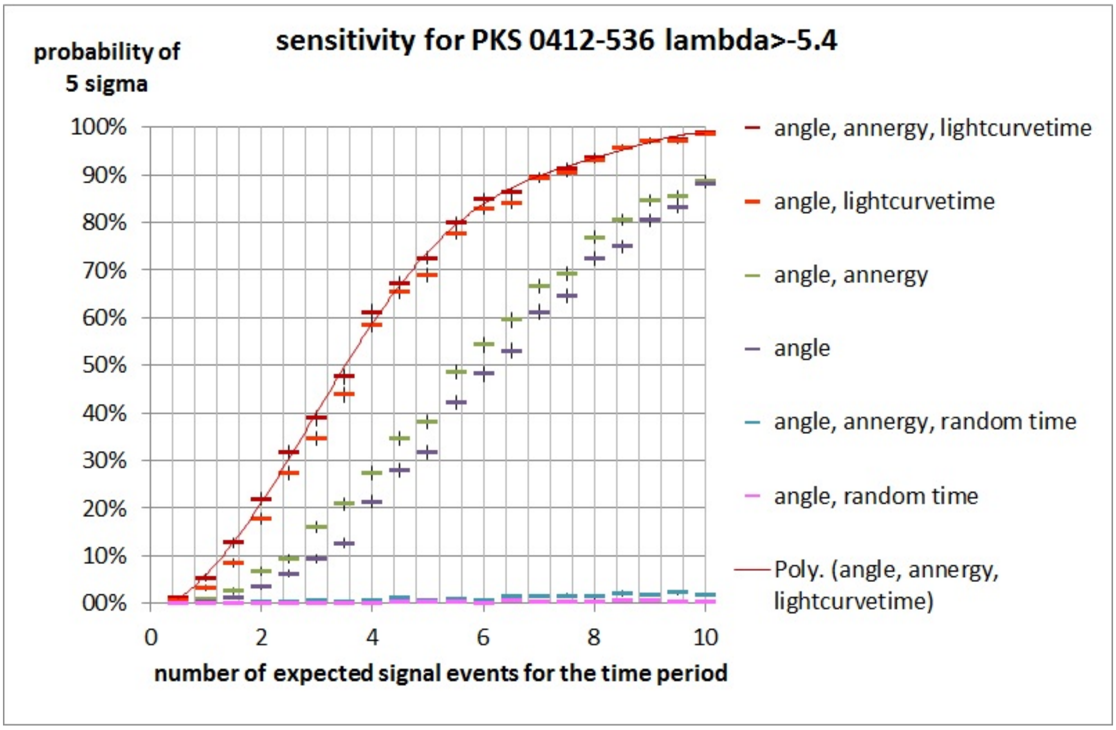

FIGURE A.5: Optimized sensitivity for PKS 0412-536

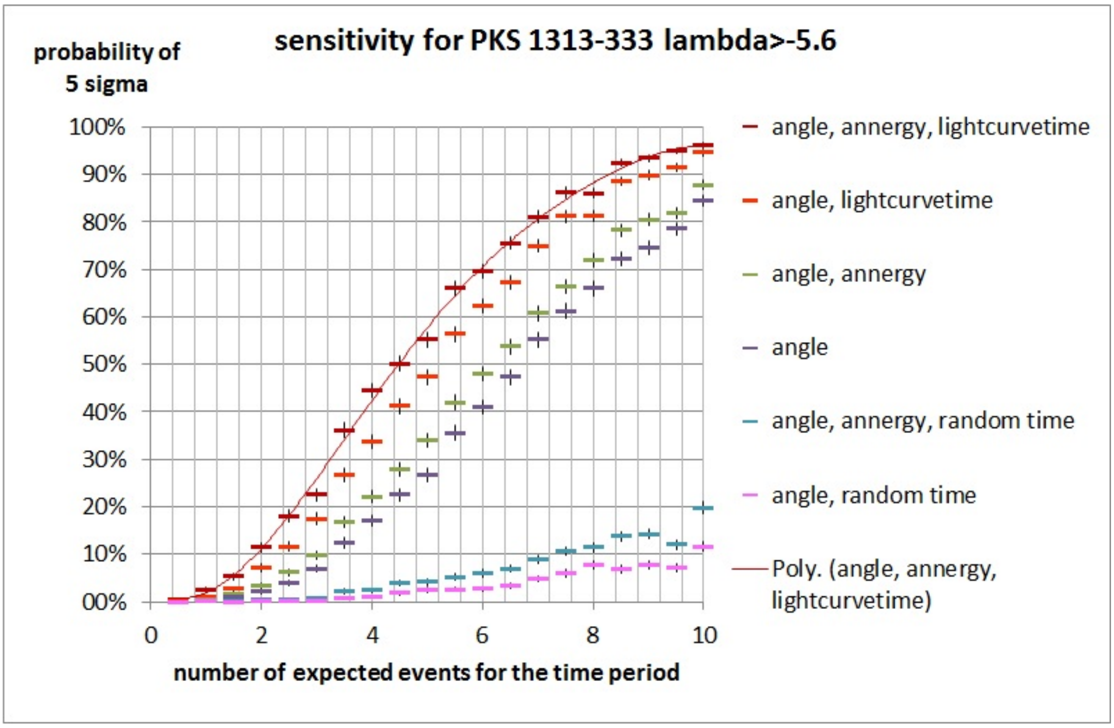

FIGURE A.6: Optimized sensitivity for PKS 1313-333

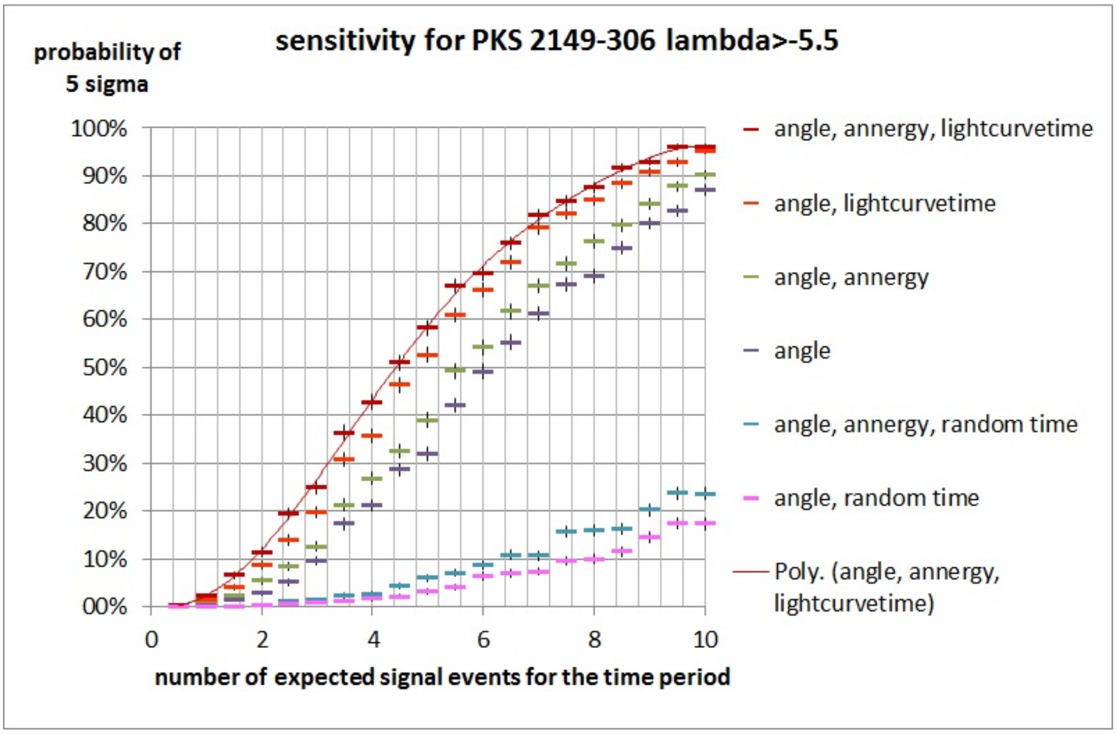

FIGURE A.7: Optimized sensitivity for PKS 2149-306

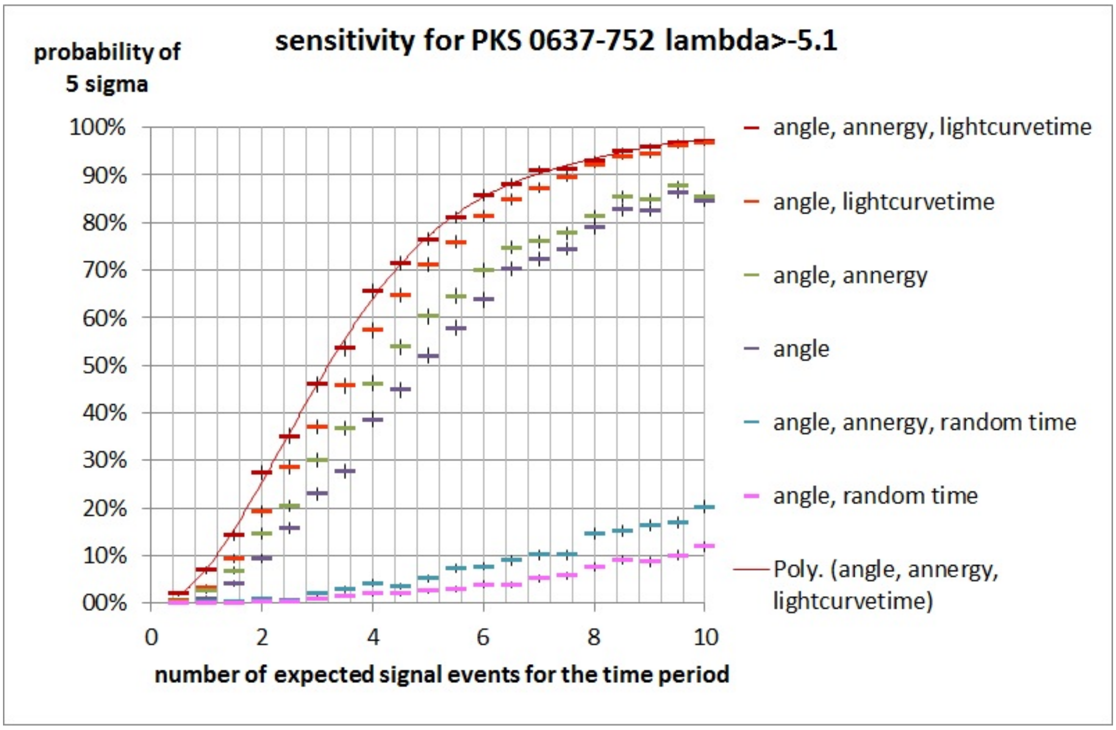

FIGURE A.8: Optimized sensitivity for PKS 0637-752

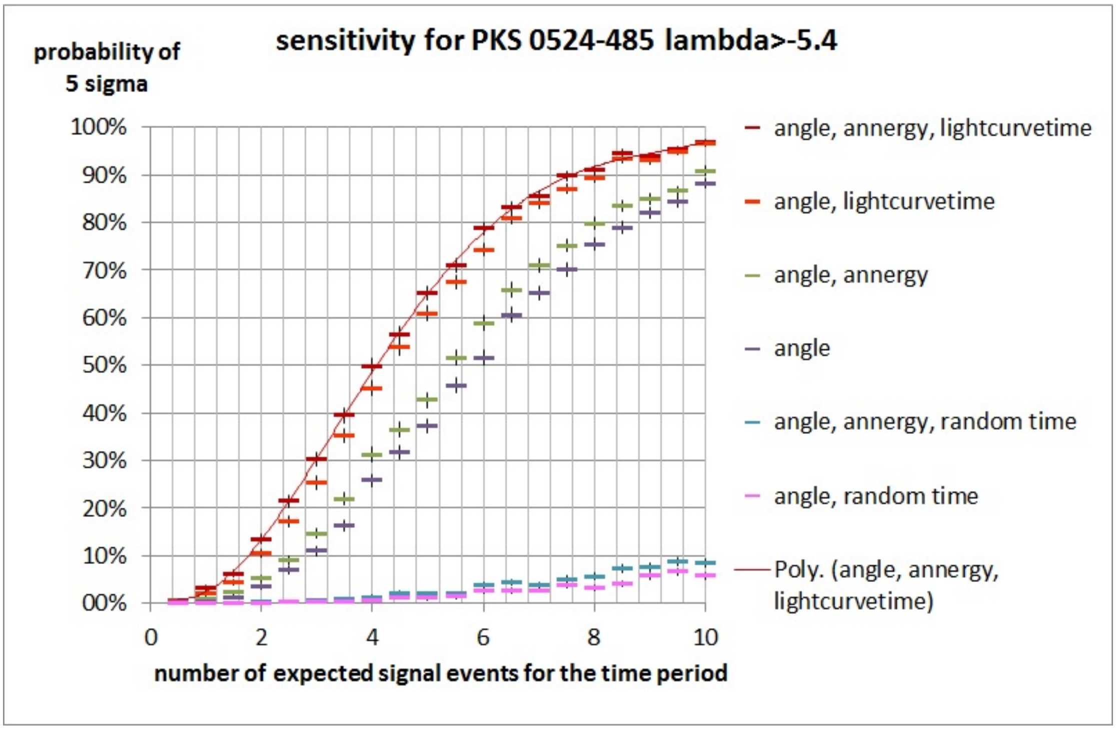

FIGURE A.9: Optimized sensitivity for PKS 0524-485

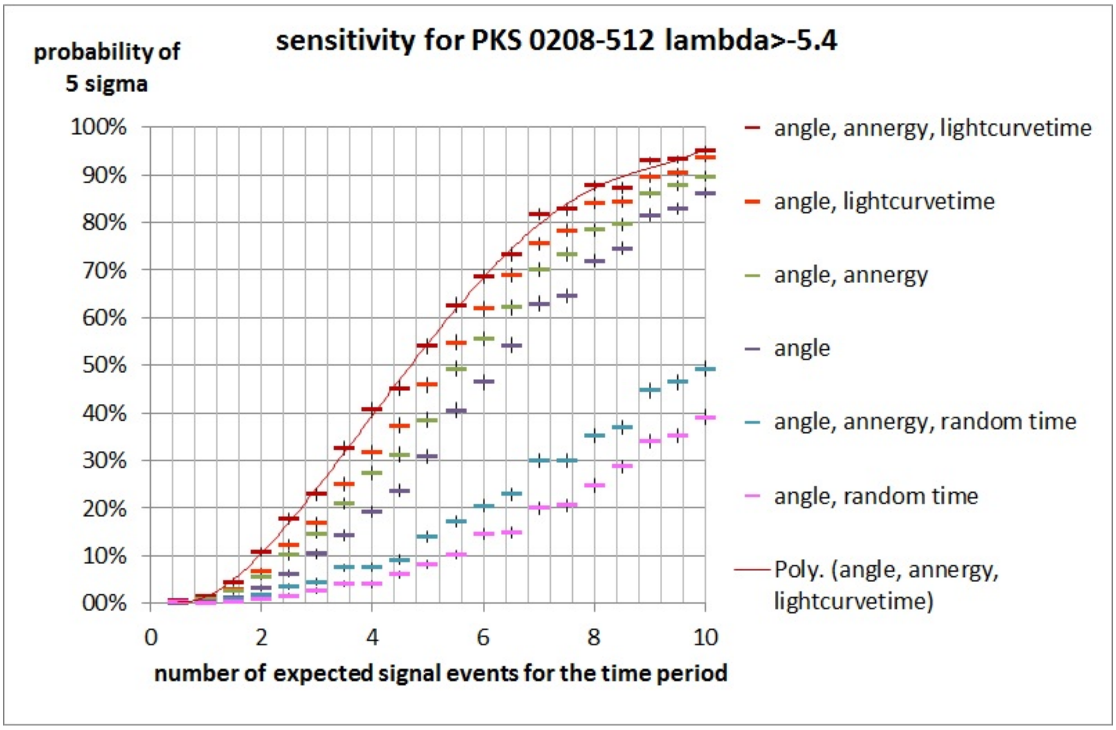

FIGURE A.10: Optimized sensitivity for PKS 0208-512

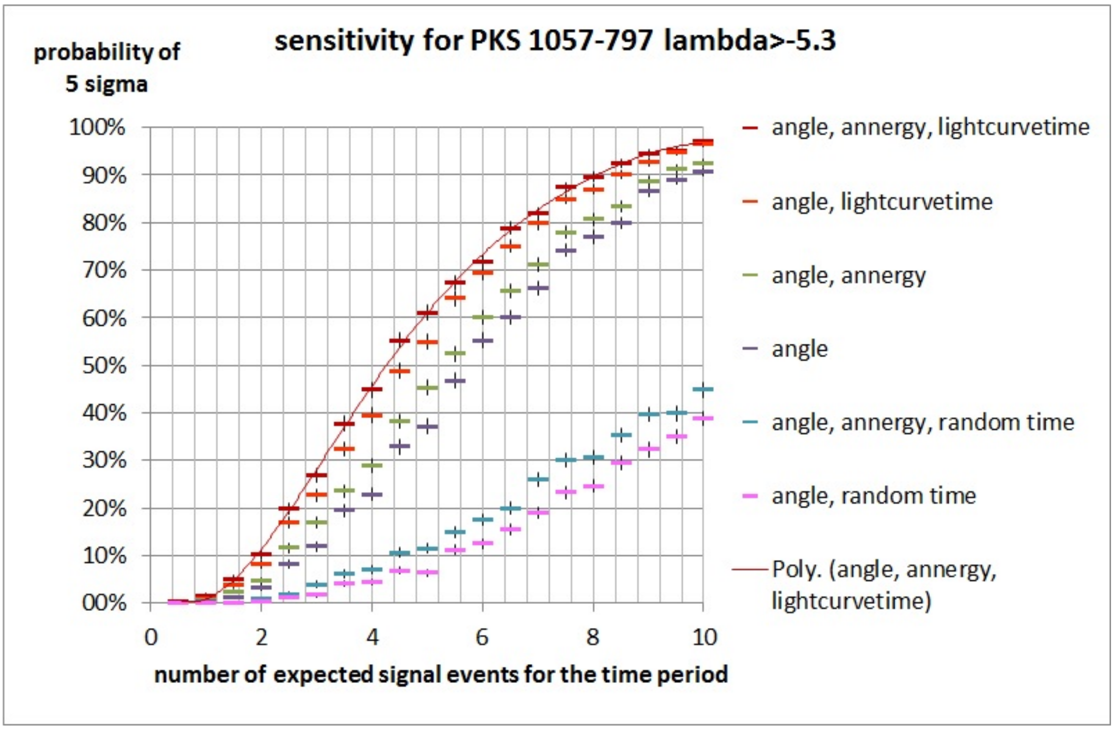

FIGURE A.11: Optimized sensitivity for PKS 1057-797

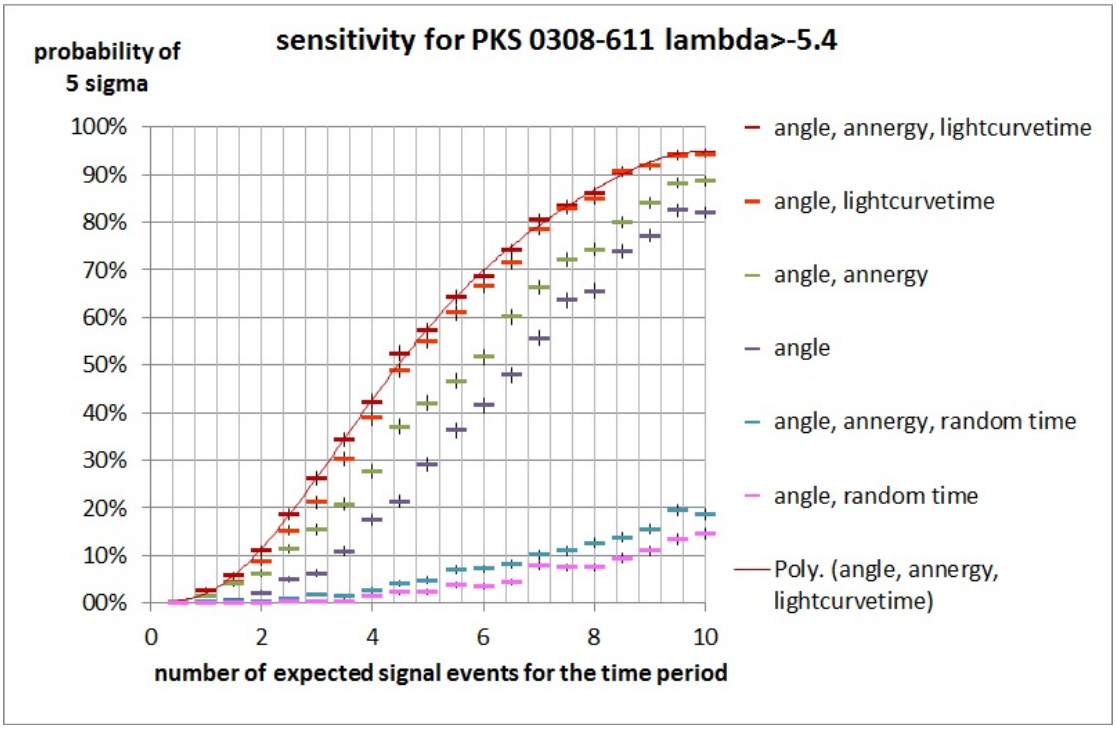

FIGURE A.12: Optimized sensitivity for PKS 0308-611

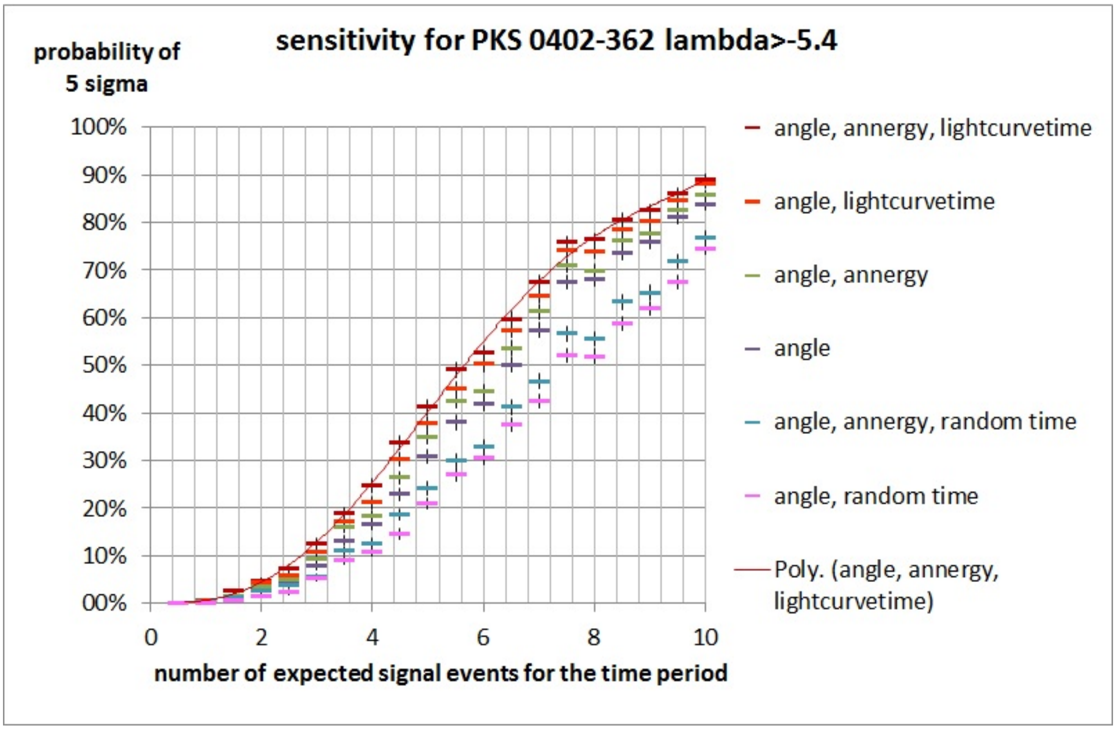

FIGURE A.13: Optimized sensitivity for PKS 0402-362

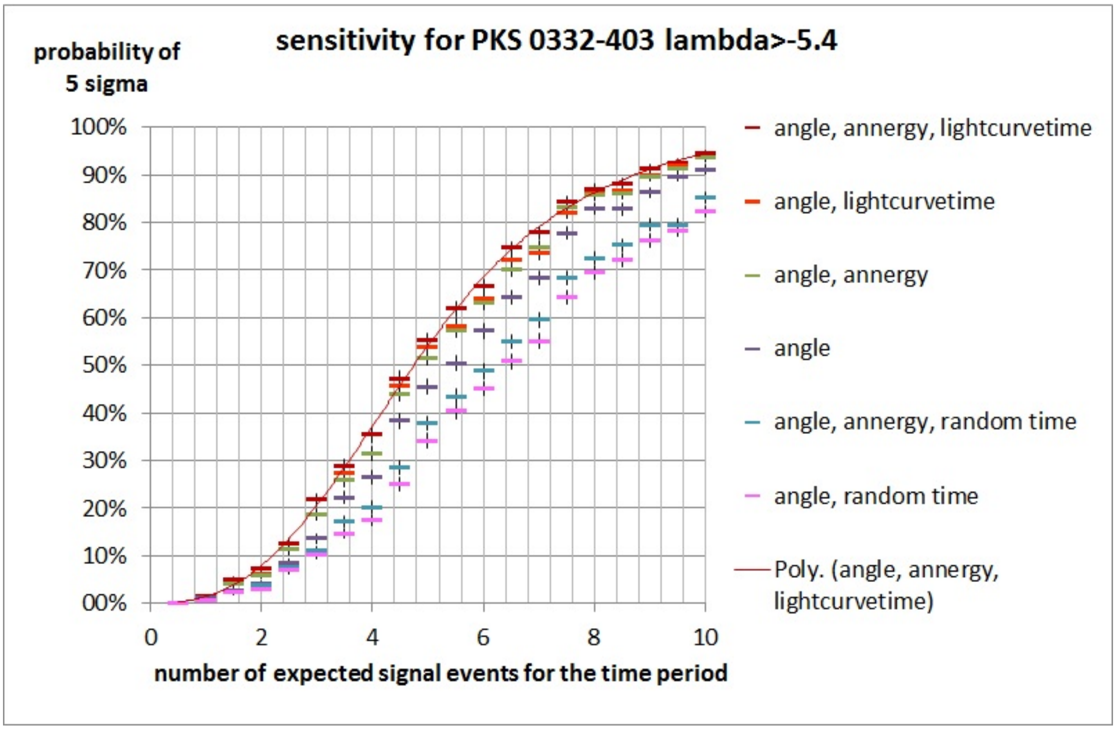

Figure A.14: Optimized sensitivity for PKS 0332-403

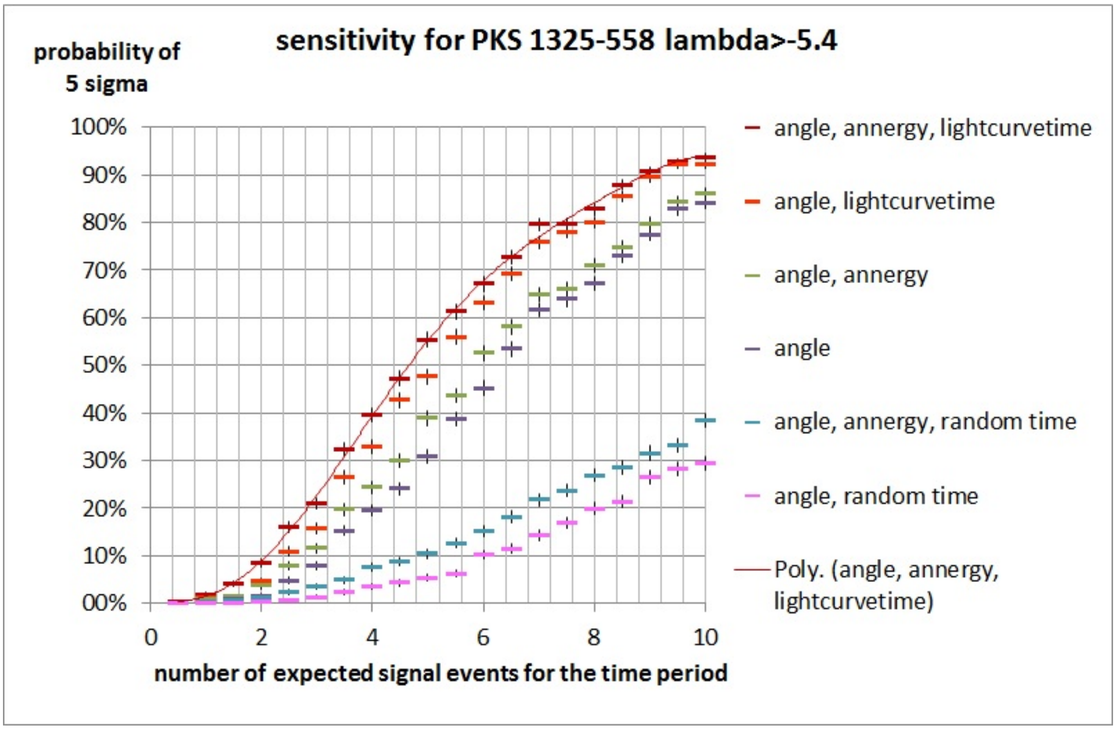

Figure A.15: Optimized sensitivity for PKS 1325-558

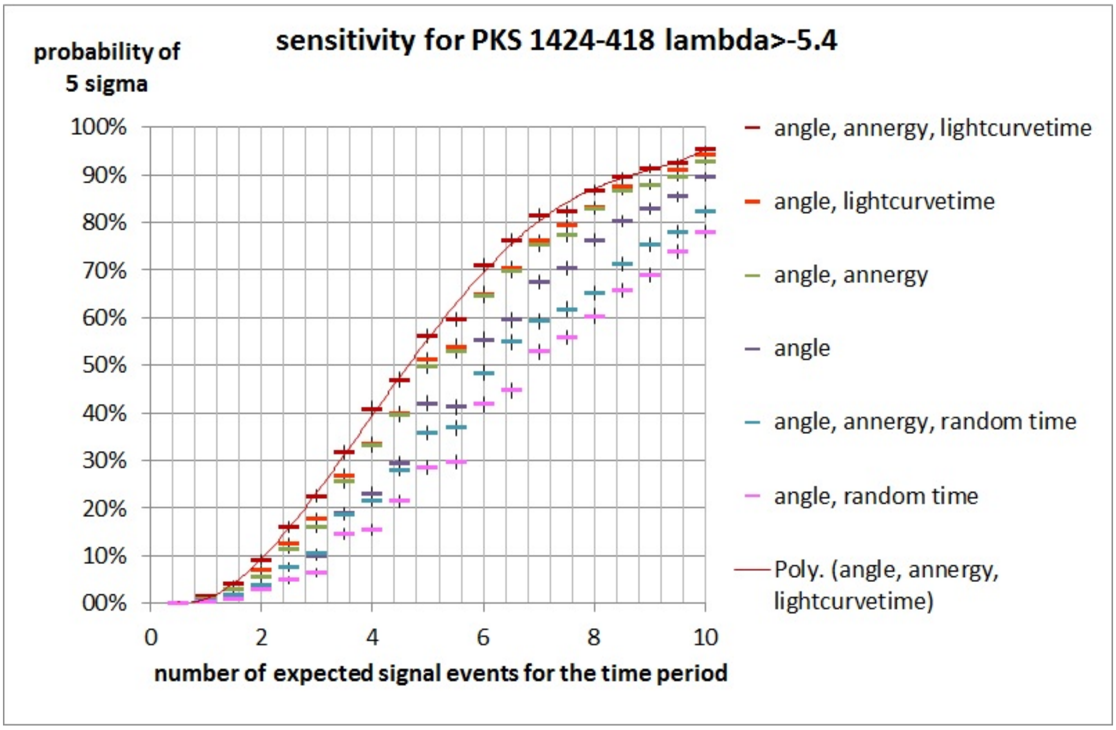

Figure A.16: Optimized sensitivity for PKS 1424-418

Appendix B

Tables of limit calculation

TABLE B.1: Probabilities of the values of the test statistic for all runs for E^{-1} spectrum

D	$\mu = 1$	$\mu = 2$	$\mu = 3$	$\mu = 4$	$\mu = 5$	$\mu = 6$	$\mu = 7$
0.5	71.8%	57.4%	43.1%	32.6%	23.4%	17.3%	12.4%
1	7.4%	7.9%	7.9%	7.4%	6.2%	6.0%	3.9%
1.5	5.0%	6.3%	7.1%	6.6%	6.3%	5.4%	4.2%
2	3.4%	5.5%	5.9%	6.2%	5.9%	4.9%	4.2%
2.5	3.0%	4.2%	5.2%	5.1%	5.3%	4.6%	4.3%
3	2.2%	3.3%	4.5%	4.7%	5.0%	4.4%	4.3%
3.5	1.6%	2.8%	3.7%	4.6%	4.6%	4.2%	4.0%
4	1.2%	2.0%	3.1%	3.6%	4.2%	4.2%	3.9%
4.5	0.8%	1.6%	2.5%	3.2%	3.8%	4.0%	4.0%
5	0.6%	1.3%	2.1%	2.7%	3.4%	3.7%	3.5%
5.5	0.4%	1.1%	1.6%	2.4%	3.0%	3.0%	3.1%
6	0.3%	0.8%	1.7%	2.1%	2.9%	3.1%	3.0%
6.5	0.2%	0.7%	1.3%	1.8%	2.2%	2.8%	3.1%
7	0.2%	0.5%	1.0%	1.8%	2.2%	2.3%	3.1%
7.5	0.2%	0.4%	0.9%	1.7%	1.8%	2.3%	2.9%
8	0.1%	0.4%	0.8%	1.2%	1.9%	2.0%	2.2%
8.5	0.1%	0.2%	0.7%	1.0%	1.3%	1.8%	2.4%
9	0.1%	0.2%	0.6%	0.8%	1.3%	1.6%	2.2%
9.5	0.1%	0.2%	0.5%	0.9%	1.2%	1.6%	2.0%
10	0.3%	0.4%	0.6%	1.0%	1.4%	1.7%	1.7%
10.5	0.2%	0.5%	0.6%	1.0%	1.1%	1.3%	1.7%
11	0.2%	0.3%	0.6%	0.8%	1.1%	1.4%	1.8%
11.5	0.1%	0.2%	0.5%	0.7%	0.9%	1.4%	1.7%
12	0.1%	0.3%	0.5%	0.6%	0.9%	1.3%	1.4%

Table B.2: Feldman and Cousins ranking for all runs for E^{-1} spectrum

D	$\mu = 1$	$\mu = 2$	$\mu = 3$	$\mu = 4$	$\mu = 5$	$\mu = 6$	$\mu = 7$
0.5	1.00	0.80	0.60	0.45	0.33	0.24	0.17
1	0.94	1.00	1.00	0.94	0.79	0.76	0.50
1.5	0.07	0.90	1.00	0.94	0.89	0.77	0.60
2	0.56	0.90	0.96	1.00	0.96	0.79	0.68
2.5	0.04	0.78	0.97	0.96	1.00	0.87	0.80
3	0.43	0.66	0.90	0.93	1.00	0.88	0.86
3.5	0.02	0.61	0.79	0.99	1.00	0.90	0.87
4	0.28	0.47	0.73	0.84	1.00	0.98	0.92
4.5	0.01	0.40	0.63	0.79	0.94	1.00	1.00
5	0.17	0.34	0.58	0.75	0.92	1.00	0.96
5.5	0.01	0.35	0.50	0.76	0.93	0.95	0.98
6	0.09	0.25	0.55	0.69	0.93	1.00	0.97
6.5	0.00	0.21	0.38	0.53	0.66	0.85	0.93
7	0.06	0.15	0.32	0.59	0.71	0.76	1.00
7.5	0.00	0.15	0.31	0.56	0.61	0.76	0.95
8	0.05	0.15	0.32	0.43	0.70	0.76	0.83
8.5	0.00	0.09	0.25	0.40	0.51	0.69	0.92
9	0.05	0.09	0.21	0.31	0.48	0.60	0.81
9.5	0.00	0.09	0.20	0.34	0.44	0.60	0.74
10	0.12	0.18	0.26	0.45	0.59	0.75	0.75
10.5	0.00	0.21	0.27	0.41	0.45	0.56	0.73
11	0.09	0.14	0.26	0.33	0.45	0.56	0.76
11.5	0.00	0.09	0.20	0.26	0.37	0.57	0.66
12	0.04	0.12	0.23	0.27	0.40	0.56	0.62

Appendix C

Calculation of the angular smearing

ϑ and φ are zenith and azimuth of the source, $\tilde{\vartheta}$ and $\tilde{\varphi}$ are zenith and azimuth of the reconstructed direction. The vector of the axis for the rotation is the following.

$$\begin{pmatrix} \sin\vartheta \cdot \cos\varphi \\ \sin\vartheta \cdot \sin\varphi \\ \cos\vartheta \end{pmatrix} \times \begin{pmatrix} 0 \\ 0 \\ 1 \end{pmatrix} = \sin\vartheta \cdot \begin{pmatrix} \sin\varphi \\ -\cos\varphi \\ 0 \end{pmatrix}$$

The rotation of the vector of the reconstructed direction is done as follows.

$$\begin{pmatrix} (\sin\varphi)^2(1-\cos\vartheta)+\cos\vartheta & -\sin\varphi\cos\varphi(1-\cos\vartheta) & -\cos\varphi\sin\vartheta \\ -\cos\varphi\sin\varphi(1-\cos\vartheta) & (\cos\varphi)^2(1-\cos\vartheta)+\cos\vartheta & -\sin\vartheta\sin\varphi \\ \cos\varphi\sin\vartheta & \sin\varphi\sin\vartheta & \cos\vartheta \end{pmatrix} \circ \begin{pmatrix} \sin\tilde{\vartheta} \cdot \cos\tilde{\varphi} \\ \sin\tilde{\vartheta} \cdot \sin\tilde{\varphi} \\ \cos\tilde{\vartheta} \end{pmatrix}$$

This gives the rotated vector $\vec{v} := \begin{pmatrix} x_1 \\ x_2 \\ x_3 \end{pmatrix}$.

The tilted source vector has got zenith ε and an arbitrary azimuth Φ.
So the new angle between the vectors is calculated as follows.

$$\cos\alpha = \begin{pmatrix} \sin\varepsilon \cdot \cos\Phi \\ \sin\varepsilon \cdot \sin\Phi \\ \cos\varepsilon \end{pmatrix} \circ \begin{pmatrix} x_1 \\ x_2 \\ x_3 \end{pmatrix}$$

Appendix D

Lightcurves and events

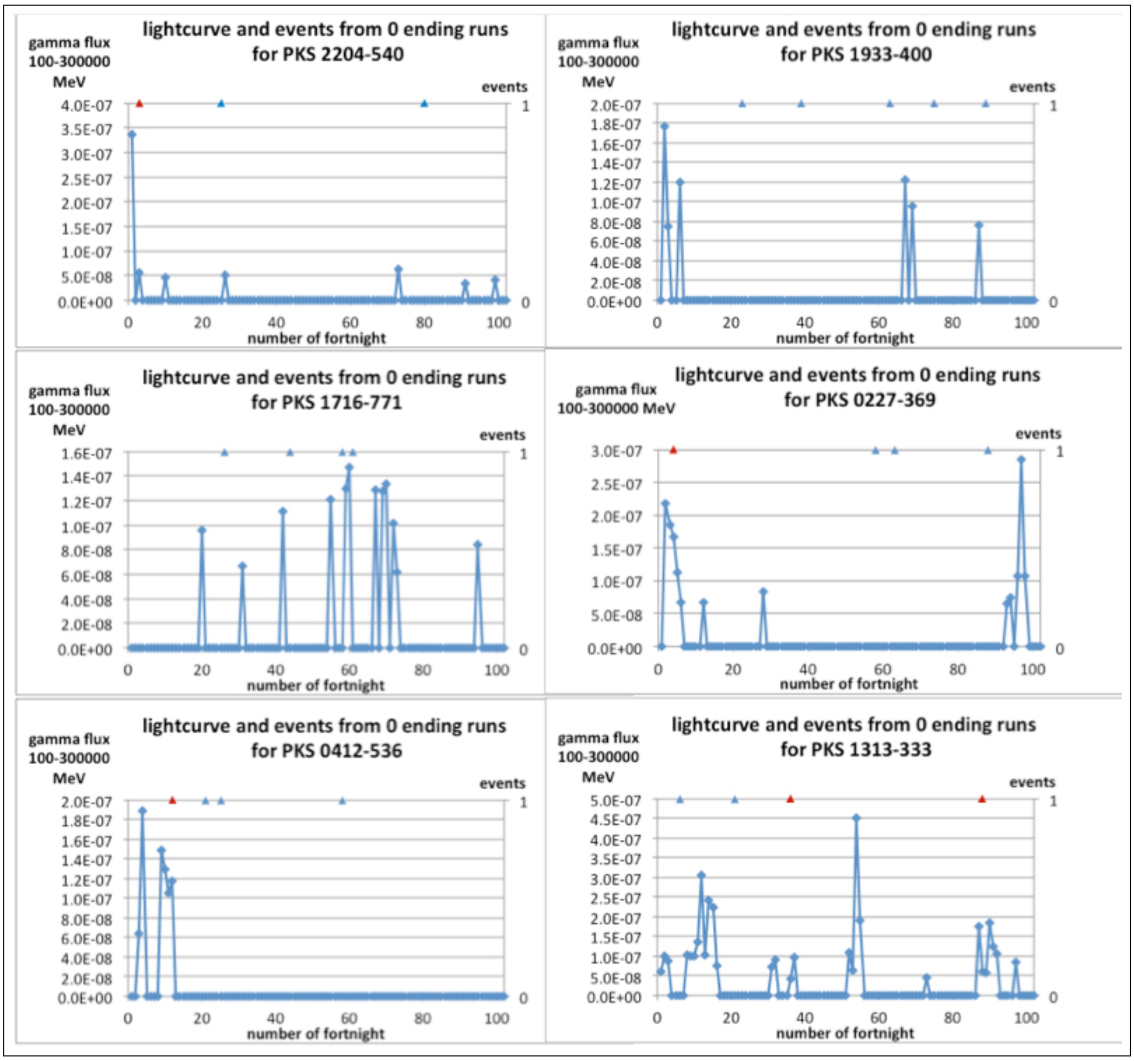

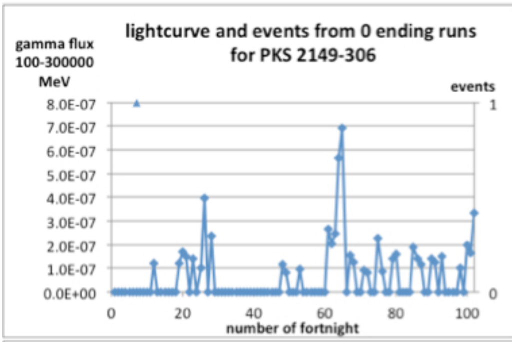
lightcurve and events from 0 ending runs
for PKS 2149-306
gamma flux
100-300000
MeV
events
number of fortnight

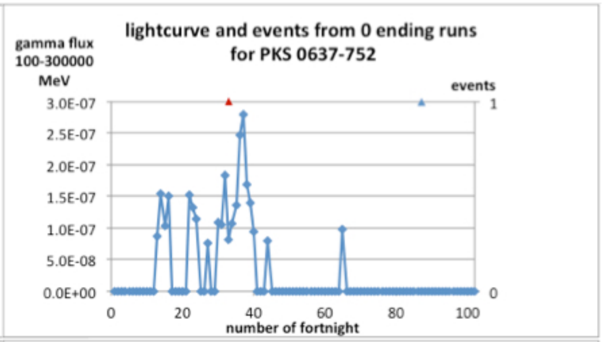
lightcurve and events from 0 ending runs
for PKS 0637-752
gamma flux
100-300000
MeV
events
number of fortnight

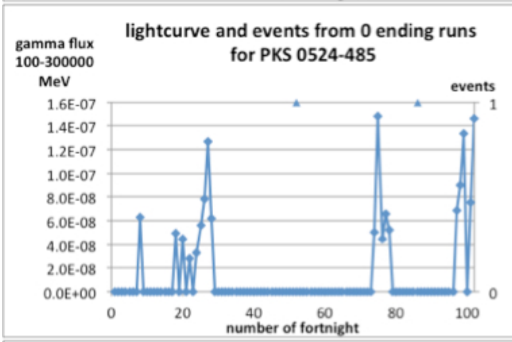
lightcurve and events from 0 ending runs
for PKS 0524-485
gamma flux
100-300000
MeV
events
number of fortnight

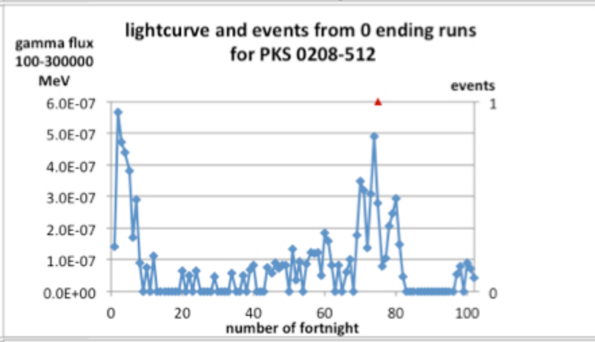
lightcurve and events from 0 ending runs
for PKS 0208-512
gamma flux
100-300000
MeV
events
number of fortnight

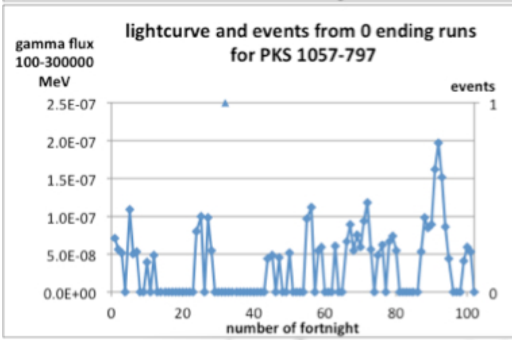
lightcurve and events from 0 ending runs
for PKS 1057-797
gamma flux
100-300000
MeV
events
number of fortnight

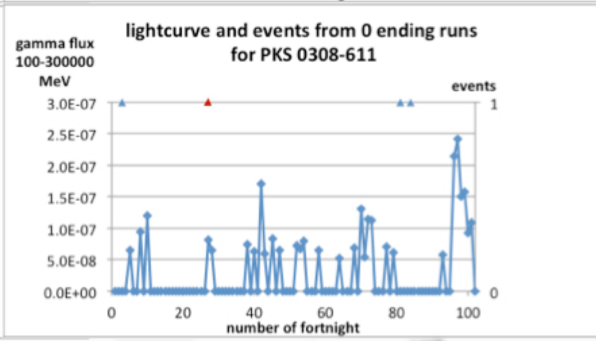
lightcurve and events from 0 ending runs
for PKS 0308-611
gamma flux
100-300000
MeV
events
number of fortnight

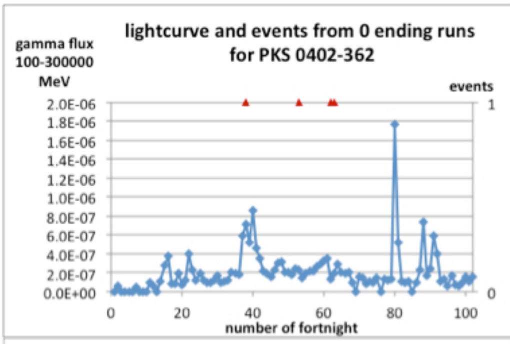
lightcurve and events from 0 ending runs
for PKS 0402-362
gamma flux
100-300000
MeV
events
number of fortnight

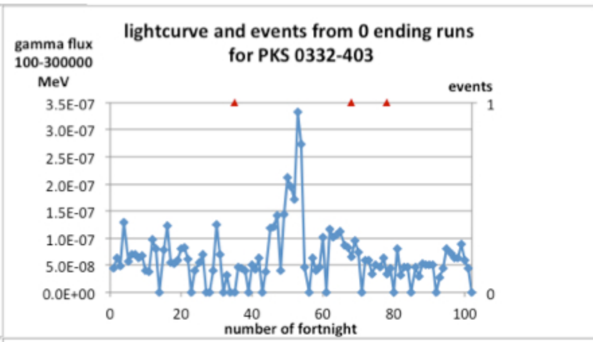
lightcurve and events from 0 ending runs
for PKS 0332-403
gamma flux
100-300000
MeV
events
number of fortnight

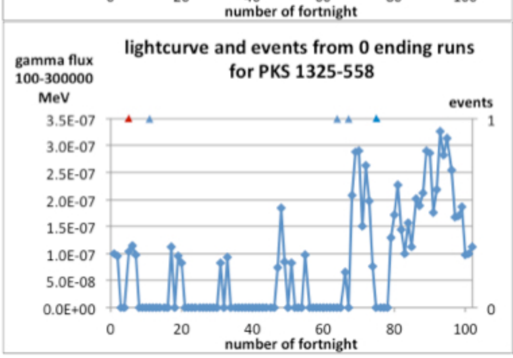
lightcurve and events from 0 ending runs
for PKS 1325-558
gamma flux
100-300000
MeV
events
number of fortnight

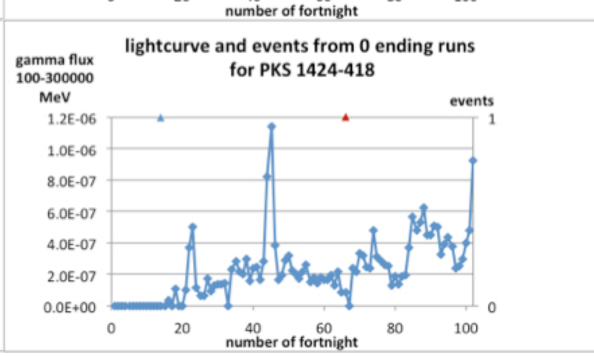
lightcurve and events from 0 ending runs
for PKS 1424-418
gamma flux
100-300000
MeV
events
number of fortnight

Bibliography

[Ab11] R. Abbasi et al., *Time-integrated searches for point-like sources of neutrinos with the 40-string IceCube detector*, Astrophys. J. **732** (2011) 18

[AM04] A. L'Abbate, T. Mntaruli, I. Sokalski, GENHEN *v6: ANTARES neutrino generator extension to all neutrino flavors and inclusion of propagation through the Earth* ANTARES-Soft-2004-010 (2004)

[Ac06] A. Achterberg et al., *On the selection of AGN neutrino source candidates for a sources stacking analysis with neutrino telescopes*, Astropart. Phys. **26** (2006) 282-300

[Ad12] S. Adrián-Martínez et al., *Search for neutrino point sources with four years of data from the ANTARES telescope*, Astrophys. J. **760** (2012) 53

[Ad13] S. Adrián-Martínez et al., *Search for muon neutrinos from gamma-ray bursts with the ANTARES neutrino telescope using 2008 to 2011 data*, Astron. Astrophys. **559** (2013)

[Ad14] S. Adrián-Martínez et al., *Searches for Point-like and Extended Neutrino Sources close to the Galactic Center using the ANTARES Neutrino Telescope*, Astrophys. J. **786** (2014)

[Ag11] M. Ageron et al., *ANTARES*, Nucl. Instrum. Meth. A **656** (2011) 11-38

[An97] P. Antoniolo, C. Ghetti, E. V. Korolkova, V. A. Kudryavtsev, G. Sartorelli, MUSIC *A Three-Dimensional Code for Muon Propagation through the Rock* [arXiv:hep-ph/9705408] (1997)

[Ba02] D. Bailey, *Dark Matter, the deep ocean and neutrinos from heaven: Monte Carlo tools and analysis methods for understanding the ANTARES experiment and predicting its sensitivity to Dark Matter*, PhD thesis Oxford 2002

[Be08] J. Becker, *High-energy neutrinos in the context of multimessenger astrophysics*, Phys. Rep.**458**.4-5 (2008) 173-246

[BS12] V. Beckmann, C. Shrader, *Active Galactic Nuclei*, Wiley-Vch, 2012

[BZ77] R. Blandford, R. Znajek, *Electromagnetic extraction of energy from Kerr black holes*, MNRAS **179** (1977) 433

[Bo14] G. De Bonis, GENHEN *release v7r1*, ANTARES-SOFT-2014-001 (2014)

[Br10] J. Braun et al., *Time-Dependent Point Source Search Methods in High Energy Neutrino Astronomy*, Astropart. Phys. **33** (2010) 175-181

[Bru99] J. Brunner, *Updated tag list for the new ANTARES event format*, ANTARES-SOFT-1999-003 (1999)

[Co13] L. Core, *Search of an ultra high energy neutrino diffuse flux with the ANTARES telescope*, PhD thesis Marseille 2013

[EK09] T. Eberl, C. Kopper, *The SeaTray software framework*, ANTARES-SOFT-2009-013 (2009)

[FC98] G. Feldman, R. Cousins, *Unified approach to classical statistical analysis of small signals*, Phys. Rev. D **57** (1998)

[Fe49] E. Fermi, *On the Origin of the Cosmic Radiation*, Phys. Rev. *75* (1949)

[FZ11] V. Frolov, A. Zelnikov, *Introduction to black hole physics*, Oxford University Press, 2011

[He04] A. Heijboer, *Track reconstruction and point source searches with ANTARES*, PhD thesis Amsterdam 2004

[In96] G. Ingelmann, A. Edin, J. Rathsman, LEPTO 6.5 - *A Monte Carlo Generator for Deep Inelastic Lepton-Nucleon Scattering* [arXiv:hep-ph/9605286] (1996)

[Jo10] M. de Jong, *The Trigger Efficiency program*, ANTARES-SOFT-2009-001 (2010)

[KS12] U. F. Katz, C. Spiering, *High-Energy Neutrino Astrophysics: Status and Perspectives*, Prog. Part. Nucl. Phys. *67* (2012)

[Ke08] R. P. Kerr, *Discovering the Kerr- and Kerr-Schild metrics*, [arXiv:0706.1109] (2008)

[Kr12] F. Kraußet al., *Multiwavelength observations of TANAMI sources*, Conference Proceedings of "11th European VLBI Network Symposium and Users Meeting", published in Proceedings of Science (2012)

[Li91] P. Lipari, T. Stanev, *Phys. Rev.* **D44** (1991) 3543

[Ma00] K. Mannheim, R. J. Protheroe, J. P. Rachen, *Cosmic ray bound for models of extragalactic neutrino production*, Phys. Rev. D *63* 023003 (2000)

[MM03] J. Martí, E. Müller, *Numerical Hydrodynamics in Special Relativity*, Living Rev. Relat. *6* (2003)

[Me12] A. Meli, L. Biermann, L.: Active Galactic Nuclei Jets and Multiple Oblique Shock Acceleration: Starved Spectra arXiv:1207.4397v1 (2012)

[MP14] A. Mücke, R. J. Protheroe, R. Engel, J. P. Rachen, T. Stanev, *BL lac objects in the synchrotron proton blazar model*, Astropart. Phys. **18**.6 (2003) 593-613

[Mu14] C. Müller, *High-Resolution Observations of Active Galactic Nuclei in the Southern Hemisphere*, PhD thesis Erlangen 2014

[NT99] S. Navas, L. Thompson, KM3 *user guide and reference manual*, ANTARES-Soft-1999-011, 2011

[No12] P. L. Nolan et al, *Fermi large area telescope second source catalog*, ApJS **199**.31 (2012)

[Pe69] R. Penrose, *Extraction of rotational energy from a black hole*, Rev. Nuovo. Cim. **1** (1969) 252

[PR99] B. Povh, K. Rith, C. Scholz, F. Zetsche, *Teilchen und Kerne*, Springer 1999

[Re12] A. Reimer, *On the Physics of Hadronic Blazar Emission Models*, JPCS *355* (2012)

[Ri11] F. Rieger, *Cosmic ray acceleration in active galactic nuclei*, Frontiers Science Series **57** (2011) 43-49

[Scn10] J. Schnabel, *Muon Energy Reconstruction for the Neutrino Telescope ANTARES using Neuronal Networks*, Diploma thesis Erlangen 2010

[Scu11] O. Schulz, *The design study of IceCube deep core*, PhD thesis Heidelberg 2011

[Sj95] T. Sjostrand, PYTHIA 5.7 and JETSET 7.4 *Physics and Manual* [arXiv:hep-ph/9508391] (1995)

[St10] T. Stanev, *High energy cosmic rays*, Springer 2010

[Tc11] A. Tchekhovskoy, R. Narayan, J. C. McKinney, *Efficient generation of jets from magnetically arrested accretion on a rapidly spinning black hole*, MNRAS **418**.79-83 (2011)

[Ti11] J. Tiffenberg, *UHE neutrino searches with the Pierre Auger neutrino observatory*, NUSKY (2011)

[Tr08] R. Treumann, C. Jaroschek, *Fundamentals of Non-relativistic Collisionless Shock Physics: V. Acceleration of Charged Particles*, [arXiv:0806.4046] (2008)

[Vo12] H. Voigt, *Abriss der Astronomie*, Wiley-Vch 2012

[WA14] http://antares.in2p3.fr/internal/dokuwiki

[WM14] A. Müller, *Lexikon der Astrophysik*, https://www.wissenschaft-online.de/astrowissen/lexdt.html

[WS14] SLALIB - *Positional Astronomy Library* http://star-www.rl.ac.uk/docs/sun67.htx/sun67.html

Acknowledgements

Meiner Doktormutter Prof. Dr. Gisela Anton bin ich sehr dankbar, dass sie mir in ihrer klaren Art mit ihrem Einsatz für mich ermöglicht hat, einen Lebenstraum zu erfüllen.

Prof. Dr. Ulrich Katz hat sich Zeit genommen für Gespräche und Ermutigungs-Emails und hat in großer Kenntnis des Detektors wichtige Sachhinweise gegeben.

I would like to thank PhD Clancy James for the advice in our regular meetings.

Prof. Dr. Elisa Resconi danke ich für die einführende Hilfestellung. PD Dr. Alexander Kappes danke ich für den Hinweis auf ein hilfreiches Paper und für die Diskussion bezüglich des Korrekturfaktors. Dr. Thomas Eberl ist mit mir eine ganze Zugfahrt lang die Berechnung der Akzeptanz durchgegangen, vielen Dank! Dr. Kay Graf war stets freundlicher und verlässlicher Ansprechpartner besonders bei Fragen zur Schicht. Das Lernen bei den Schichten mit Rezo Shanidze, Björn Herold, Jutta Schnabel, Maria Tselengidou hat mir große Freude gemacht. Jutta Schnabel danke ich ganz besonders, dass sie mit mir alle vor der Analyse liegenden Schritte der Simulationskette durchgearbeitet hat.
Thanks to the members of the ANTARES and TANAMI collaboration, who almost always answered immedeately.
Ich sage Dank an alle im ECAP, die mir geholfen haben und ein lebenswertes Arbeitsumfeld geschaffen haben, so auch Florian Folger und vor allem meine Zimmerkollegen Stefan Geißelsöder und Jannik Hofestädt.
Meinem guten Freund Holger danke ich für seine Unterstützung.
Meinen Eltern hier zu danken, würde weit den Rahmen sprengen.